EXPERIMENTAL STUDY OF HIGH BETA TOROIDAL PLASMAS

by

ARNOLD GARY KELLMAN

A thesis submitted in partial fulfillment of the
requirements for the degree of

DOCTOR OF PHILOSOPHY

(Physics)

at the

UNIVERSITY OF WISCONSIN-MADISON

1983

EXPERIMENTAL STUDY OF HIGH BETA TOROIDAL PLASMAS

Arnold Gary Kellman

Under the supervision of Associate Professor Stewart C. Prager

Experiments on the Wisconsin Levitated Toroidal Octupole have produced a wide range of stable high β plasmas with β significantly above single fluid MHD theory predictions. A stable $\beta \sim 8\%$ plasma, twice the fluid limit, is obtained with $5\rho_i \sim L_n$ and $\tau_\beta \approx 6000\ \tau_{\text{Alfvén}} = 600\ \mu\text{sec}$. The enhanced stability is explained with a kinetic treatment that includes the effect of finite ion gyroradius which couples the ballooning mode to an ion drift wave. Measurement of the perturbation to the vacuum magnetic field due to the plasma diamagnetism agrees well with single fluid theory predictions. In a more collisional, large gyroradius ($2\rho_i \sim L_n$) regime, a stable $\beta \sim 35\%$ plasma is obtained with a decay time of 1000 Alfvén times. Measurement of the equilibrium magnetic field in this regime indicates that the diamagnetic current density is five times smaller than predicted by ideal MHD, probably due to ion gyroviscosity. Since the ballooning mode is predominantly diamagnetic current driven, this may account for the observed stability.

Particle transport is anomalous and ranges from agreement with the classical diffusion rate at the highest beta, lowest field plasma ($B_p = 200$ G), to thirteen times the classical rate in a $\beta = 11\%$, high field plasma ($B_p = 860$ G) where the level of enhancement increases with magnetic field. There is no evidence that this anomalous rate of diffusion is beta related. Experimental density profiles are compared to numerical solutions of the time dependent diffusion equation, and it is found that in many cases, the profiles can be matched if the diffusion is classical in the absolute good curvature region and classical enhanced by vortex diffusion in the average good curvature region. No mechanism has been identified that accounts for different diffusion mechanisms in the two curvature regions.

Fluctuations in density, electrostatic potential, and magnetic field have been studied in plasmas with β from 0.1% to 40%. In all plasmas, fluctuation levels peak in the bad curvature region, however, no β related fluctuations have been identified ($\tilde{B}/B<0.1\%$, $\tilde{n}/n<5\%$).

ACKNOWLEDGEMENTS

I would like to thank my adviser, Professor Stewart Prager, for his encouragement and guidance throughout this research. His attitude toward research and enthusiam for this project helped make my graduate career both personally and academically rewarding.

I would also like to thank Dr. Richard S. Post for helping me in the early stages of this research and for challenging me to explore new ideas. My appreciation is also due to Professor J.C. Sprott for reminding me when I worked with him that research should be fun.

This work could not have been completely as sucessfully without the help of my fellow graduate students. In particular, I am indebted to Dr. Ted Strait and Mike Zarnstorff for their help in all aspects of this experiment. To my officemate, Tom Osborne, and all the graduate students, I offer my sincerest gratitude for sharing their knowledge and experience, giving me encouragement when times were hard, and generally making my stay at Wisconsin a continually enjoyable experience.

I would also like to thank John Laufenberg and his able crew of hourlies for their expert and willing assistance without which no experiment on the Octupole would be possible. The experience of Tom Lovell in the design stage of this experiment is also greatly appreciated.

I thank Kay Shatrawka for her help with the typing and preparation of this thesis.

TABLE OF CONTENTS

Page

CHAPTER 1

Introduction

1.A. Motivation and Background

A fundamental parameter in plasma physics is β, defined as the ratio of plasma pressure to magnetic pressure. As β is increased, the plasma pressure increases relative to the confining magnetic fields and one can no longer neglect the effect of the plasma on the externally applied fields. Ideal magnetohydrodynamic theory (MHD) predicts that above a critical value of β, the internal plasma currents and resultant self-fields perturb the external field enough that the plasma becomes unstable and confinement may degrade. This region of instability has never been observed because previous experiments have achieved only low β plasmas or high β plasmas that are too short-lived to permit the growth of the instability. The attainment of long-lived high β plasmas and subsequent search for this instability is essential since the theory is fundamental to the understanding of plasma behavior. In addition, the study of high β effects on plasma equilibrium and transport properties will permit the verification of other critical elements of plasma theory not yet explored experimentally. There is also a practical concern, since future magnetic confinement fusion reactors will require high β plasma in order to be economically feasible. The power output density of current reactor schemes can be shown to be proportional to the square of the plasma β[1], and thus smaller and more efficient reactors are possible if high β plasma is obtained. Thus, there is a strong motivation to study the behavior of plasmas at high β and to search for this instability.

In most plasma devices there are two types of magnetic field curvature, good and bad curvature, depending on the relative direction of the plasma pressure gradient and the magnetic field gradient. In a good curvature region, the pressure gradient and the magnetic field gradient are in opposite directions, while the opposite is true in a bad curvature region. In many magnetic configurations, the same field line may have both types of curvature. If the "average" curvature along a field line is good, the plasma is located in an effective magnetic well, i.e. on the average, the confining field is stronger outside of the plasma. A device with field lines that possess average good curvature is referred to as a minimum-average-B configuration. If there are regions in which the field lines have only one type of curvature, these are referred to as "absolute" good or bad curvature regions.

Certain classes of plasma perturbations, for example, the MHD interchange mode, are unstable in a bad curvature region. At low values of β, the most unstable MHD modes cause rigid displacements of field lines and thus do not expend energy bending field lines. Thus, the amplitude is constant along a field line ($\lambda_{\parallel}=\infty$), and the mode equally weights regions of good and bad curvatures. If the average curvature is good, the mode is stabilized.

If the amplitude was not constant along a field line, then the mode could go unstable in the bad curvature region only. This localization bends the field lines which requires energy, and at low β, this energy is not available; however, as beta is increased, a value is reached where the stabilization due to field line bending is smaller than the destabilizing effect of mode localization in the bad curvature regions. All minimum-average-B configurations have a critical beta above which this ideal MHD "ballooning" instability is predicted to onset. Many tokamaks have reported volume average beta, $\langle\beta\rangle$, near that predicted by MHD for the onset of the ballooning mode. None of these have reported exceeding this β limit or the observation of an ideal ballooning mode.

In circular cross section tokamaks, the $\langle\beta\rangle$ limit is 2.5-3.0%[2]. ISX-B has obtained $\langle\beta\rangle \sim 2.5-3.0\%$ with an injected beam power of 1.7MW. It was reported[3] earlier that this was above the ideal ballooning limit, however, a more detailed analysis of the equilibrium[4] has increased the theoretical beta limit so that the observed β is too close to the stability limit to determine if it has been exceeded. As yet, there has been no observation of a sudden degradation of confinement above a certain value of β which would be the mark of an ideal ballooning mode. However, β has not continued to increase as rapidly as expected as beam power is increased. This gradual deterioration of confinement as β increases has been referred to as a "soft β-limit". Recent studies have indicated that this is not related to the increases in the toroidal beta (computed using the value of the toroidal field) which is the relevant parameter for the ideal ballooning mode. They attribute the poor confinement either to the effects of plasma rotation or to a resistive ballooning mode. Although the latter is related to the ideal ballooning mode, it is not the same thing and in particular, does not have a β threshold; rather it is unstable at all values of β with a linear growth rate that depends on β. This mode will be discussed in the context of the current experiment in Chapter 5.

In a non-circular cross section plasma the β limit is higher, and thus Doublet III has achieved a volume average beta of 4.5% in an elongated plasma[5]. In the Doublet experiment they see no evidence of an ideal ballooning mode, however, as with ISX-B, there is degradation of confinement. As in the other tokamak experiments, the high values of beta are achieved by injection of high power (up to 5MW) neutral hydrogen beams. They report that the enhancement of $\langle\beta\rangle$ with plasma shaping is in qualitative agreement with theory and that the plasma beta is still increasing with input beam power. Additional tokamak experiments done on JFT-2[6] in Japan and PDX[7] at Princeton have also obtained volume average beta near the ideal ballooning limit with no observation of the mode.

On multipole devices, high beta experiments have been performed on the UCLA Dodecapole[8] and the University of Wisconsin Levitated Toroidal Octupole[9]. On the Dodecapole, stable plasmas with a β of

8% have been obtained in a region where the beta limit was 7%. These were large gyroradius plasmas (on the order of the density gradient scale length), and the equilibrium was stable with a decay time in excess of 400 Alfven times, which is the time scale for ideal MHD activity. Stable plasma have been observed in the Octupole with β significantly above the critical beta predicted by ideal MHD theory. An examination of these plasmas is the subject of this study.

A multipole has certain unique features that make it an excellent vehicle for testing the rudimentary ballooning mode theory common to all miminum-average-B devices. Unlike tokamaks, which require a plasma current to create the poloidal magnetic field, in a multipole the magnetic field and externally created plasma are independently adjustable, and thus a much broader range of parameters is accessible. Since multipoles can operate without magnetic shear and without electric field-driven ohmic currents (to eliminate current-driven instabilities), the analysis is simplified and in fact, much of the original theoretical work on ideal ballooning modes[10,11] was done for axisymmetric toroidal devices without magnetic shear, such as a multipole, because it is such a simple device. On the Wisconsin Octupole, shear (through the addition of toroidal field) and ohmic currents are optional and independently controllable features.

1.B. Content and Organization of the Thesis

This thesis will describe work done on the Wisconsin Levitated Octupole in an experimental study of high beta plasmas. The primary objective to this research is to search for the beta limit for the ideal ballooning mode on the Octupole and study the properties of the instability if it is observed. It is also desired to study the equilibrium properties, particle transport, and microstability of these high beta plasmas.

To achieve this we have improved our previous plasma sources (Marshall guns) and built additional sources capable of producing significantly higher densities and plasma beta. Thus we have obtained a wide range of stable high beta plasmas from β=8% to 44% (2 to 10 times the ideal MHD ballooning limit of β=4.3%) in which various mechanisms enable the plasma to exceed the MHD limit. It is shown that the stability at β=8% can be attributed to the finite ion gyroradius effect in which the ballooning mode is manifested as an oscillatory ion drift wave. At β~44%, far in excess of the ideal MHD β limit, the plasma remains macroscopically stable. The finite ion gyroradius effect mentioned above, although a strong stabilizing effect, is not sufficient to explain the enhanced stability of this plasma. The equilibrium properties of this plasma are revealed, by detailed measurements of the diamagnetic currents, to be also poorly described by MHD. It is believed that ion gyroviscosity leads to an observed reduction in the diamagnetic current. In that the diamagnetic current drives the ballooning mode, this reduction stabilizes the plasma. Thus, this work demonstrates the general limitation or fragility of the MHD approximation in describing plasma behavior. In addition, these experimental results and stabilization mechanisms are important in suggesting related methods by which the MHD ballooning limit may be circumvented in other devices.

Particle transport was studied in a range of plasmas from β=1% to 34%. Transport ranges from agreement with the classical diffusion rate at the highest beta (β=34%), lowest field plasma to thirteen times the classical rate in a β=11%, high field plasma. There is no evidence that this anomalous rate of diffusion is beta related. The diffusion does not scale classically either with density or magnetic field, and the enhancement above the classical diffusion rate increases with increasing magnetic field. No single diffusion coefficient can describe all the plasmas studied, and there is evidence that different mechanisms, classical and vortex, are active in the different curvature regions of the plasma.

In Chapter 2, the Octupole and the diagnostics used in this experiment are described. The plasma sources and results of experiments performed with the guns on a test stand are presented.

Chapter 3 discusses the theory of an ideal ballooning mode. A physical picture of the mode in general geometry is presented. Based on this physical picture a discussion of various factors that can affect the stability of the ballooning mode is included. To aid in the interpretation of the experimental results, certain properties of the high β equilibrium are discussed, in particular, the perturbation to the vacuum magnetic field due to the plasma diamagnetism. A detailed theory of the ballooning mode, developed elsewhere[12], is outlined here using the MHD and kinetic stability theory which is employed to interpret these experiments. The MHD theory examines ballooning stability for infinite toroidal mode number (n) and for finite, but high toroidal mode number by means of a perturbation expansion about the $n=\infty$ solution. The kinetic theory is derived for low frequency modes with $\omega \ll \omega_{ci}$ where ω_{ci} is the ion cyclotron frequency. This includes the effects of finite ion gyroradius and trapped and untrapped particles. All equations are solved numerically for the configuration of the experimental device.

Chapter 4 will present the experimental results. This includes optimization of the plasma sources to produce high beta and a detailed description of two of the high beta plasmas, $\beta=8\%$ and 35%. Equilibrium properties measured include density and temperature profiles, decay rates, and plasma diamagnetic perturbation to the vacuum magnetic field. Relevant parameters of additional plasmas representative of the wide range of plasmas obtained will be presented as well as a brief discussion of additional methods that were attempted to obtain high beta plasma.

Chapter 5 compares the experiment with theory, with the consideration of the applicability of the theory to these plasmas and the additional effects that are necessary to account for the enhanced stability. A comparison of the measured equilibrium with

MHD and non-MHD models, including viscosity effects and its relevance to other devices is presented.

Chapter 6 examines the particle transport and fluctuations in these plasmas. Previous work on transport in low beta ($\beta < 1\%$) and low density ($n < 1 \times 10^{13}$ cm^{-3}) plasmas is reviewed. Experimental density profiles are presented for β up to 35% and density in the range of 4×10^{12} to 6×10^{13} cm^{-3}. These are compared with predictions from a computer program which solves the diffusion equation in magnetic flux coordinates in octupole geometry. General properties of fluctuations observed in these high beta plasmas are discussed and more detailed measurements of the fluctuation spectrum of a high beta plasma for density, electrostatic potential, and the toroidal and poloidal components of the magnetic field are presented. Correlation of the fluctuations in density and magnetic field, and density and potential are examined. Finally, a measurement of fluctuation induced particle flux is compared with both the classical particle flux and the actual particle flux determined from the experimental density profiles.

References for Chapter 1

1. W.M. Stacey, Jr., Fusion Plasma Analysis, (J. Wiley and Sons, Inc., N.Y. 1981) Ch. 1.

2. A.M.M. Todd, J. Manickam, M. Ikabayaski, M.S. Chance, R.C. Grimm, J.M. Green, and J.L. Johnson, Nucl. Fusion 19, 743 (1979).

3. M. Murakami et al., Plasma Physics and Controlled Nuclear Fusion Research 1980, Vol. I, (IAEA, Vienna, 1981), 377.

4. M. Murakami, et al., Plasma Physics and Controlled Nuclear Fusion Research 1982, Vol. I, (IAEA, Vienna, 1983).

5. K.H. Burrell, R.D. Stambaugh, et al., Nucl. Fusion 23, 536 (1983).

6. JFT-2 Group, in Proceedings of the Tenth European Conference on Controlled Fusion and Plasma Physics, Moscow, 2, (1981).

7. D. Johnson et al., Plasma Physics and Controlled Nuclear Fusion Research, Baltimore, 1982 (IAEA, Vienna, 1983).

8. R.W. Schumacher, M. Fukao, A.Y. Wong, R.G. Suchannek, K.L. Lane, and K. Yatsu, Phys. Rev. Lett. 46, 1391 (1981).

9. A.G. Kellman, M.W. Phillips, S.C. Prager, and M.C. Zarnstorff, submitted to Nucl. Fusion; J.H. Halle, A.G. Kellman, R.S. Post, S.C. Prager, E.J. Strait, and M.C. Zarnstorff, Phys. Rev. Lett. 46, 1396 (1981).

10. I.B. Bernstein, E.A. Frieman, M.D. Kruskal, R.N. Kulsrud, Proc. Roy. Soc. A 244, 17 (1958).

11. J.M Greene and J.J. Johnson, Plasma Physics 10, 729 (1968).

12. M.W. Phillips, University of Wisconsin Ph.D. Thesis, DOE/ET/53051-29 (1982).

CHAPTER 2

Experimental Apparatus and Methods

This chapter will include a machine description, a brief survey of the diagnostics used in this experiment with additional detail on the diagnostics and techniques unique to this experiment and a description of the operation the Marshall gun plasma sources that were developed to attain high-β plasmas.

2.A. Machine Description

The Wisconsin Levitated Octupole (Fig. 1) is a 1.4 meter major radius toroidal plasma confinement device with a vacuum volume of 8.6 m^3 of which 7.7 m^3 is in the MHD stable region (absolute or average good curvature region).

The vacuum vessel is made of 2" thick high conductivity 1100 aluminum. There are four internal current carrying rings, also made of 1100 aluminum, each with a minor radius of 8.89 cm.

The current in the internal rings is inductively driven. There are 90 primary turns wound on an iron core, and each internal ring is a one turn secondary. An insulated gap (~1/8" thick) in the machine wall in a poloidal cross section prevents the machine wall from being the secondary and thus allows current to flow in the rings. In order for the machine to contain the magnetic field and thus shape the field lines to the desired configuration, the machine

FIG. 1. Schematic view of Wisconsin Levitated Octupole.

WISCONSIN LEVITATED OCTUPOLE

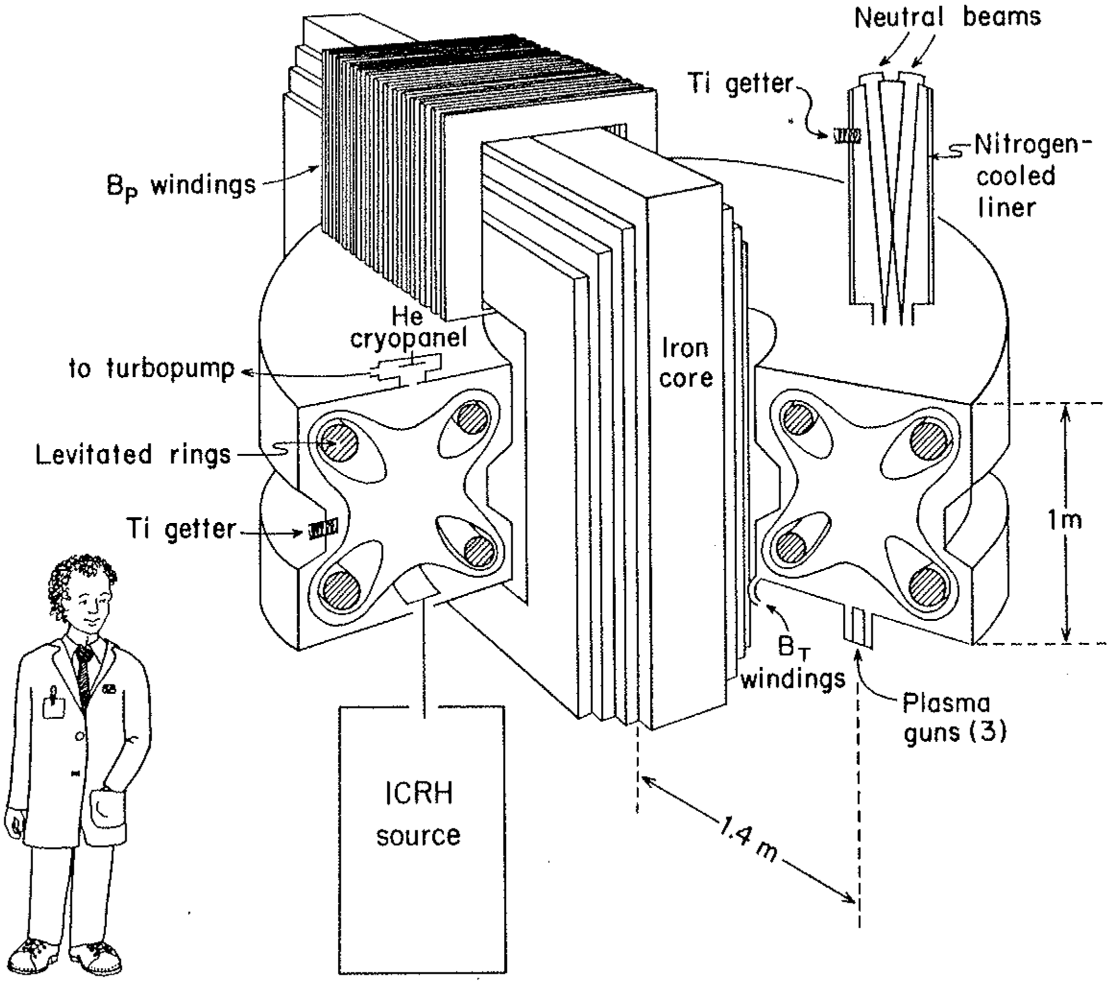

walls must carry the image current of the ring current. As the image current resistively decays in the walls the field lines soak out of the machine. If the vacuum vessel had only an insulated gap as described above, the image currents would flow counter to the hoop current on the inside of the machine and then flow on the outside of the machine in the reverse direction to complete the current path (Fig. 2a). This is undesirable for a number of reasons. First, it can be seen that the machine wall carries no net toroidal current. Thus the magnetic flux is not actually contained in the machine, and will fill up the space outside the machine with valuable flux. This reduces the magnetic field strength in the machine and affects the external diagnostics, as well as affecting the field period since the inductance is increased from the case where all the flux is contained in the machine. A second and more important effect is what happens at the poloidal gap. The image current distribution on the inside wall will be determined by the position of the internal rings; more specifically, it will be related to the local field strength at the surface of the wall. If the machine is viewed, for short time scales, as a superconducting can with a current inside of it, it can be seen that the current distribution on the outside of the wall will not match the image current distribution inside the wall. Thus, at the poloidal gap the current will flow in the poloidal direction in order for the distributions to match up. This will cause large field errors by introducing radial and toroidal components to the magnetic field

FIG. 2. Top view of machine (without lid) showing inner and outer walls, iron core cross-section, and one internal ring. (a) Without continuity windings, the image currents return on the outside of the walls. (b) With continuity windings, the image currents remain inside the machine and do not spread out at the gap.

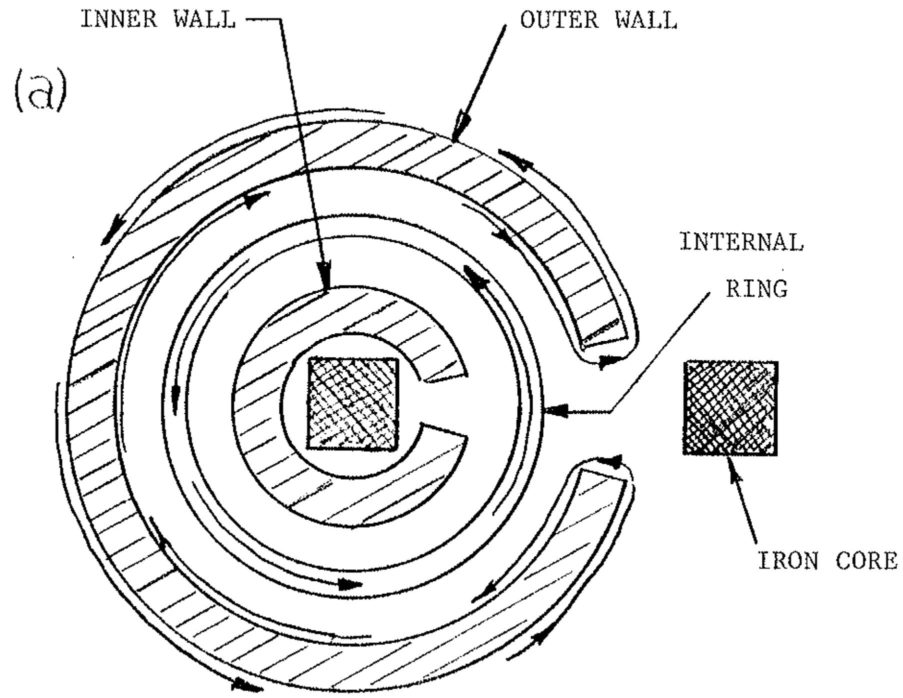
INNER WALL
OUTER WALL
(a)
INTERNAL RING
IRON CORE

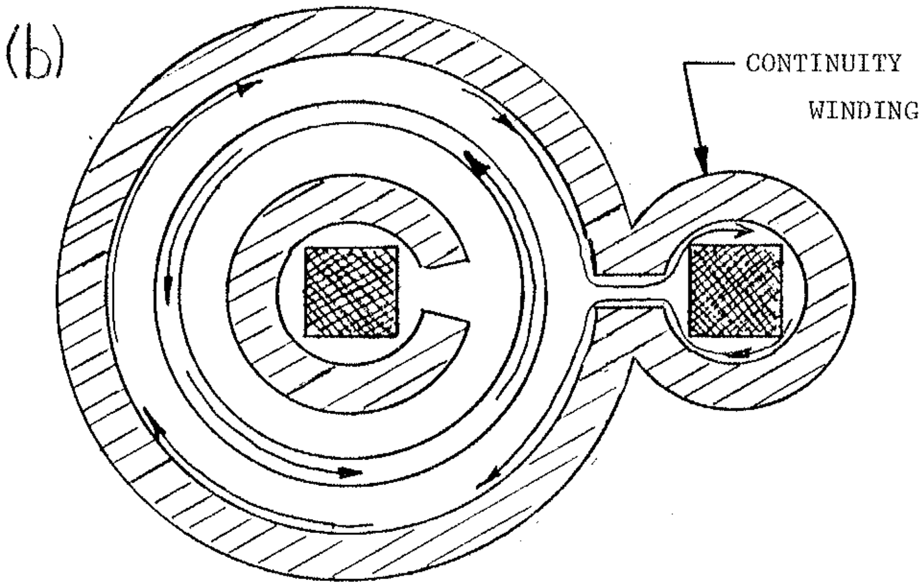
(b)
CONTINUITY WINDING

which was meant to be poloidal only. To prevent this problem, "continuity windings" were installed that continue the machine wall from one side of the gap around the outside of the iron core and then connect again to the wall on the other side of the gap (Fig. 2b). Thus, the wall is topologically outside the core so there is no inductive current in the wall due to driving the primary windings. However, there is now a path for the image current on the inside wall to follow when it reaches the gap. The number, poloidal placement, and resistance of each continuity winding (there is either one or one pair per primary winding) were individually determined to make the wall resistance look continuous across the gap. If this is not so, the wall currents, although still on the inner wall, will readjust their distribution at the gap and this implies a poloidal component of the current and hence a field error.

Drake[1] measured the field error at the gap error to be $\lesssim 2\%$ at all poloidal locations. This was recently confirmed by Sprott and Kellman.

The primary windings are fed from a 5 kV, 0.6 MJ capacitor bank. The magnetic field can be operated as a half sine wave pulse with a half period of 43 msec (Fig. 3). At 21.5 msec the capacitor bank voltage reverses and flux starts to leave the machine through the poloidal gap. Peak magnetic field occurs earlier than this, and depends on the exact location in the machine due to field soak-in effects. In the region between the outer hoop and wall, peak field occurs at 19.45 msec. The magnetic field can also be crowbarred, in

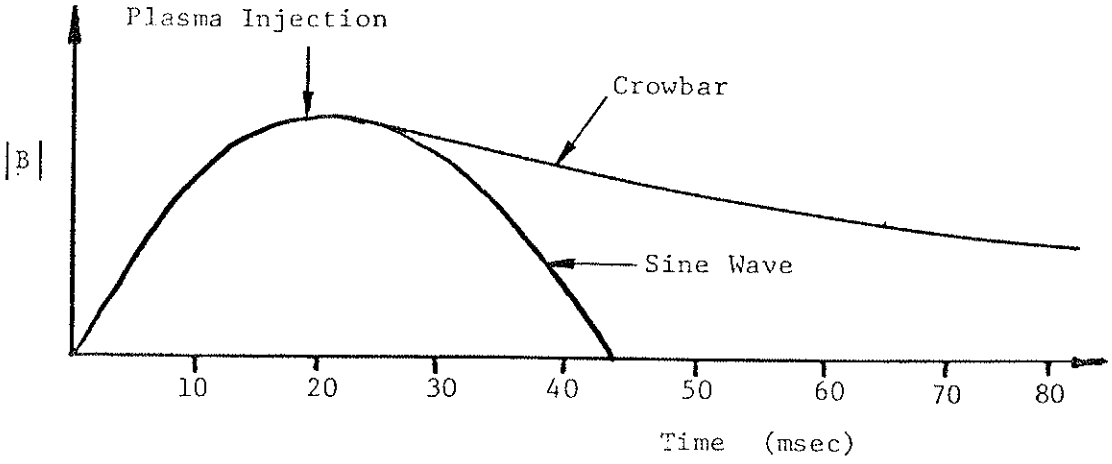

FIG. 3. Magnetic field pulse shape. Crowbar occurs slightly after peak field and plasma injection is typically near peak field.

which case, the voltage across the poloidal gap is clamped at zero when the capacitor banks are fully discharged and all the magnetic flux has entered the machine. Ideally, no flux could then leave the machine through the gap, however, in reality an ignitron switch is used to short out the capacitor bank, and the resistive losses in the ignitron and the primary windings allow some small voltage across the gap and thus some flux loss through the gap. The field also decays away due to resistive losses in the hoops and walls, and this results in a decay time of 70 msec for the field in crowbar mode (Fig. 3).

Figure 4 shows the contours of constant magnetic field, and Fig. 5 is the machine flux plot. Each "flux line" represents a toroidal surface of revolution such that any line drawn from the magnetic axis of an internal ring (position of zero field) to the flux line intercepts the same amount of poloidal flux. In the case of purely poloidal field these flux lines are the field lines as well. The separatrix field line (dashed line in Fig. 5) separates different types of regions of magnetic field. Inside the separatrix, the field lines encircle only one ring. This is called the private flux region, and all the field lines have absolute good curvature. Outside the separatrix, the field lines encircle all four rings; this is the common flux and since the field line curvature changes direction along the field line, each line has regions of good and bad curvature. Between the separatrix and the critical flux surface, ψ_{crit} (dotted and dashed line in Fig. 5), the

FIG. 4. Mod B plot in Octupole. Mod B contours are labeled in kilogauss. Note the large low field region in the center.

MOD B

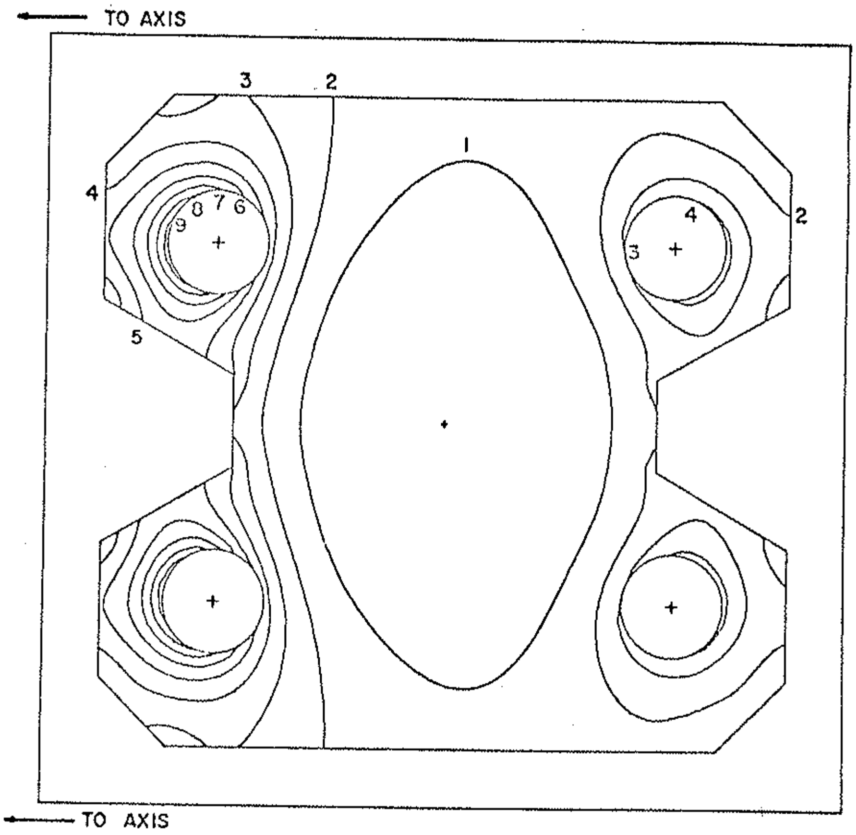

TIME = .025 SEC

FIG. 5. Poloidal magnetic flux plot of the Octupole, indicating the bad curvature region where β is evaluated. Flux lines are labeled in Dories with 10 Dories of total flux in the machine at full excitation. The dotted lines are the separatrices (the field null is degenerate), and the last stable flux surface, Ψ_{crit}, is the dot-dash line.

OCTUPOLE FLUX PLOT

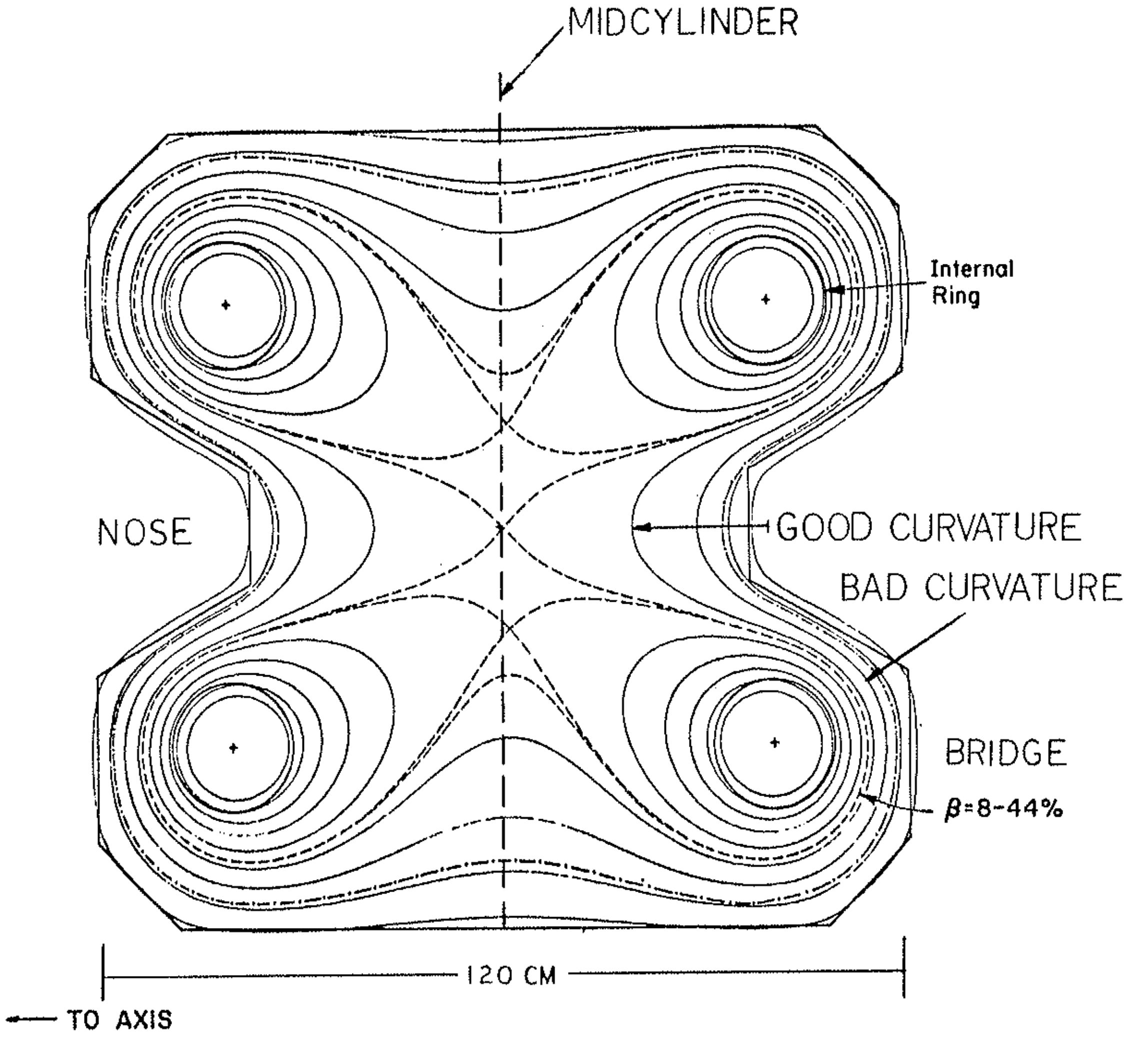

TIME = .025 SEC

field lines have average good curvature. Outside of ψ_{crit}, there is average bad curvature, and this is characterized by being unstable to MHD interchange modes.

Various terms used throughout this paper refer to specific parts of the machine. These are labeled in Fig. 5. The "bridge" region is the region between the ring and wall; the "nose" is the region near the indented surfaces on the inner and outer wall; the "midcylinder" is the vertical surface passing through the center of the vacuum region. The standard system of magnetic flux coordinates are used in this paper. This is a right-handed coordinate system (ψ, χ, ϕ) where ψ is the direction perpendicular to flux surfaces and is equal to $1/2\pi$ times the poloidal flux contained within the surface, χ measures along field lines, and ϕ is the toroidal angle. The flux lines are labeled, in units called Dories, from ψ=0 to ψ=10 Dories with zero being at the magnetic axis of the rings and 10 being at the outermost flux surface at peak magnetic field. At 25 msec the surface of the outer ring, separatrix, and critical flux surface are located at ψ=2.4, 5.7, and 7.8 Dories respectively.

A weak toroidal magnetic field is obtained by flowing current poloidally through the machine walls. Fourty-four cables uniformly distribute the current around the machine toroidally, and an insulated toroidal gap makes the machine wall a one-turn solenoid. This field has a 1/R dependence, where R is the major radius, and its maximum value on the midcylinder with the present capacitor bank is 450 G.

The base vacuum pressure is 1×10^{-8} T. This is achieved with two turbomolecular pumps, a liquid helium cryopanel and extensive use of titanium gettering. Neither the turbomolecular pump or cryopanel do any significant pumping during a plasma shot compared to the titanium coating on the wall. The titanium covers approximately 75% of the surface area in the machine, and with a fresh layer of titanium a pumping speed of 380,000 liters per second has been measured for hydrogen.

A unique feature of the Octupole is that the sixteen supports for the external rings can be withdrawn before the plasma is injected and reinserted 20-30 msec later leaving the rings unsupported or "levitated" for that time. This allows one to perform an experiment (typically 1-10 msec) without metallic supports crossing the plasma region

A complete summary of important machine parameters is listed in Table 1.

2.B. Plasma Sources

The primary sources of plasma in this experiment were three coaxial Marshall guns[2]. Ohmic discharges and a combination of ohmic and gun plasmas were tried but will not be reported here. Plasma guns have long been a source of plasma on the Octupole and thus are fully described in previous literature. For a list of references on construction and operation of these guns and the process of cross field injection and trapping of the plasma in the Octupole magnetic

Table I

Operating Parameters of the Levitated Octupole*

	Wall	Inner Hoop	Outer Hoop
Current**	1.4×10^6 A	0.5×10^6 A	0.25×10^6 A
B max (at surface)**	6 kG	12. kG	5.5 kG
B_T (center of toroid)	768 G		

Energy of Pulse	0.6×10^6 J
Total Peak Core Flux	0.72 Wb
Inductance L: $L = N^2 L_o$, $N = 90$, L_o =	0.6 μH (calculated)
Capacitance	0.048 F
Volume of Vacuum Region	8.6 m^3
Volume inside ψ-critical @ 20 msec	7.7 m^3
Hoop Minor Radius	8.9 cm
Inner Hoop Major Radius	0.99 m
Outer Hoop Major Radius	1.79 m
Half sine Period (B_P)	43 msec
Half sine Period ($B_P + B_T$)	47 msec
Crowbar time	25 msec
Crowbarred field decay time	65-90 msec

*All parameters are for full amplitude at 20 msec.

**Approximate values.

field see the paper by Kellman[3]. In order to obtain the high beta plasmas for this experiment certain modifications were made to existing guns and a new gun was built. The modifications and new equipment will be described below.

2.B.1. Big Gun

There are two "big guns" used in this experiment which have essentially the same design and associated hardware. The mechanical construction of the gun is shown in Fig. 6. Hydrogen gas is puffed into the region between the inner and outer electrodes (parts #1 and #2) by retracting the acoustic rod (#3) from the teflon vacuum seat (#4) and allowing the gas to flow from a 1 cc plenum through the slots in the inner electrode. After a delay of several hundred microseconds, a high voltage capacitor bank is connected between two electrodes. A breakdown occurs in the hydrogen gas allowing current to flow between the two electrodes and creating a magnetic field between the electrodes. The resultant j×B force propells the plasma out of the gun. As the plasma is accelerating out of the gun, it ionizes the gas it encounters, building up the plasma density as it progresses until finally leaving the gun. In order to produce the high beta plasma required in this experiment, the plasma density and temperature had to be increased. Typically, this type of gun produces a majority of the plasma with low $T_i \sim 50$ eV and T_e below that. A small fraction (~1%) of the plasma has an energy in excess of 1 kV and thus contains a significant fraction of the energy;

FIG. 6. Mechanical diagram of plasma gun - Big Gun #2. All three guns have similar design with only small modifications.

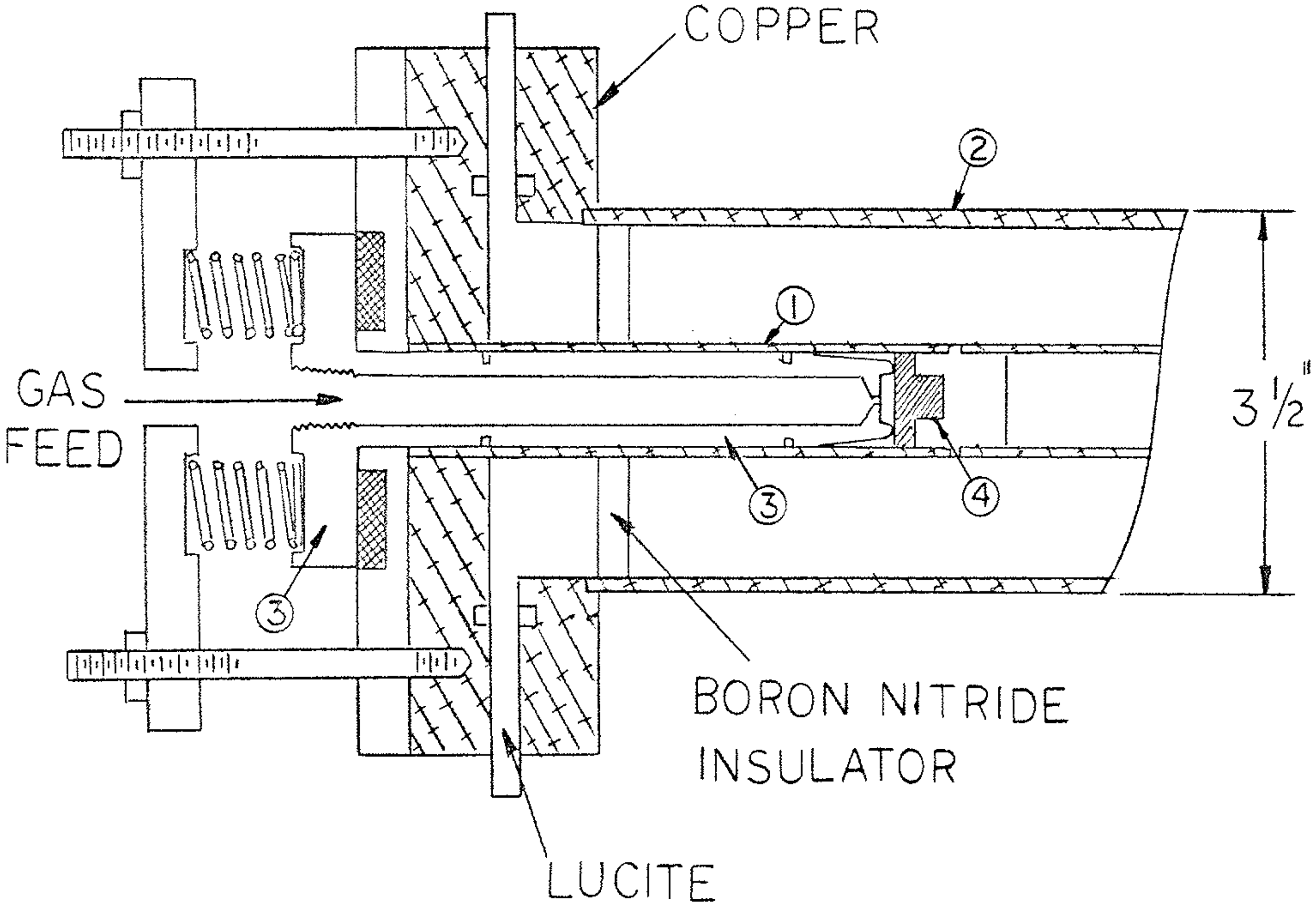
COPPER
②
①
GAS
FEED
3 1/2"
③
④
③
BORON NITRIDE
INSULATOR
LUCITE

however, these particles are not well confined at low magnetic field, and the temperature decays very rapidly for the fraction that is confined. Thus, the high beta results are achieved by increasing plasma density, and this requires additional energy in the gun capacitor bank. The higher energy bank required an upgrade of the switches and transmission line to handle the higher current. The upgraded system is shown in Fig. 7. A 20 kV, 100 μF capacitor bank is connected to the gun through a 1/4" aluminum parallel plate transmission line. The power is switched through a low inductance rail gap switch capable of handling currents up to 1 MA (Fig. 8a). The rail gap is used instead of a spark gap because it allows multiple arc closures along the rails and thus reduces the switch inductance as well as the current density in each arc channel which increases the switch life. The rail gap is triggered by a 30 kV trigger from a smaller spark gap switch (Fig. 8b). Both the inductance and resistance were variable by adjusting the separation of the transmission line plates and by the addition of an adjustable length 0.010" stainless steel strip in the transmission line.

Figure 9 shows a typical transmission line current waveform. The rise time of the waveform is less than one-quarter of the period of oscillation because the gun inductance is low when the current is located near the input terminals, and thus little magnetic flux is contained between the electrodes. The plasma typically leaves the gun near the time of peak current, and this is seen as a "glitch" on the current trace. There is an accompanying inductive voltage spike

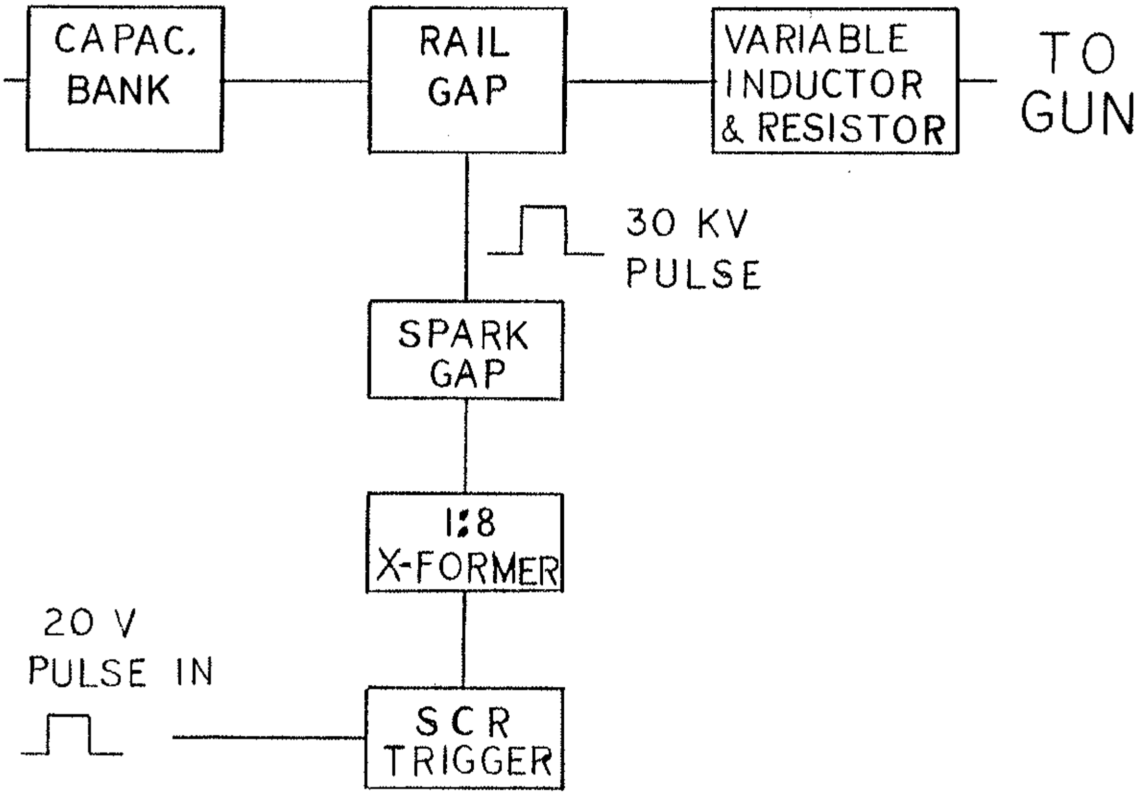

CAPACITANCE:	100 fd @20 KV, $1/2CV^2 = 20$ KJ
INDUCTANCE:	$L_{Bank} + L_{X\text{-}Line} = 50$ nH $L_{Gun} = 0 - 175$ nH
RESISTANCE:	0.02 Ω
CURRENT:	0.5 MA peak
PERIOD:	30 μsec Rise time - 4 - 5 μsec

FIG. 7. Block electrical diagram of charging and trigger circuitry for the plasma guns. The capacitor bank discharges through the high current rail gap switch which is triggered by a 30KV pulse.

FIG. 8. Schematic drawing of (a) rail gap switch. This is used for switching the gun capacitor bank instead of the (b) spark gap switch because the multiple arc channels in the rail gap give a lower inductance. The spark gap is used in the low current trigger circuitry.

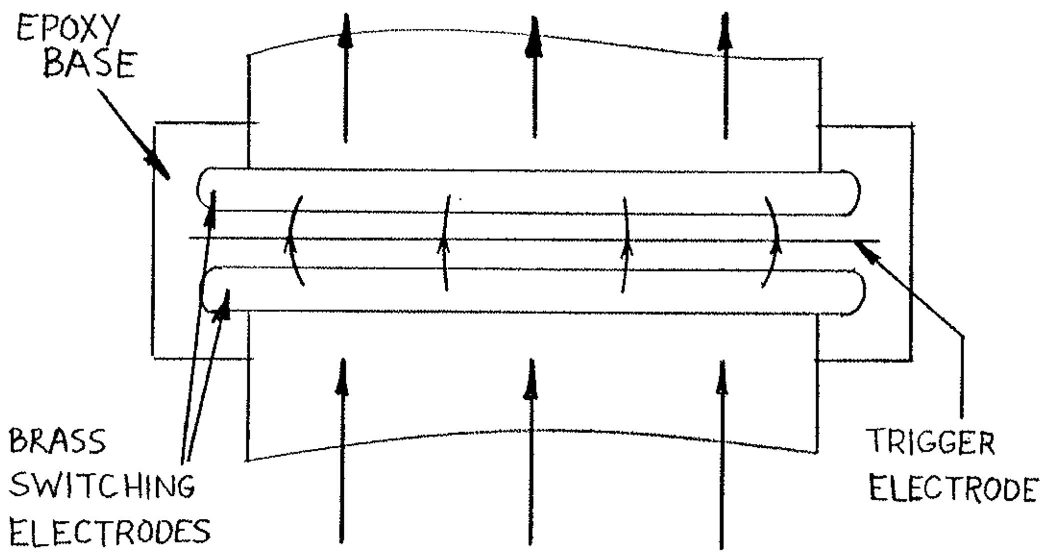

RAIL GAP

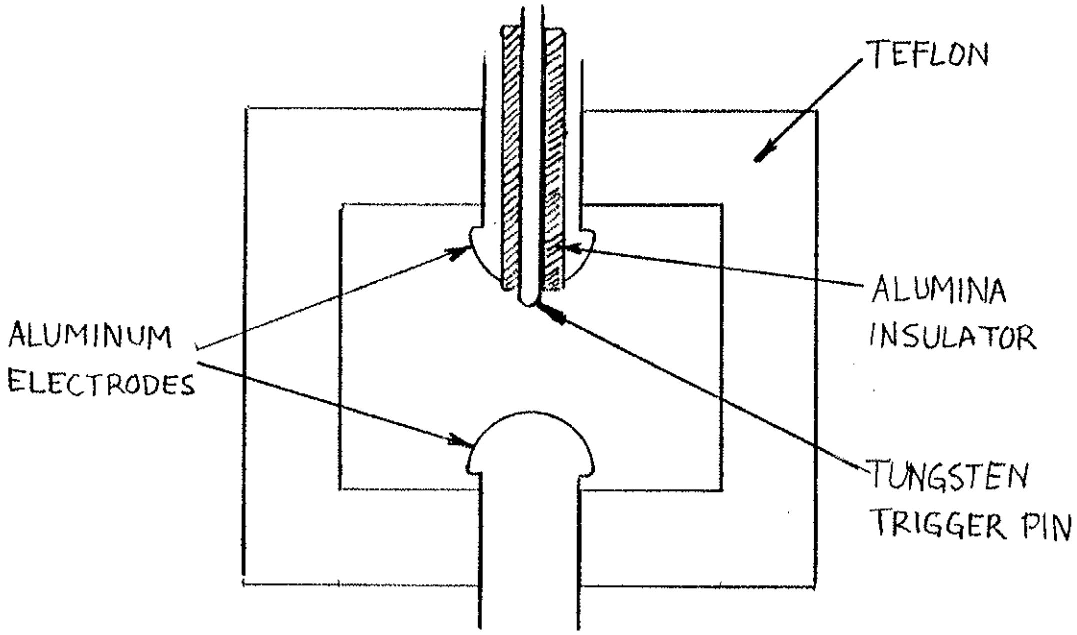

SPARK GAP

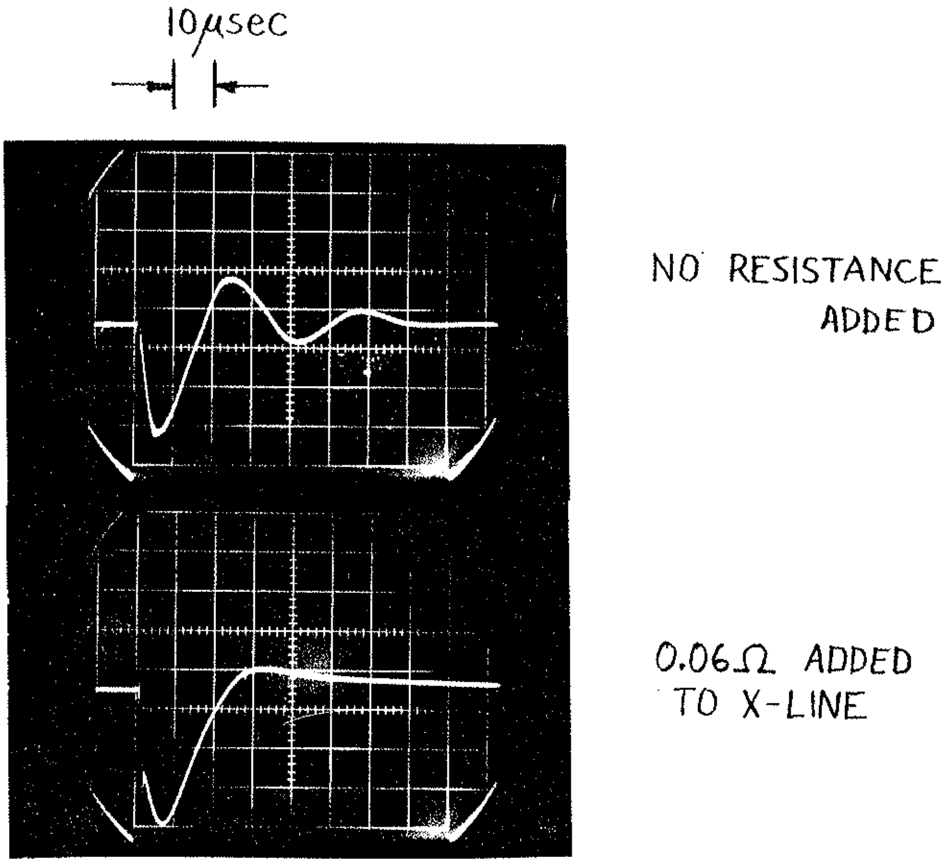

FIG. 9. Current waveform in transmission line. (a) Current underdamped. (b) Resistance added to nearly critically damp the current. Plasma typically leaves the gun barrel near peak current. The "glitch" has been filtered out for clarity.

which prevents the current from going to zero when the plasma leaves the gun by causing the arc to restrike within the gun barrel.

Magnetic field measurements taken inside the gun in the region between the gun barrels indicate the distribution of current in the gun as well as the position of the leading edge of the current as a function of time. With the capacitor bank charged to 16 kV, these measurements indicate that the plasma in the leading edge of the current is continually accelerated while inside the gun, and exits the gun with a velocity of 27 cm/μsec or approximately 400 eV directed energy (Fig. 10). At 12 kV, the behavior was similar, but the exit velocity was decreased to 20 cm/μsec or 200 eV.

Measurements of the magnetic field strength at different positions in the gun (Fig. 11) indicate that the current is not confined to a thin sheet that remains intact as it moves down the barrel (current density is proportional to the derivative of the magnetic field strength). Although there is some indication of a current sheet[4] early in the acceleration process, there is always some current behind this sheet, and as time progresses the distribution might best be described as uniform.

When installed on the Octupole these big guns are each capable of producing plasma densities of 5×10^{13} cm^{-3} and electron and ion temperatures of 40 eV.

2.B.2. Intermediate Density Gun

FIG. 10. (a) Velocity of the leading edge of the current distribution in the gun. (b)Position of leading edge versus time. The measurement is taken with a magnetic probe placed inside the gun electrodes.

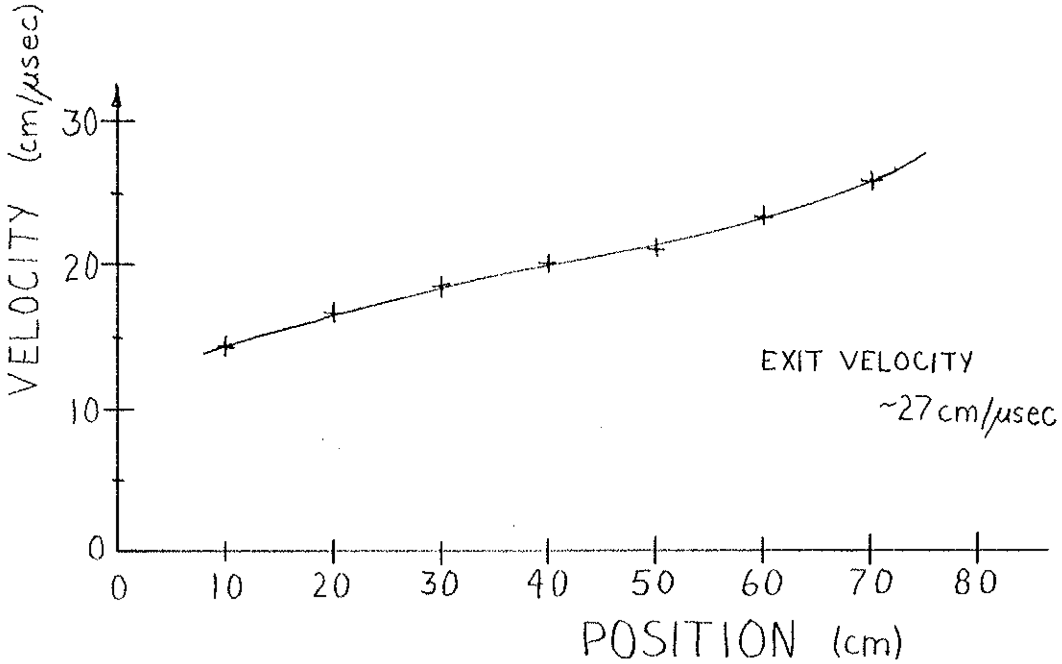
VELOCITY (cm/μsec)
30
20
10
0
0
10
20
30
40
50
60
70
80
POSITION (cm)
EXIT VELOCITY
~27 cm/μsec

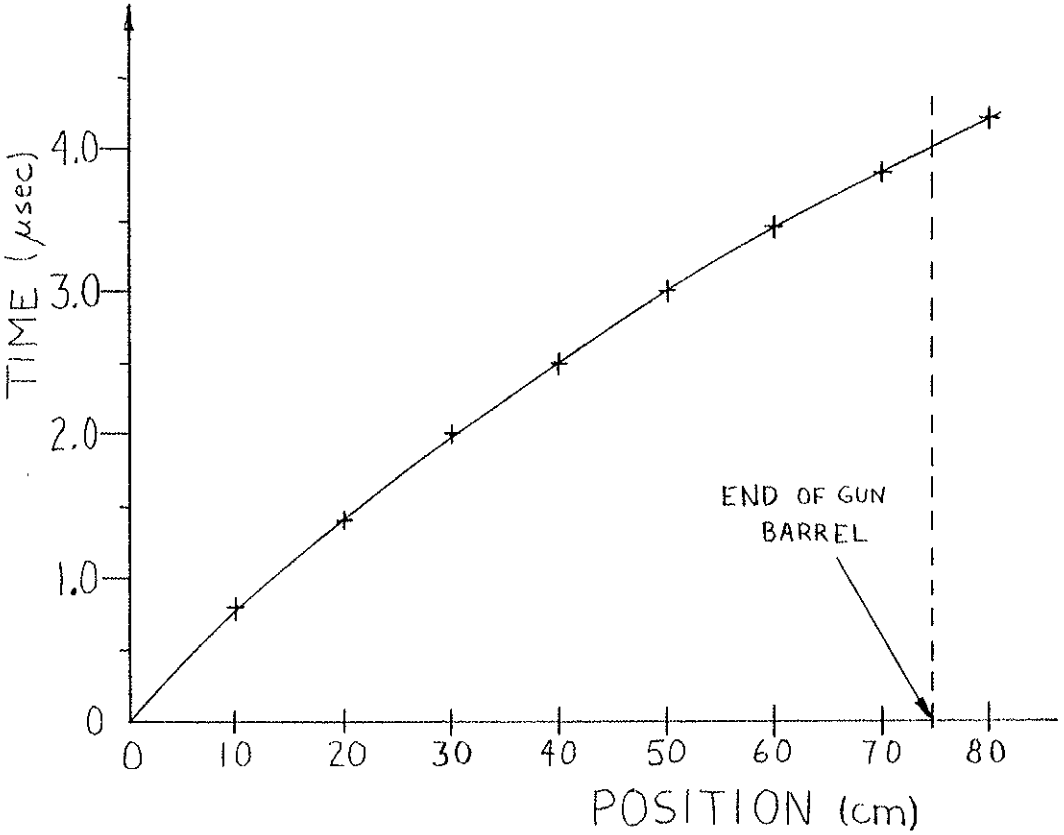
TIME (μsec)
4.0
3.0
2.0
1.0
0
0
10
20
30
40
50
60
70
80
POSITION (cm)
END OF GUN
BARREL

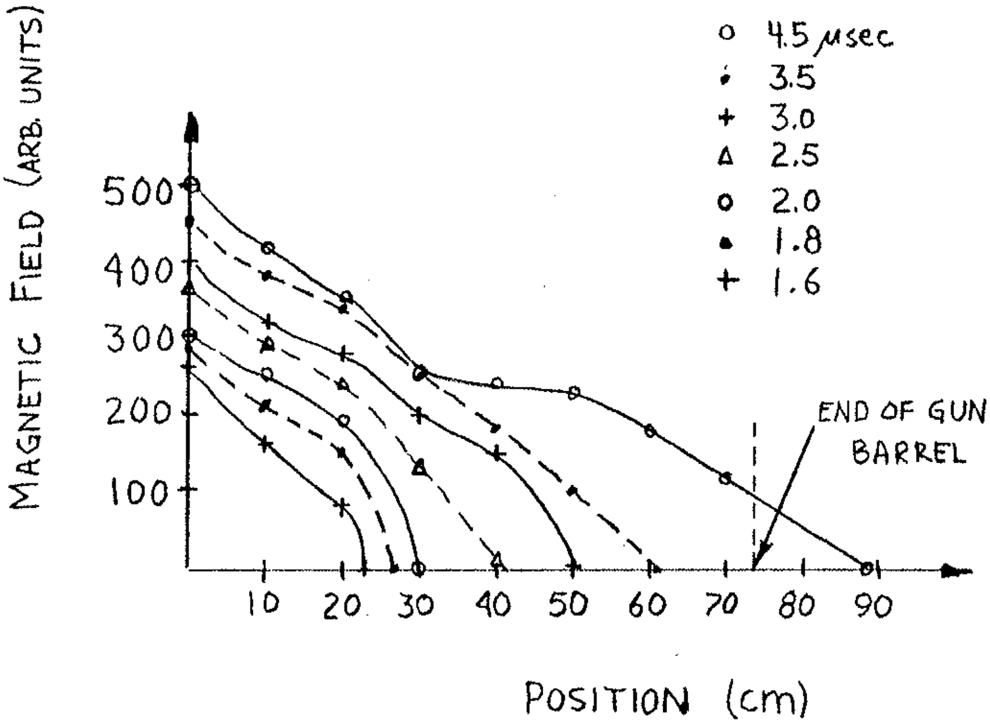

FIG. 11. Magnetic field distribution inside plasma gun at different times from the time of firing (t=0.0 μsec). This field structure indicates only a slight peak in the current distribution at the leading edge, followed by a more uniform distribution.

This is just a smaller version of the big guns. It has an adjustable size gas plenum (0-0.5 cc), a 6 kJ, 20 kV capacitor bank and is capable of producing 2×10^{13} cm^{-3} and $T_e \sim T_i \sim 40$ eV. An additional gun, the "small gun" which produced a low density plasma 10^8-10^{10} cm^{-3} was not used in this experiment.

2.C. Diagnostics

2.C.1. Langmuir probe

This is a brief summary of the main points of electrostatic probe theory relevant to the use of probes in this experiment and of the plasma parameters that can be measured using probes. For a more complete description of the theory see the article by Chen[5], and for a complete treatment of practical electronics for probes see Sprott[6].

An ungrounded piece of metal inserted into a plasma will reach a steady state "floating potential", V_f, such that the there is no net current to the metal, i.e. the ion and electron fluxes are equal. If the probe is biased positive or negative with respect V_f, it will attract or repel electrons or ions and will draw a net current. If the probe is biased negatively enough, no electrons are collected and all the ions traversing the effective probe area, A, (equal to the actual area if we neglect the plasma sheath) will be collected. The expression for this "ion saturation current" is

$$I_{si} = \frac{1}{4} neAv^* \qquad \text{where } v^* = [\frac{8kT_e}{\pi m_i}]^{1/2} \qquad T_i \leq T_e \quad ,$$

and n, m_i, T_i, and T_e are the ion density, ion mass, ion temperature, and electron temperature respectively.

Thus the density can be determined if the area of the probe tips and the electron temperature is known. In practice this is used only for relative density measurements, and an absolute calibration is determined by other means.

It can be shown that for a single tipped probe, the slope of the current voltage characteristic at the floating potential is given by

$$\frac{dI}{dV}\bigg|_{V_f} = \frac{eI_{si}}{kT_e} \quad .$$

Thus to determine the electron temperature, we can plot the full I-V curve either by point by point measurements taken on different shots or by sweeping the bias voltage fast enough that the electron temperature does not change significantly during the sweep.

Typically, a bias voltage of a few times the electron temperature assures that the probe is collecting the ion saturation current. If, however, there are large floating potential variations (on the order of the bias potential) the probe might not always be collecting saturation current since the bias voltage is set with respect to ground and not the floating potential. Alternatively, if an I-V characteristic is being measured and the plasma potential is changing with time either because of fluctuations or plasma decay, it is difficult to maintain a constant probe to plasma potential difference. To prevent this problem, a floating double probe has been used throughout most of this research. For this probe, two probe tips biased relative to each other are not referenced to ground potential. The entire systems "floats" and can follow changes in the plasma potential. It can be shown that if the two tips have equal area then the total current to the probe is

$$I = I_{si} \tanh (eV/2kT_e)$$

where I_{si} is the ion saturation current for a single probe tip and V is the potential difference between tips. Thus, as for the single probe, we can determine the electron temperature by measuring the slope of the I-V characteristic at V=0. For the more general case of unequal tip areas,

$$\left.\frac{dI}{dV}\right|_{V=0} = \frac{e}{kT_e} \left[\frac{I_{si1}\, I_{si2}}{I_{si1}+I_{si2}}\right] .$$

An alternative method[7] of determining the electron temperature, also based on measuring the slope of the I-V curve at V_f, can be used to obtain a continuous measure of the temperature by measuring the admittance, Y, defined as

$$Y = \frac{1}{R} = \frac{dI}{dV}\Big|_{V_f} = \frac{eI_{si}}{kT_e} \quad .$$

The admittance can be measured by use of a capacitance bridge that is balanced for zero output signal in the absence of plasma. The addition of plasma unbalances the bridge and if the output of the bridge is calibrated against known resistances, the admittance or inverse resistance of the plasma sheath can be determined. The electron temperature can be determined if the ion saturation current is measured simultaneously. It is crucial that the area of the probe tip used for measurement of I_{si} and Y are the same size and shape. Much of the electron temperature data in this research used this technique. A triple tipped probe was used, with one tip for admittance and the other two serving as a floating double probe for measuring ion saturation current. The agreement is very good between the electron temperature determined using this admittance method and by direct measurement of the slope from point by point data.

Floating potential measurements are particularly simple with a single probe and are obtained by measuring the voltage across a high impedance termination, such as the 1 MΩ input impedance of an oscilloscope.

The terminating impedance should be much larger than the plasma sheath resistance, R_s, but this is easily satisfied in low temperature, high density plasmas where R_s is typically less than 100-1000 Ω.

Measurement of the electric field, E, can be obtained using the relationship between plasma potential and floating potential,

$$V_p = V_f + \frac{kT_e}{2e} \ln\left(\frac{m_i}{m_e}\right) \quad \text{for} \quad T_i = T_e$$

$$E = -\nabla V_p = -\nabla V_f - 3.8\nabla\left(\frac{kT_e}{e}\right) \quad .$$

Thus, if we neglect any fluctuation in the temperature gradient, the fluctuating electric field is just the fluctuation in the floating potential gradient.

2.C.2. Ion Temperature Probe

Ion temperature measurements were performed using an electrostatic ion energy analyzer that was mounted on a 1/4" diameter probe.[8] The probe has three grids and a collector (Fig. 5). The first grid in contact with the plasma is at the floating potential. Behind this is the discriminator grid biased positive with respect to the ground. This only permits ions with energy $E > V_{discrim} - V_{plasma}$ to be collected. The third grid is biased negatively with respect to the grids and collector to repel incoming electrons and also to suppress secondary electrons emitted from ion impact on the collector. The collector is biased negatively to collect ion current. Collector current is monitored as a function of the discriminator voltage, and the ion temperature is calculated from the relationship $\frac{d\ell nI}{dV} = \frac{e}{T_i}$.

2.C.3. Charge Exchange Analyzer

For a complete description of this diagnostic see Fortgang[9]. This device measures the ion temperature by looking at the fast neutral flux coming out of the plasma. Fast plasma ions charge exchange off of neutral gas in the plasma and turn into fast neutrals. These freely move through the magnetic field and can be detected externally by reconverting them to fast ions in a nitrogen stripping cell through the reaction $H^o+N_2^o \rightarrow H^+ + N_2^-$. The resultant fast ions can now be detected, and their energy is measured using a curved plate electrostatic energy analyzer. This allows the reconstruction of the ion energy distribution from which the ion temperature can be determined. There is a lower limit on the temperature that can be reliably determined since there is a strong energy dependence of the stripping reaction and the cross section is not well known below 150 eV. Thus, only the high energy part of a low temperature ion distribution can be measured. Typically, the lowest temperature that can be determined is ~40 eV.

This device was only of limited use in this experiment for two reasons. The ion temperature of the gun plasmas decayed very quickly after injection, and thus charge exchange measurements could only be obtained for the first 100-200 μsec. Secondly, at high enough plasma densities, the fast neutrals leaving the plasma may not be representative of the bulk ion temperature but only of the temperature near the plasma edge. Consider the case where the central ion temperature is 100 eV, the electron temperature is 25 eV, and the plasma density is 5×10^{13} cm^{-3}. A charge exchange neutral created at the plasma center will have a mean free path for ionization of 15.6 cm and thus will probably not make it out of the central region. More importantly, at these parameters, a neutral coming in from the wall at room temperature has a mean free path for ionization of 0.25 cm. Thus, there will be a strong neutral pressure profile across the plasma, and the flux of charge exchange neutrals from the central or burned out regions will be strongly reduced because of the lack of neutral particles.

2.C.4. Interferometer

Plasma density is measured with a 70 GHz microwave interferometer[10] that views the plasma along the midcylinder. Because most of the path along the midcylinder is between two separatrices (see Fig. 5), the interferometer essentially measures the density on the separatrix. For 70 GHz, the maximum plasma density through which the beam will propagate is given by

$$N_{crit} = \frac{m_e \omega^2}{4\pi e^2} = 6.08 \times 10^{13} \text{ cm}^{-3} \quad .$$

Basically, the system measures the phase shift of a microwave beam propagated through the plasma relative to a beam in a reference leg. When the plasma is injected, the index of refraction changes because it depends on the plasma density. This causes a phase shift between the plasma leg and the reference leg, and digital circuitry converts the phase shift to an analog output which is proportional to plasma density. The calibration depends on the electronics and the microwave hardware, and for this interferometer is 2×10^{13} cm^{-3}/volt. Two corrections are necessary.

(i) The index of refraction is given by the expression

$$n = \left(1 - \frac{N}{N_{crit}}\right)^{1/2}$$

where N is the plasma density and N_{crit} is the critical density at cutoff. If $N/N_{crit} \ll 1$ then we can linearize this relation, and since the phase shift is proportional to the change in the index of refraction, it is also proportional to the change in plasma density. Thus, when the digital circuit counts the number of fringes (2π of phase shift per fringe), its output voltage is proportional to density. When we are near cutoff, the above linearization is not valid. Near cutoff, the phase shift per unit change in density increases, and the value for the density is too high. Using the exact expression for the index of refraction, we find that the actual density, N, is related to the density measured by the interferometer, N_m by the expression,

$$N = N_M(1-N_M/4N_{crit}) \quad .$$

(ii) For densities far below the cutoff density, the interferometer output is proportional to the line averaged density along the midcylinder. Although most of the plasma along the midcylinder is at the separatrix density, significant difference in the shape of the density profile off of the separatrix will alter the relationship between interferometer output and the separatrix density. The interferometer output is proportional to the phase shift which can be related to the line averaged density by

$$\Delta\phi = \frac{2\pi}{\lambda}\frac{1}{N_{crit}}\int_0^{\ell} N(x)dx$$

where ℓ is the total length in the plasma. If we define a normalized profile, f(x), with a peak value of unity on the separatrix, then

$$N(x) = N_{sep}\ f(x)$$

and

$$\Delta\phi = \frac{2\pi}{\lambda}\frac{N_{sep}}{N_{crit}}\int_{0}^{\ell} f(x)dx \quad .$$

For our interferometer[11] a phase shift of 2π corresponds to a density of 8×10^{11} cm^{-3}. Thus, we can solve for the value of the integral,

$$\int_{0}^{\ell} f(x)dx = 65.1 \text{ cm} \quad .$$

If the profile shape is of the form

$$f(\psi) = \exp\left[-\left(\frac{\psi-\psi_{sep}}{\sigma}\right)^{2}\right] \quad ,$$

then the value of the integral yields a value of σ=0.64 Dories. Density profiles with a different value for this line integral require adjustment of the interferometer calibration to determine the actual separatrix density.

2.C.5. Magnetic probes

Magnetic probes are used to measure the vacuum magnetic field, the plasma diamagnetic perturbation to the vacuum field and magnetic fluctuations. The principal type of magnetic probe used in this experiment is a B-dot probe which consists of a multiturn coil which puts out a signal proportional to the time rate of change of magnetic flux through the coil. A number of different variations on this basic probe were used in this experiment. Most of the early data on plasma diamagnetic perturbations to the vacuum field were obtained with one type of probe. The 300 turn coil was inserted into a 1/4" diameter grounded stainless steel tube that was welded closed at the end inserted into the plasma. Because the probe had problems with electrostatic pickup, the coil was center tapped with the two sections wound in opposite directions. The center tap was grounded, and the signal measured differentially thus eliminating the electrostatic part of the signal. The signal was integrated with a passive RC network. The RC time was chosen to be much longer than the signal frequency; RC=500 msec for the main vacuum field pulse and 10 msec for the field perturbation due to the plasma. This latter signal typically had rise times of 100-200 μsec and decay rates of 500 μsec.

More recent data taken on magnetic fluctuations has been taken using a probe that substituted a glass tube for the outer stainless steel housing. Electrostatic shielding was provided by enclosing the wires in a stainless steel tube which fit inside the glass tube. The shield was continued around the tip of the coil by wrapping it with .001"-.002" aluminum foil. This coil did not have problems with electrostatic pickup and thus it was not center tapped.

Magnetic field measurements were also made inside the plasma gun. These used a probe identical in design to the second one described above except that a small slit was cut in the aluminum foil surrounding the coil to allow field penetration. The time scales for these signals were very short (rise time <1 μsec), and a continuous foil strip would have decreased the frequency response of the probe. Only five turns were used in this coil since the signal sizes were so large inside the gun.

2.C.6. Spectroscopic Diagnostics

Doppler Broadening

The wavelength shift of radiation emitted from a particle moving at a speed v in the direction of observation is

$$\Delta\lambda_D = \frac{v}{c}\lambda \qquad (v \ll c)$$

where λ is the unshifted wavelength. In a plasma with a Maxwellian distribution of velocities, the intensity of radiation emitted $\delta\lambda$ away from the unshifted wavelength is given by[12]

$$I(\Delta\lambda) = \frac{I_1}{\pi^{1/2}\Delta\lambda_D} \exp\left[-\left(\frac{\Delta\lambda}{\Delta\lambda_D}\right)^2\right]$$

where I_1 is the total line intensity. Thus for a hydrogen plasma with temperature T, the full width at half maximum intensity is given by

$$\Delta\lambda(\text{Å})_{1/2} = 7.71 \times 10^{-5}\ \lambda(\text{Å})T_i^{1/2}(\text{ev}).$$

$\Delta\lambda_{1/2}$ is 0.7Å for the H_β line in a 4 eV plasma. Measurement of the line intensity, $I(\Delta\lambda)$, was performed with a Jarrell-Ash monochromator[13] which had a resolution of 0.1-0.2Å.

VUV Monochromator

This device had a resolution of ~1Å and was used to monitor various impurity lines during the optimization of the plasma gun.

Various other spectroscopic signals were routinely monitored to check on plasma reproducibility. These included H_β(4861Å), CIII 4647Å, OIII 3760Å, and NIII 4515Å.

2.D. Fluctuation Measurement Techniques

This section describes both the experimental and computational techniques used to measure fluctuating plasma quantities.

The quantities of interest, density, potential, electric field, and magnetic field are measured in the range of 20-160 kHz. Three-pole Butterworth filters are used to filter out the low and high frequencies. The high frequency filter is used to avoid "aliasing" which occurs when there are frequency components in the signal which are above the Nyquist frequency (f_N=1/2Δt), where Δt is data sampling interval. For $\Delta t=2$ μsec, $f_N=250$ kHz. Since at the Nyquist frequency no information about the magnitude of the frequency component can be determined, the actual upper frequency used is below f_N. Most data is data taken with $\Delta t=1$ μsec, so $f_N=500$ kHz.

There are two main techniques for determining the frequency characteristics or the power spectrum, $P(\omega)$, of a fluctuating signal: the Blackman-Tukey method using correlation functions, and direct determination of the power spectrum using the Fast Fourier Transform (FFT). Both of these methods, as well as other numerical methods for treatment of digitized signals, are well discussed in the literature and will not be reviewed here[14,15,16]. Using the FFT method, both the power spectrum and the cross power spectrum of two different signals are easily obtainable, and this method has been used for all the data in the experiment. All raw data have their mean value and a linear fit subtracted out and are then multiplied by either a Hann function or a cosine taper to make the signals periodic and reduce leakage[14]. The power or cross power spectrum is then determined. Given the power spectrum, the total power, P, is simply

$$P = \int_{-\infty}^{+\infty} P(\omega)d\omega = \int_{-\infty}^{+\infty} |F(\omega)F^*(\omega)|d\omega$$

where $F(\omega)$ is the Fourier Transform of the signal. It is important to note that the power is proportional to the square of the signal amplitude.

Since the frequency resolution of the power spectrum is $\Delta f_R=1/T$, where T is the total time for sampling, T should be made as large as possible. In this experiment, however, the plasma is decaying and often the frequency spectrum changes with time. Thus, if T is too large, the results are not meaningful. In general if the frequency of a mode changes by more than Δf_R in a time T, then the sampling time T should be reduced.

In order to compare two different power spectra, a frequency correlation coefficient is defined as,

$$\eta(\omega) = \frac{|F_1^*(\omega)F_2(\omega)|}{[(F_1(\omega)F_1^*(\omega))(F_2^*(\omega)F_2(\omega)]^{1/2}} = \frac{P_{12}(\omega)}{[P_1(\omega)P_2(\omega)]^{1/2}}$$

where F_1 and F_2 are the Fourier Transforms of the two signals and thus $\eta(\omega)$ is just a "normalized" cross power spectrum. It can be shown that as defined, $\eta(\omega)=1$ for all ω. To make this a meaningful quantity, it is redefined such that the three terms are averaged over a frequency interval $\Delta\omega$ about ω before they are combined in $\eta(\omega)$, i.e.

$$\eta(\omega) = \frac{\langle P_{12}(\omega)\rangle}{[\langle P_1(\omega)\rangle\langle P_2(\omega)\rangle]^{1/2}}$$

where <•••> indicates a frequency average. Thus, $\eta(\omega)$ indicates the degree of similarity of two power spectra within a frequency interval, independent of the phase. If the frequency interval chosen is the entire frequency range measured, then this total or integrated correlation coefficient, η, indicates the similarity of the two power spectra. The maximum value of $\eta(\omega)$ or η is unity indicating maximum correlation.

2.E. Timing and Data Handling

Figure 12 shows a typical timing sequence. If toroidal field is desired, it is triggered at $t=0$ with the poloidal field. Both fields have the same period so the ratio of their amplitudes remains constant.

Early data were taken on oscilloscope and stored on Poloroid film. Currently, all data is taken on the computer. The two types of digitizers used are LeCroy models 8210 and 2264. The 8210 is a 4 channel, bipolar, 10 bit digitizer that can digitize at up to 1 μsec per sample. Each 8210 has 32 K memory to be divided among the number of channels used. The 2264 is an 8 channel, bipolar, 8 bit digitizer with a maximum sampling rate of 0.25 μsec per sample. Because the resolution of the 2264 is only 8 bits, it is typically used for routine monitoring of spectroscopic diagnostics. For both digitizers, data sampling is done simultaneously on all channels.

FIG. 12. Typical timing sequence.

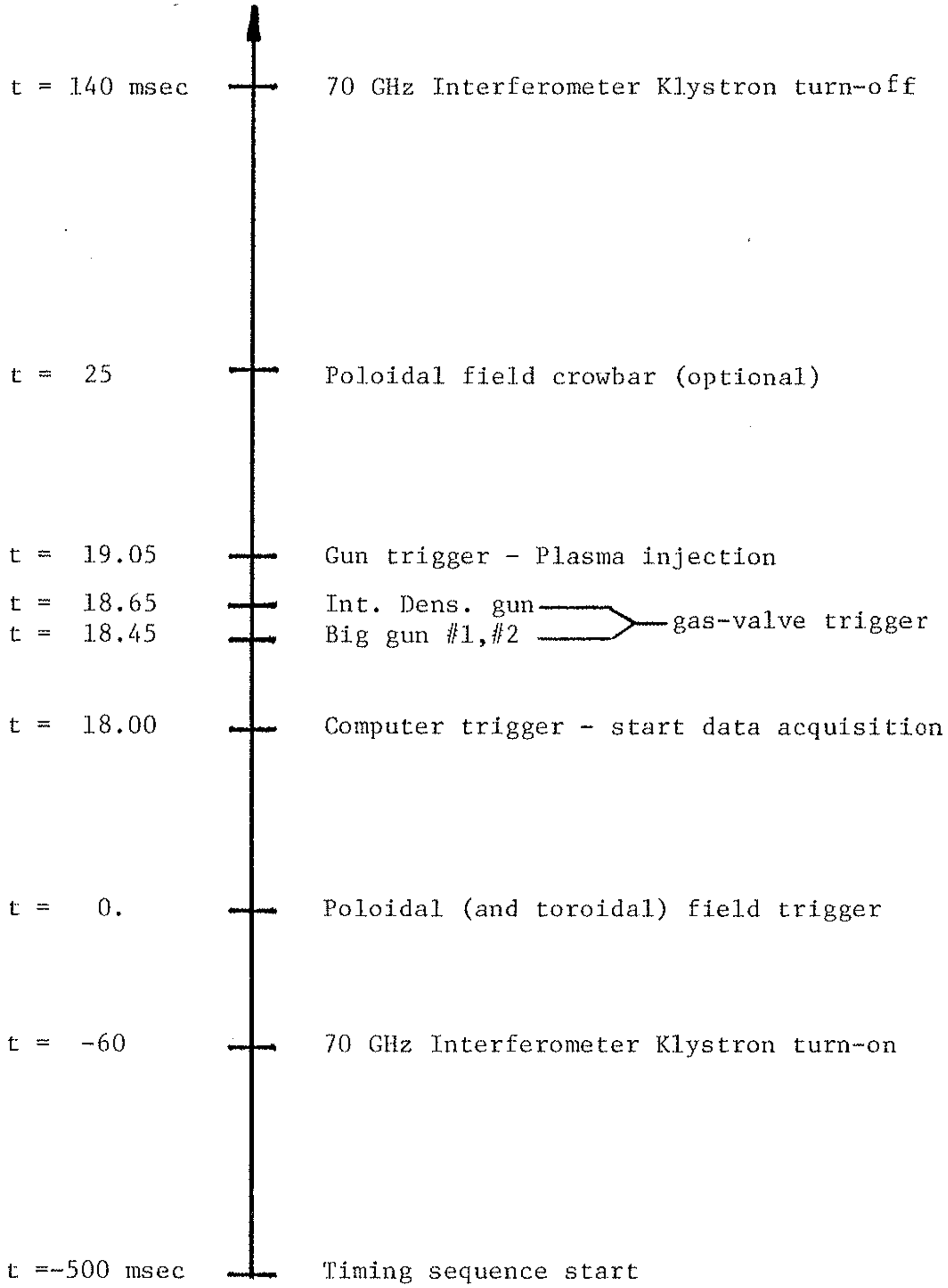
t = 140 msec
70 GHz Interferometer Klystron turn-off
t = 25
Poloidal field crowbar (optional)
t = 19.05
Gun trigger - Plasma injection
t = 18.65
Int. Dens. gun
t = 18.45
Big gun #1,#2
gas-valve trigger
t = 18.00
Computer trigger - start data acquisition
t = 0.
Poloidal (and toroidal) field trigger
t = -60
70 GHz Interferometer Klystron turn-on
t =-500 msec
Timing sequence start

References for Chapter 2

1. J.R. Drake, University of Wisconsin Plasma Physics Report PLP 537 (1973).
2. J. Marshall, Phys. Fluids 3, 134 (1960).
3. A. Kellman, University of Wisconsin PLP 859 (1981).
4. L.C. Buckhardt and R.H. Lovberg, Phys. Fluids 5, 341 (1962).
5. F.F. Chen, "Electric Probes" in Plasma Diagnostic Techniques, R.H. Huddlestone and S.L. Leonard, Eds., (Academic Press, New York, 1965), Ch. 4.
6. J.C. Sprott, University of Wisconsin PLP 88 (1966).
7. J.C. Sprott, Rev. of Sci. Inst. 39, 1569 (1968).
8. P. Nonn private communication.
9. C.M. Fortgang, University of Wisconsin-Madison, Ph.D. Thesis (1983).
10. H. Garner, University of Wisconsin PLP 833 (1980).
11. C.M. Fortgang, University of Wisconsin PLP 861 (1981).
12. W.L. Wiese, "Line Broadening" in Plasma Diagnostic Techniques, R.H. Huddlestone and S.L. Leonard, Eds., (Academic Press, New York, 1965), Ch. 6.
13. R.N. Dexter private communication.
14. R.K. Otnes and Loren Enochson, Digital Time Series Analysis, (J. Wiley and Sons, New York, 1972).
15. E.O. Brigham, The Fast Fourier Transform, (Prentice Hall Inc., N.J., 1974).
16. E.A. Rose, University of Wisconsin-Madison, Ph.D. Thesis (1982) Ch. 4.

CHAPTER 3

Summary of Ballooning Mode Theory for Multipoles

This chapter contains a brief summary of ballooning mode stability theory. A physical description of a ballooning mode in general geometry is presented with a discussion of factors that can affect ballooning stability such as plasma shape, shear, and resistivity. This is followed by an analytic solution to the low, but finite-β equilibrium in the bridge region in the Octupole. Finally, the theoretical treatment of ballooning stability in a multipole is presented including infinite and finite toroidal mode number MHD theory and a more detailed kinetic treatment of the mode including the effect of finite ion gyroradius. It is shown that for infinite toroidal mode number, the critical beta for ballooning is 4.3%, and this increases with decreasing toroidal mode number. The kinetic treatment reveals that large ion gyroradius can be strongly stabilizing. All solutions are solved numerically for Octupole geometry. The ballooning mode stability theory and numerical solution for the Octupole presented here were obtained by Phillips[1].

3.A. Physical Picture

To aid in interpretation of the experiment it is useful to precede the theoretical analysis with a discussion of the physical mechanism of the ballooning instability, including the source of free energy, the force that drives the mode unstable, and the role of curvature.

The first thing to note is that the mode grows through a decrease in magnetic energy, rather than internal energy. This is evident from inspection of the change in the energy due to displacement $\underline{\xi}$ as written in the MHD energy principle[2]

$$\delta W = \frac{1}{2} \int d\tau \left(|\underline{\tilde{B}}|^2 + (\underline{j}_o \cdot \underline{\xi} \times \underline{\tilde{B}}) + (\underline{\xi} \cdot \nabla p)(\nabla \cdot \underline{\xi}) + \gamma p (\nabla \cdot \underline{\xi})^2 \right) \quad (1)$$

where $\underline{\tilde{B}}$ is the magnetic perturbation and $\underline{j}_o$ is the equilibrium diamagnetic current (ohmic currents are ignored). The first two terms represent changes in magnetic energy, and the last two terms represent changes in internal energy $p/(\gamma-1)$. It will be shown in the next section that at marginal stability the most unstable mode is incompressible or $\nabla \cdot \underline{\xi} = 0$. Thus, the last two terms in δW are zero, and only the magnetic energy changes in the most unstable mode.

The second point of interest is that the force that drives the mode is a Lorentz $\underline{j}_o \times \underline{\tilde{B}}$ force due to the diamagnetic current. This force is included in the second term, the only destabilizing contribution to the energy integral. Instability occurs if the diamagnetic current $\underline{j}_o$ is sufficiently large so as to overcome the stabilizing effect of the first term which is positive definite. Thus, from the point of view of the instability dynamics, the pressure or plasma beta is a critical parameter only in that it produces a diamagnetic current and a destabilizing Lorentz force. This magnetic energy source is the same as that which drives the Suydam or Mercier interchange modes which are also incompressible. Thus, the ballooning mode can be viewed as a localized interchange. However, the interchange mode that is often heuristically derived[3] and results from compressional change in plasma internal energy is unrelated to the ballooning modes since it has a different energy source.

The details of the instability are clarified through Fig. 1 which displays a cylindrical region of plasma in a bad curvature field, with equilibrium field $\underline{B}_o = B_o\hat{\theta}$, field gradient $-|\nabla B|\hat{r}$, pressure gradient $-|\nabla P|\hat{r}$, and equilibrium diamagnetic current $\underline{j}_o = (|\nabla P|/B_o)\hat{z}$. To examine the radial force balance we note that a radial displacement will create a poloidal field perturbation given (by expanding $\tilde{\underline{B}} = \nabla\times(\xi\times\underline{B}_o)$) by

$$\tilde{B}_\theta = - B_o\left[\frac{\partial\xi_r}{\partial r} + \frac{\partial\xi_z}{\partial z}\right] - \xi_r \frac{\partial B_o}{\partial r} \qquad (2)$$

Thus, for example, if $\frac{\partial\xi_r}{\partial r} + \frac{\partial\xi_z}{\partial z}$ is sufficiently positive the poloidal flux will be rarefied, the field weakened or $\tilde{B}_\theta < 0$, as shown in Fig. 1. The resultant $\underline{j}_o \times \tilde{\underline{B}}_\theta$ radial force is radially outward and enhances the original perturbation with instability ensuing.

FIG. 1. Physical picture of ballooning instability indicating equilibrium quantities $\underline{B}_o$, $\underline{j}_o$, ∇B_o, ∇p_o, and perturbed quantities $\underline{\xi}$ (displacement), $\underline{\tilde{B}}$ and $\underline{j}_o \times \underline{\tilde{B}}$ (force). The z-axis is out of the paper. Plasma is shown in a field with bad curvature.

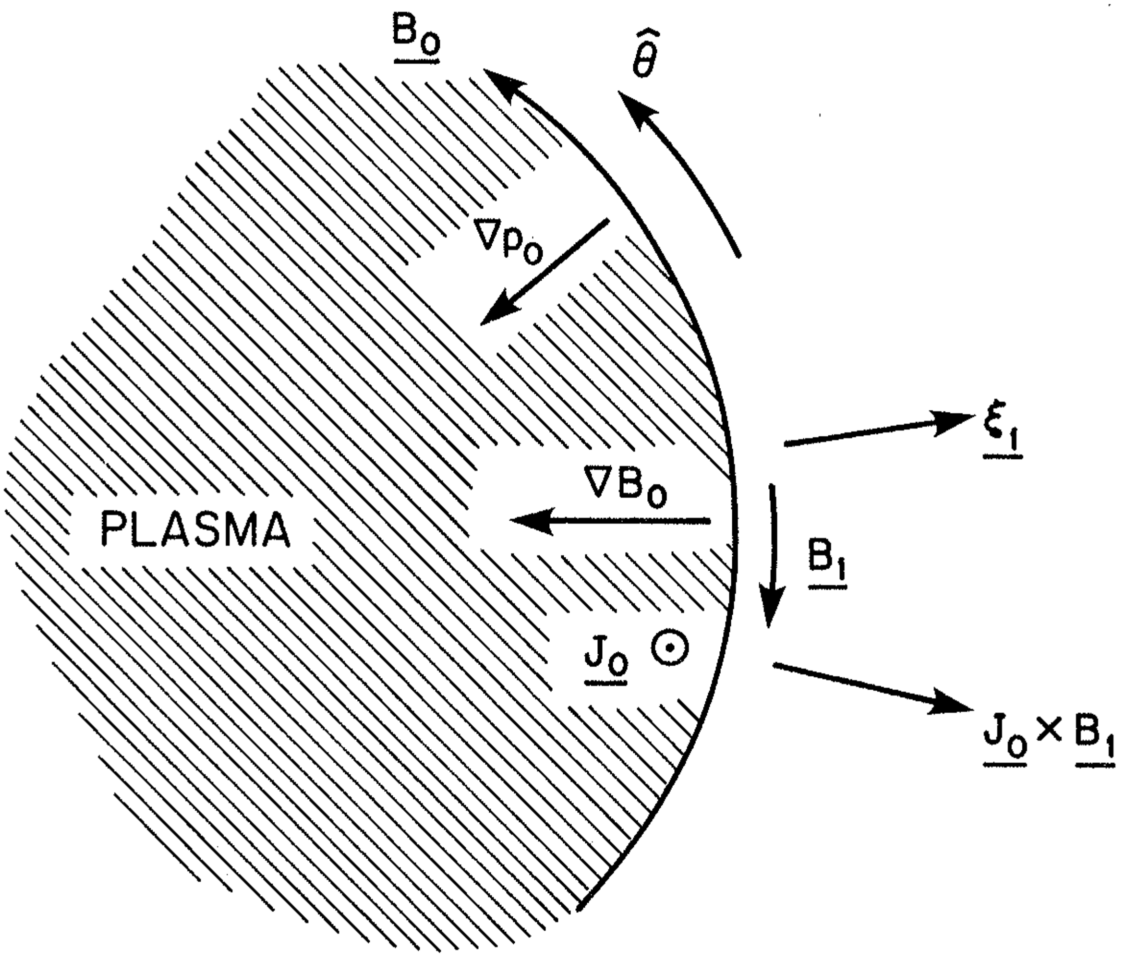
$\underline{B_0}$
$\hat{\theta}$
∇p_0
$\underline{\xi_1}$
∇B_0
PLASMA
$\underline{B_1}$
$\underline{J_0}$ ⊙
$\underline{J_0} \times \underline{B_1}$

The role of curvature is somewhat subtle. Interestingly, in a good curvature region both the destabilizing and stabilizing forces are enhanced. Curvature enters explicitly in the $\partial B_o/\partial r$ term in Eq. (2). This term is destabilizing in good curvature $(\partial B_o/\partial r>0)$ regions only. Thus the contribution of this term in the good curvature region makes $\tilde{B}_\theta$ more negative (the direction required for instability) but also enchances its magnitude $|\tilde{B}_\theta|$. The increase in $|\tilde{B}_\theta|$ enhances the quadratic stabilizing term, $|\tilde{B}|^2$, of δW, more than the destabilizing $\underline{j}_o \times \underline{\tilde{B}}_\theta$ which is only linear in $\tilde{B}_\theta$. Thus the added stabilizing field compression in good curvature favors mode localization to bad curvature regions.

3.B. Factors Affecting Ballooning Stability

There are many factors that can affect the actual value of the β-limit for the ideal ballooning instability; in particular the magnetic geometry and detailed kinetic properties of the plasma. Furth, et al[4] showed that minimizing the connection length between the good and bad curvature regions increases the β-limit. This principle has been applied to tokamaks and in a recent paper by Bernard and Moore[5], it was shown that elongation of the discharge and addition of triangularity on the outside edge decreases the connection length between good and bad curvature and thus increases the β-limit. By optimization of the discharge shape the calculated maximum stable volume averaged beta was increased to 10.2% from a typical value of 3%.

Dagazian and Paris[6] have shown that high magnetic shear can also be very stabilizing. In a Reversed Field Pinch device, which has bad curvature throughout, high shear can provide stability to ideal ballooning modes up to high values of beta (~20-30%). Tang, Connor and Hastie[7] showed for general geometry that the inclusion of finite ion gyroradius increased the β-limit from the ideal MHD value by an amount proportional to $(\rho_i/L_n)(\rho_i/\lambda_\perp)$ where ρ_i, L_n, and $\lambda_\perp$ are the ion gyroradius, density scale length, and perpendicular wavelength respectively. Connor, Chen and Chance[8] examined the effect of resistivity and ion perpendicular viscosity on the stable region between the ideal MHD limit and the higher limit due to finite gyroradius effects. They found that resistivity can destabilize the mode in this region but that ion viscosity reduces the growth rates. Dagazian and Paris[9] showed that perpendicular ion viscosity always reduces the growth rate of electrostatic ballooning modes; however, they point out that these results do not necessarily apply to the ideal ballooning mode since it is electromagnetic and the plasma dynamics along a field line are also different for the two modes.

In the following sections we treat the effects of finite toroidal wavelength, particle trapping, and finite ion gyroradius and apply the results to the Octupole geometry. A more heuristic treatment of the effect of ion gyroviscosity is presented in Chapter 5.

3.C. MHD Equilibrium Theory - Finite - β

For all stability calculations presented in this paper the MHD equilibrium of the Levitated Octupole was treated by numerically solving the Grad-Shafranov equation for a given pressure profile, with the requirement that both the pressure and pressure gradient must go to zero at the critical flux surface, at the plasma edge, which possesses neutral average curvature. The field lines and pressure profile are mapped out in flux coordinates for subsequent use in the stability calculations.

The equilibrium equation can be solved analytically, however, in the bridge region for the perturbation to the vacuum magnetic field due to the finite-β plasma. As stated in the introduction, the standard orthogonal flux coordinate system (ψ, χ, ϕ) will be used. The starting point for the derivation is the MHD force balance equation,

$$\vec{j} \times \vec{B} = \nabla p \tag{3}$$

where j is the diamagnetic current (there are no other currents in the plasma), B is the total magnetic field and p is the pressure. Solving for the diamagnetic current, we find

$$\vec{j} = - \frac{R\partial p}{\partial\psi} \hat{\phi} \quad . \tag{4}$$

Substituting $\vec{j}$ into Ampere's law, $\vec{j} = \nabla \times \vec{B}$, the ϕ component becomes,

$$\frac{1}{J} \frac{\partial}{\partial \psi} (JB\Delta B) = -\mu_o \frac{\partial p}{\partial \psi} \tag{5}$$

where J is the Jacobian, ΔB is the perturbation to the vacuum magnetic field, B_v, due to the diamagnetic current, and $B=B_v+\Delta B$. With the assumption that $\Delta B/B_v \ll 1$ and $\frac{\partial \Delta B}{\partial \psi} \ll \frac{\partial B_v}{\partial \psi}$, and using $J \sim B^{-2}$, Eq. (5) reduces to

$$B_v^2 \frac{\partial}{\partial \psi} \left(\frac{\Delta B}{B_v}\right) = -\mu_o \frac{\partial p}{\partial \psi} \tag{6}$$

which can easily be solved for ΔB,

$$\frac{\Delta B(\psi)}{B_v(\psi)} = -\mu_o \int_{\psi_o}^{\psi} \frac{1}{B_v{}^2} \frac{\partial p}{\partial \psi} d\psi + K \quad . \tag{7}$$

If ψ_o is chosen as the surface of the ring, then K is related to the field perturbation at the surface. The constant, K, can be determined by requiring that there is no net change in flux between the ring and the wall. This is a good assumption because of the fast time scales in this experiment and the high conductivity aluminum ring and wall. This requirement reduces to

$$\int_{\text{ring}}^{\text{wall}} R\Delta B dr = 0 \quad . \qquad (8)$$

With this condition, the full solution for ΔB can be found. This solution, however, is only valid in the bridge region since the assumption on the relative size of ΔB and B_v is clearly invalid in the center of the machine where B_v is low everywhere and is actually zero at three locations.

As an example, consider a gaussian pressure profile peaked on the separatrix of the form, $p=p_o \exp[-(r-r_s)^2/2r_o^2]$, where r_s is the radial distance of the separatrix from the center of the ring and $r_o=(a-r_s)/3$, where a is the minor radius of the internal ring. If the magnetic field is assumed to have a 1/r dependence, Eq. (7) can be integrated analytically to obtain an expression for $\Delta B(r)$ involving error functions. The quantity $\Delta B(r)/B_{sep}$, where B_{sep} is the vacuum field on the separatrix, is plotted in Fig. 2. For this choice of profile shape, the constant K is very small and has not been added to the solution shown, but is plotted separately as the dotted line in Fig. 2. It can be seen that the agreement between this analytic solution and the full numerical solution to the Grad-Shafranov equation (also shown in Fig. 2) is very good.

An interesting property relating ΔB and β can now be derived. Consider a pressure profile with a peak value on the separatrix equal to p_s. Thus, the pressure can be written as

$$p(\psi) = p_s \hat{p}(\psi) \qquad (9)$$

FIG. 2. Analytic solution for plasma diamagnetic perturbation to the vacuum magnetic field (solid line). The small correction due to the change in the ring current is shown as the dotted line. The full numerical solution to the Grad-Shafranov equation for a $\beta=2.5\%$ plasma is shown for comparison.

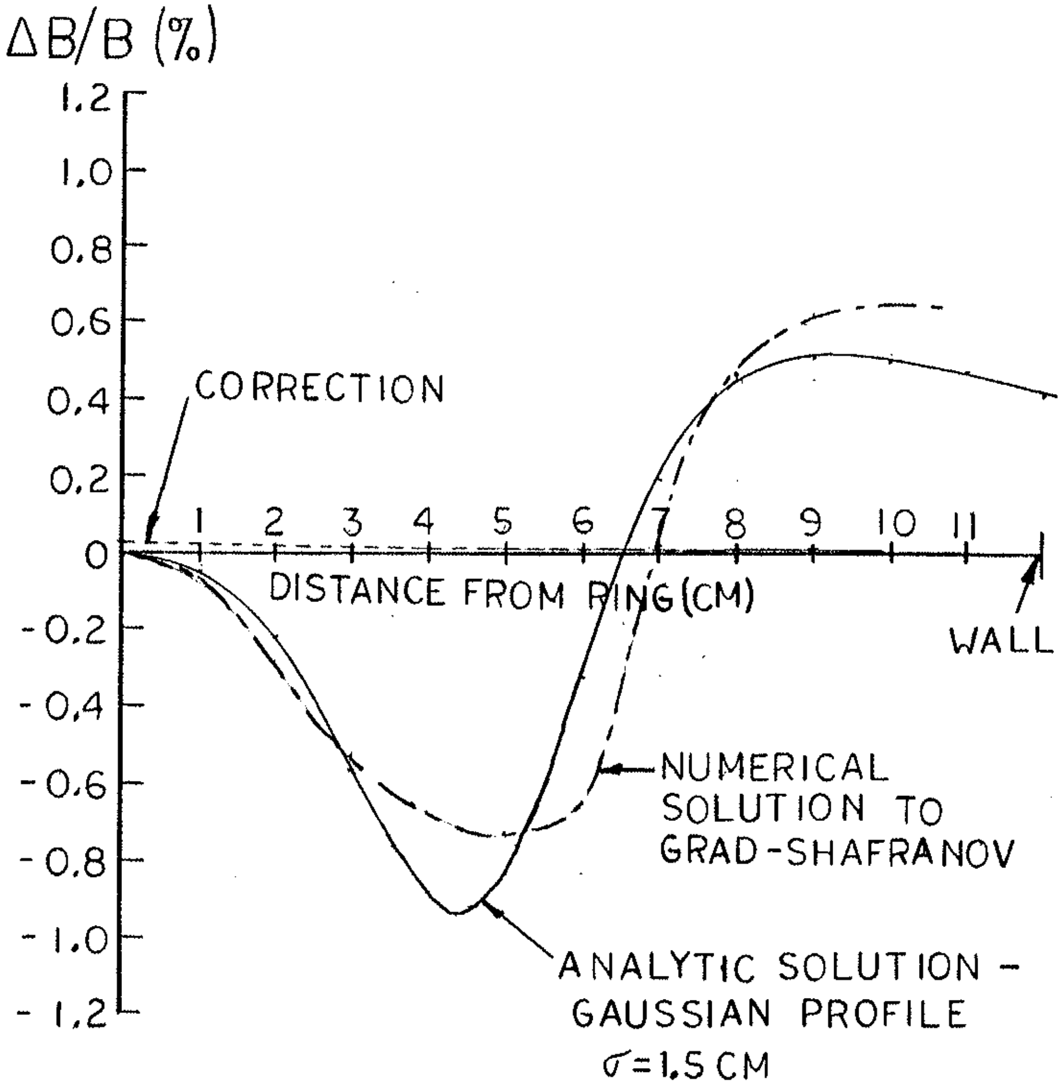
ΔB/B (%)
1.2
1.0
0.8
0.6
0.4
0.2
0
-0.2
-0.4
-0.6
-0.8
-1.0
-1.2
1
2
3
4
5
6
7
8
9
10
11
CORRECTION
DISTANCE FROM RING (CM)
WALL
NUMERICAL SOLUTION TO GRAD-SHAFRANOV
ANALYTIC SOLUTION - GAUSSIAN PROFILE
σ=1.5 CM

where $\hat{p}(\psi)$ is the normalized pressure profile with a maximum value of unity. Upon substitution of Eq. (9) into Eq. (7) and solving for the constant, K, the solution can be expressed as

$$\left(\frac{\Delta B}{B_v \beta_s}\right) = -g(\psi) + h \qquad (10)$$

where

$$g(\psi) = + \frac{1}{2} \int_{\psi_o}^{\psi} \left[\frac{\partial \hat{p}}{\partial \psi} / \left(B_v^2(\psi)/B_s^2\right)\right] d\psi \quad ,$$

$$h = \frac{\frac{1}{2}\int_{ring}^{wall} B_v(r) R(r) g(r)\, dr}{\int_{ring}^{wall} B_v(r) R(r)\, dr} \quad ,$$

and the subscript ´s´ refers to separatrix quantities. Equation (10) is an important result because the entire right-hand side depends only on the shape of the vacuum field and the pressure profile but not on the magnitude of either. Thus, for a given profile shape, the quantity $\Delta B/B\beta$ does not depend on the value of magnetic field or β, i.e. the fractional change in B is proportional to β.

3.D. MHD Stability Theory--Infinite Toroidal mode Number

The equation for the MHD stability of an axisymmetric system with no shear was one of the first applications of the MHD energy principle[2,10-12]. The multipole has no shear, and the modes can be Fourier analyzed in the toroidal, ϕ, direction. One finds that the mode with infinite toroidal mode number, $n=\infty$, is the most unstable mode[2] since at $n=\infty$ the stabilizing magnetic perturbation $\tilde{B}_\phi$ $(\sim\xi_\phi)$ due to field line bending (first term Eq. (1)) is minimized relative to the destabilizing $\tilde{B}_\chi(\sim n\xi_\phi)$, second term Eq. (1). In this case, $n=\infty$, the modes are localized on a flux surface, and the question of stability is reduced to solving a second order ordinary differential equation on each field line. For marginal stability, $\omega^2=0$, the critical pressure gradient for the most unstable mode is given by the eigenvalues, p_c', of the equation

$$\frac{\partial}{\partial\chi}\left(\frac{1}{Jr^2B^2}\frac{\partial X}{\partial\chi}\right) - J\mu_o p_c' DX = J\mu_o Df \ . \qquad (11)$$

which is obtained in ref.(1) by minimizing δW with respect to Y, Z, and X respectively, where $p'\equiv\partial p/\partial\phi$, $D=\frac{1}{J}\frac{\partial J}{\partial\phi} - \frac{\mu_o p'}{B^2}$ is related to the covariant component of the curvature, K_ϕ, by $D=-2K_\phi$, $Y\equiv -in\xi_\phi/R$, $Z\equiv\xi_\chi/B$, $X\equiv RB\xi_\phi$ is the covariant component of the displacement ξ_ϕ, J is the Jacobian and $f(\phi)=\oint JDXd\chi/\left[\mu_o\oint d\chi\frac{J}{B^2} + \frac{1}{\gamma p}\oint d\chi J\right]$. The field lines are closed in the multipole so X in Eq. (11) must be both periodic and continuous along the field line. Integrating Eq. (11) around a closed field line and using the periodicity condition yields $f(\psi)=0$. It can be shown that $f(\psi)=\gamma p\nabla\cdot\underline{\xi}$; thus at marginal stability, the most unstable mode is incompressible. In an up-down symmetric multipole, modes are either symmetric or antisymmetric with respect to reflection about the midplane. Modes with even symmetry have $\frac{\partial X}{\partial \chi}=0$ on the midplane, and modes with odd symmetry have $X=0$ on the midplane. The equilibrium pressure gradient is plotted in Fig. 3 along with the critical pressure gradient for both even and odd modes. The plasma is marginally stable when the equilibrium pressure gradient is equal to but not greater than the critical pressure gradient at one or more points. In the Levitated Octupole this occurs at $\beta=4.3\%$, where β is defined as the local beta on the separatrix between the outside ring and outside wall. Outside the separatrix the mode with even symmetry is the most unstable since it bends the field lines the least. At the separatrix the modes with even and odd symmetry are degenerate, and the boundary conditions $X=0$ and $\partial X/\partial\chi=0$ on the midplane are satisfied simultaneously. This minimizes the effect of the inverse curvature going to infinity at the field null. Near the critical flux surface X is interchange-like. On flux surfaces closer to the separatrix the magnitude of X maximizes in the bad curvature region, characteristic of a ballooning mode.

FIG. 3. MHD critical pressure gradient for even and odd modes and equilibrium pressure gradient for β=4.33%, ϕ_{sep}=0.5318, ϕ_{crit}=0.8245.

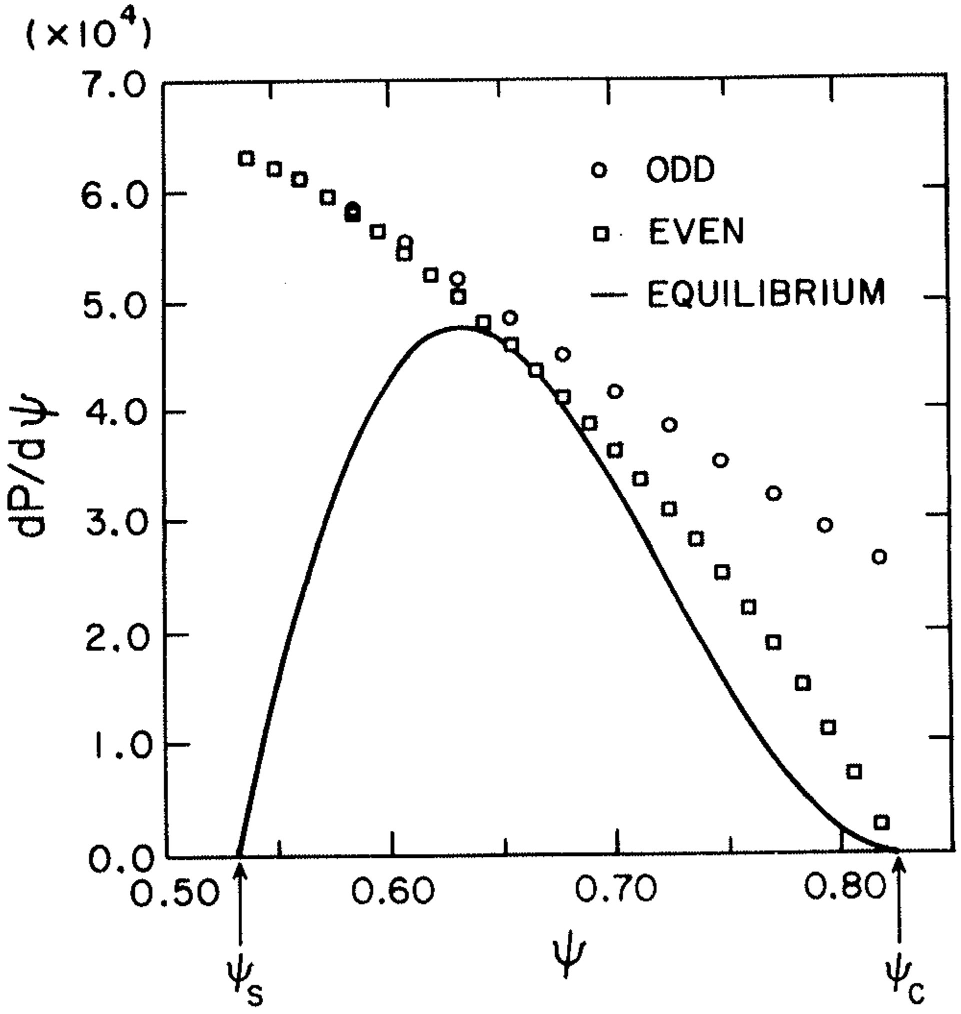
(×10^4)
7.0
6.0
5.0
4.0
3.0
2.0
1.0
0.0
dP/dψ
0.50
0.60
0.70
0.80
ψ
ψ_S
ψ_C
○ ODD
□ EVEN
— EQUILIBRIUM

6.E. MHD Stability Theory--Finite Toroidal Mode Number

Since beta values well above the MHD critical beta of 4.3% have been observed experimentally, MHD has proved inadequate for predicting the beta limit attainable by the Octupole experiments. Before discarding MHD theory completely it is useful to consider modes with finite n, i.e. $n<\infty$. It is well known that some low frequency modes ($\omega/\omega_{ci} \ll 1$) with short perpendicular wavelengths ($\lambda \lesssim \rho_i$) are stabilized by finite Larmor radius (FLR) effects^{13}. Thus, the actual beta limit may be set by lower n number modes. An equation for high, but finite, toroidal mode number MHD is obtained by minimizing $\delta W/\delta K_\perp$ with respect to Y, Z and X in that order and using a perturbation expansion in orders of $1/n^2$ for the minimizing Y. Here δW is the MHD energy integral for displacement $\underline{\xi}$, $\delta K_\perp$ is perturbed perpendicular kinetic energy and Y, Z, and X are the covariant components of ξ_ϕ, ξ_χ, and ξ_ψ as defined in the previous section. This yields the partial differential equation, with the finite n terms on the right-hand side,

$$\frac{\partial}{\partial\chi}\left[\frac{1}{Jr^2B^2}\,\frac{\partial X}{\partial\chi}\right] - J\mu_o p' X + \mu_o\rho_m\omega^2\frac{JX}{r^2B^2}$$

$$= \frac{1}{n^2}\left\{\frac{\partial}{\partial\phi}\,\frac{\partial}{\partial\chi}\left[\frac{r^2}{J}\,\frac{\partial}{\partial\chi}\left(\frac{\partial X}{\partial\phi} + \frac{\mu_o p'}{B^2}X\right)\right] - \frac{\mu_o p'}{B^2}\left[\frac{r^2}{\partial}\,\frac{\partial}{\partial\chi}\left(\frac{\partial X}{\partial\phi} + \frac{\mu_o p'}{B^2}X\right)\right]\right.$$

$$\left. + \frac{\partial}{\partial\phi}\left[Jr^2\left(\frac{\partial X}{\partial\phi} + \frac{\mu_o p'}{B^2}X\right)\right] + \frac{\mu_o p'}{B^2}\,Jr^2\left(\frac{\partial X}{\partial\phi} + \frac{\mu_o p'}{B^2}X\right)\right\} \qquad (12)$$

where ρ_m is the mass density, n is the toroidal mode number and ω^2 is the frequency of the mode. The modes were assumed incompressible. As in the $n=\infty$ theory, we will treat the marginally stable $\omega^2=0$ case, so that either p' or n can be specified with the other solved for as the eigenvalue of the equation. For any p' (for $\beta>4.3\%$) there will be a corresponding n above which the plasma is unstable; equivalently, for given n, or toroidal wavelength, there is a critical p' or β above which the plasma is unstable.

Phillips[1] developed a method for solving Eq. (12) based on a perturbation expansion about the $n=\infty$ solution. An alternate solution method was used by Adler and Lee[14] for solving Eq. (12). They adopted the procedure used in Spies[15] of expanding the solution in terms of a complete set of eigenfunctions along a field line. The equation for the high n stability then becomes an infinite set of coupled differential equations in the variable ϕ. Generally only the lowest order equation is kept. The method we use is more similar to a straightforward perturbation expansion. Using a perturbation expansion it is easier to obtain an explicit solution to the problem including the ϕ dependence of the mode. A perturbation expansion about the $n=\infty$ solution yields to lowest order a solution of the form $X_o(\phi,\chi)=U_o(\phi,\chi)R_o(\phi)$ and reduces the problem to solving two ordinary differential equations. The zero order ($n=\infty$) equation which determines the structure of the mode along field lines is

$$\frac{\partial}{\partial\chi}\left(\frac{1}{Jr^2B^2}\frac{\partial U_o}{\partial\chi}\right) - J\mu_o p_o' DU_o = 0 \tag{13}$$

where p_o' is the critical pressure gradient for the $n=\infty$ mode. This equation yields the parallel (χ) dependence of U_o. Since the parallel structure is different on each magnetic surface, U_o is also a function of ϕ. For marginal stability the equation for the radial envelope $R_o(\phi)$ is

$$\begin{aligned}
&\frac{d}{d\phi}\{\oint \frac{\partial U_o}{d\chi}\frac{r^2}{J}\frac{\partial U_o}{\partial\chi}\,d\chi\,\frac{dR_o(\phi)}{d\phi}\} \\
&\quad + \{\frac{d}{d\phi}[\oint \frac{\partial U_o}{\partial\chi}\frac{r^2}{J}\frac{\partial U_o}{\partial\chi}\,d\chi] - \oint \frac{r^2}{J}[\frac{\partial^2}{\partial\phi\partial\chi}U_o]^2 d\chi\}R_o(\phi) \\
&\quad = n^2\{\mu_o(p'-p_o')\oint JDU_o^2 d\chi\}R_o(\phi)
\end{aligned} \tag{14}$$

where we assumed low beta. The solution for U_o from Eq. (13) is used as input to Eq. (14). The boundary conditions for $R_o(\phi)$ are that R_o go to zero on conducting surfaces. In addition, we take R_o to be zero on the edge of the plasma to treat the ballooning instability, an internal mode, and to eliminate the interchange mode which is always marginally stable at the critical flux surface.

For beta slightly above the n=∞ critical beta the radial (ψ) extent of the mode is limited, and a good approximation to the lowest marginally stable mode number, n, is obtained by WKB analysis. Ignoring terms involving $\frac{\partial U_o}{\partial \psi}$ (approximate for a radially local mode where U_o varies slowly in the radial direction relative to R_o) Eq. (14) reduces to

$$\frac{d^2 R_o(\psi)}{d\psi^2} + n^2 Q(\psi, p')R_o(\psi) = 0 \qquad (15)$$

where

$$Q(\psi, p') = \frac{\mu_o(p_o' - p')\oint JDU_o^2 d\chi}{\oint \frac{r^2}{J}\left(\frac{\partial U_o}{\partial \chi}\right)^2 d\chi} \; .$$

The eigenvalue p_o' is the critical pressure gradient from Eq. (13), and p' is the equilibrium pressure gradient. Using the WKB turning point formula yields an expression for the critical mode number n_c,

$$n_c = \frac{\pi}{2\int_{\psi_a}^{\psi_b} Q^{1/2}(\psi,p')d\chi} \quad . \tag{16}$$

Here ψ_a and ψ_b are the turning points where $Q=0$ (or $p'=p_o'$) with $|p'|>|p_o'|$ for $\psi_a<\psi<\psi_b$. Modes with $n>n_c$ are unstable, and modes with $n<n_c$ are stable.

For equilibrium beta significantly greater than the $n=\infty$ critical beta, the ψ extent of the mode is radially nonlocal, Eq. (16) is inaccurate and Eq. (13) and Eq. (14) are solved numerically. For this purpose, we again take $R_o(\psi)$ to be zero at the outer edge of the plasma as one boundary condition. Inside the separatrix, in the absolute good curvature region, the critical pressure gradient jumps by a factor greater than ten. The mode amplitude is therefore expected to decrease rapidly inside the separatrix; thus we take $R_o(\psi)$ to be zero at the separatrix as the other boundary condition. The numerical results for the Levitated Octupole configuration are shown in Fig. 4 where β versus $1/n_c$ (or toroidal wavelength) is plotted. The beta limit is roughly inversely proportional to $1/n_c$. Hence if n were limited by some means such as finite ion gyroradius, one would expect an increase in the beta limit of the device. However, if as an exercise one merely sets the toroidal wavelength equal to the thermal ion gyroradius, corresponding to $n_c \simeq 500$, the beta limit is only negligibly enhanced and cannot model the experimental results. The full strength of

FIG. 4. Critical β for instability versus $1/n_c$. $1/n_c$ = (toroidal wavelength/ toroidal circumference). For a given β, modes with $n>n_c$ are unstable and modes with $n<n_c$ are stable.

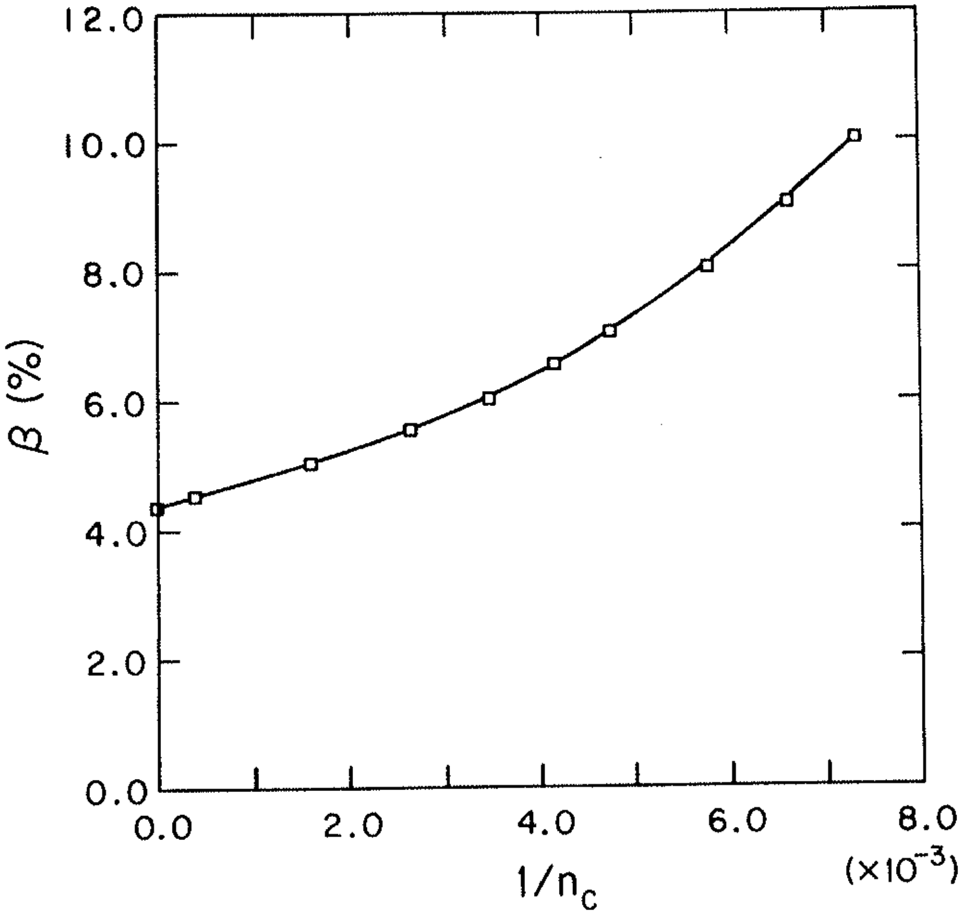
12.0
10.0
8.0
6.0
4.0
2.0
0.0
β (%)
0.0
2.0
4.0
6.0
8.0
(×10⁻³)
1/n_c

finite ion gyroradius stabilization is included in the next section through a proper kinetic treatment. Nevertheless, the fully reconstructed eigenfunction $X_o(\psi,\chi)=U_o(\psi,\chi)R_o(\psi)$ is calculable and is shown in Fig. 5 for $\beta=4.5\%$ and $\beta=5.0\%$. The width of the mode is proportional to $1/\sqrt{n_c}$. For beta values slightly greater than the $n=\infty$ critical beta the modes take up the whole region between the separatrix and the critical flux surface. As n_c becomes larger the radial extent of the mode becomes narrower until at $n=\infty$ the radial part of the eigenfunction is a delta function in ψ.

6.F. Kinetic Theory

The influence of kinetic effects, such as finite ion gyroradius, on ballooning modes, is treated in detail through the linearized Vlasov equation. A general set of kinetic equations for low frequency modes in multipoles can be derived by small frequency ($\omega \ll \omega_{ci}$, the ion cyclotron frequency), small gyroradius ($\rho_i \ll L_p, L_B$, the pressure and magnetic gradient scale lengths) expansions in order to obtain the perturbed distribution function[16]. Moments of the perturbed distribution function are calculated and used in the quasi-neutrality condition and force balance equations to obtain a complete set of equations governing the modes[1]. Considering an additional low frequency constraint $\omega \ll \omega_{bi}$, $\omega \ll \omega_{be}$, where ω_b is the bounce frequency, and expanding in powers of $1/n^2$, the equations, written to first order in ion gyroradius, can after much effort be

FIG. 5. X_o eigenfunction for the marginally stable mode for (a) β=4.5%, n=2525 and (b) β=5.0%, n=621. The mode fills up all the available flux space between ψ_{sep} and ψ_{crit} for only small increases above the ideal MHD limit of β=4.33%, where ψ_{sep} and ψ_{crit} are the locations of the separatrix and the critical flux surface. The eigenfunction peaks in the outer bad curvature region near the flux surface with the steepest pressure gradient. The plot is shown for half the field lines since the machine is up-down symmetric.

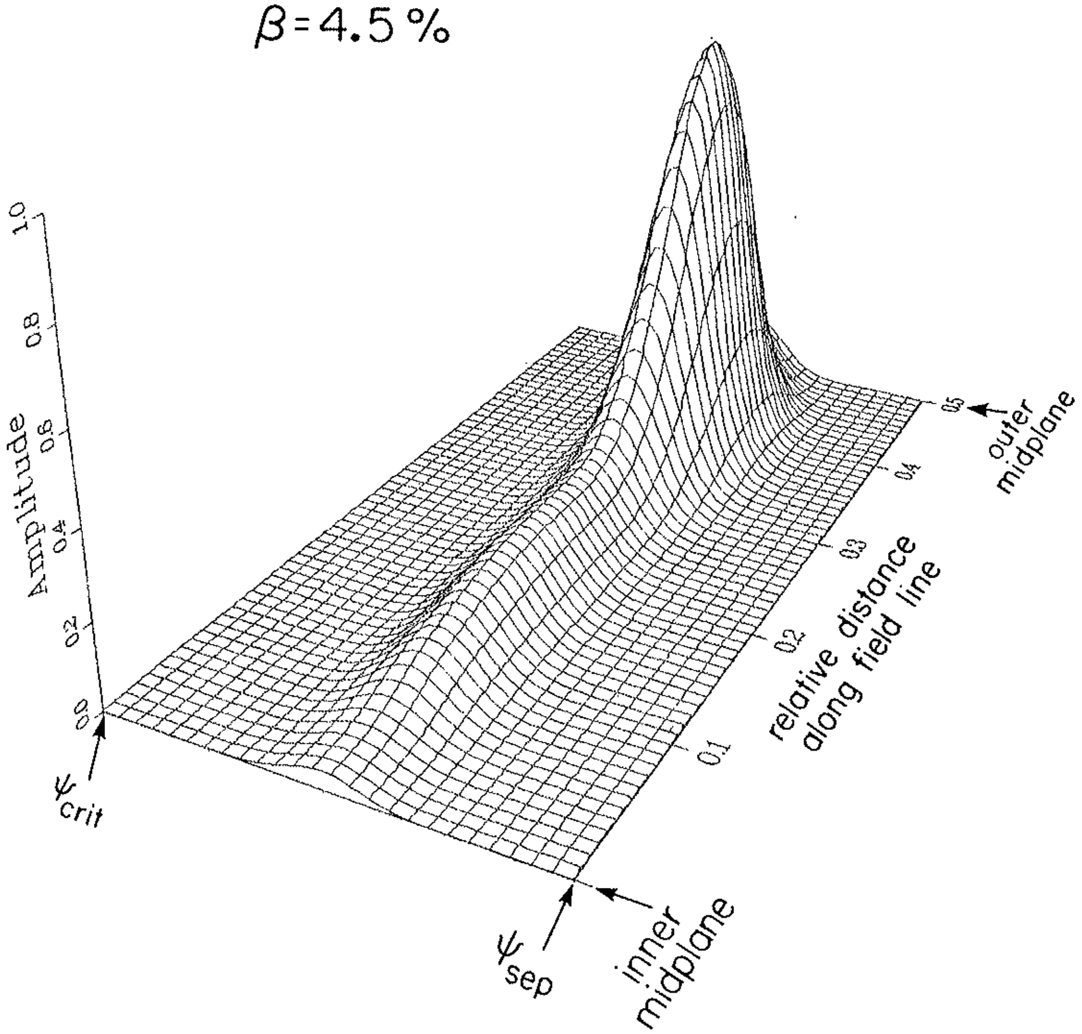
β=4.5 %
Amplitude
0.0
0.2
0.4
0.6
0.8
1.0
0.1
0.2
0.3
0.4
0.5
relative distance
along field line
outer
midplane
inner
midplane
ψ_{crit}
ψ_{sep}

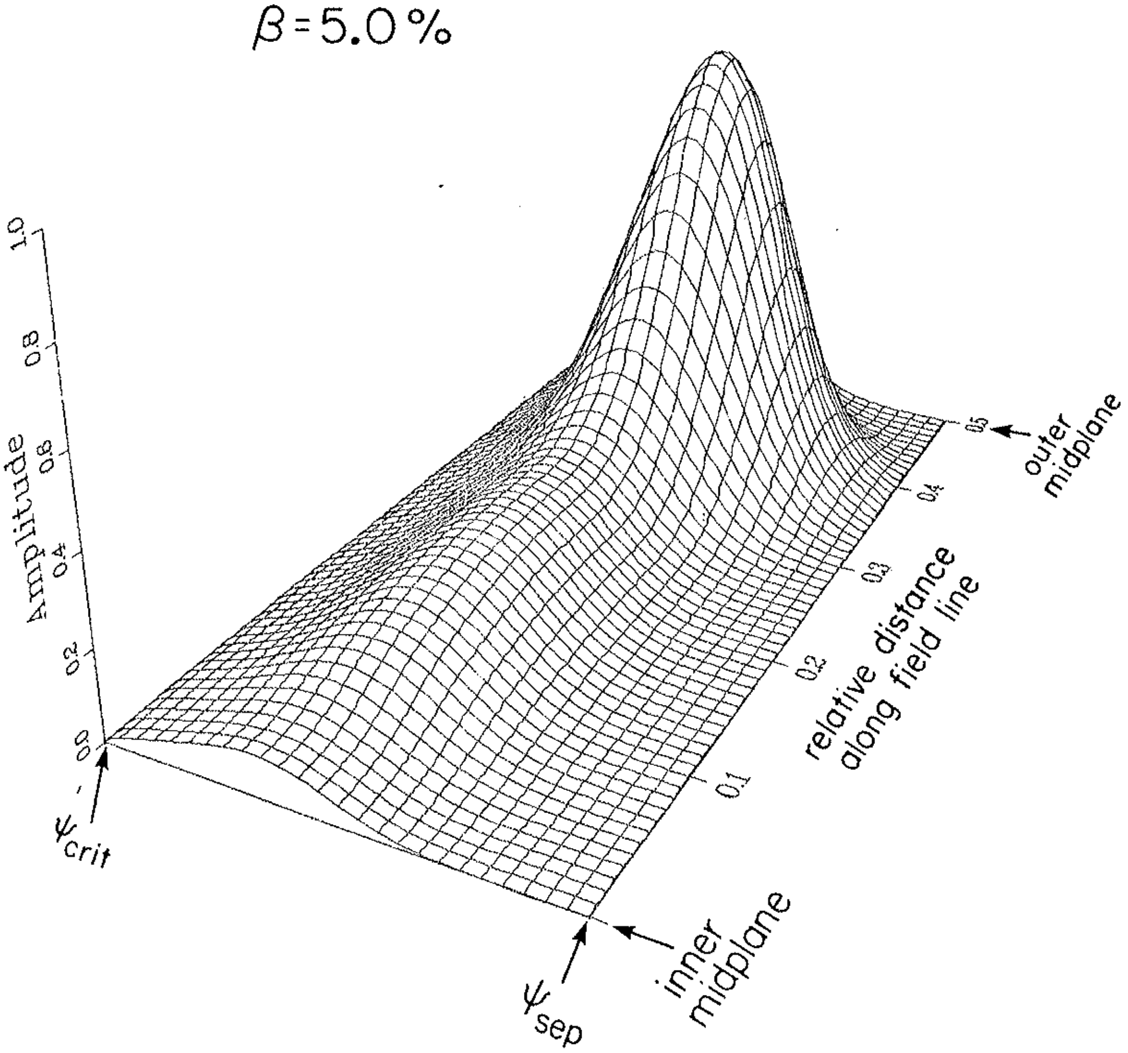
β=5.0%
Amplitude
0.0
0.2
0.4
0.6
0.8
1.0
relative distance along field line
0.1
0.2
0.3
0.4
0.5
outer midplane
inner midplane
ψ_{crit}
ψ_{sep}

combined to form a single partial differential equation for the modes

$$\frac{\partial}{\partial\chi}\left(\frac{1}{Jr^2B^2}\frac{\partial X}{\partial\chi}\right) - J\mu_o p' DX + \mu_o n_o m_i \omega(\omega-\omega_i^*)J\,\frac{X}{r^2B^2}$$

$$= \frac{1}{n^2}\left\{\frac{\partial}{\partial\phi}\frac{\partial}{\partial\chi}\left[\frac{r^2}{J}\frac{\partial}{\partial\chi}\left(\frac{\partial X}{\partial\phi} + \frac{\mu_o p'}{B^2}X\right)\right] - \frac{\mu_o p'}{B^2}\frac{\partial}{\partial\chi}\left[\frac{r^2}{J}\frac{\partial}{\partial\chi}\left(\frac{\partial X}{\partial\phi} + \frac{\mu_o p'}{B^2}X\right)\right]\right.$$

$$+ \frac{\partial}{\partial\phi}\left[\mu_o n_o m_i \omega(\omega-\omega_i^*)Jr^2\left(\frac{\partial X}{\partial\phi} + \frac{\mu_o p'}{B^2}X\right)\right]$$

$$\left. - \frac{\mu_o p'}{B^2}\,\mu_o n_o m_i \omega(\omega-\omega_i^*)Jr^2\left(\frac{\partial X}{\partial\phi} + \frac{\mu_o p'}{B^2}X\right)\right\} \quad . \qquad (17)$$

where $\omega_i^* = -\frac{nT_i}{e}\frac{p'}{p}$ is the ion diamagnetic frequency, n_o is the particle density, and m_i is the mass of the ions. In the limit $T_i \to 0$ the kinetic ballooning mode equation, Eq. (17), reduces to the MHD ballooning mode equation, Eq. (12). The effect of heat flow along field lines was neglected to arrive at Eq. (17). Calculation[1] of the beta limit using the Kruskal-Oberman energy principle which includes heat flow along field lines, but does not include FLR effects, has shown that the critical beta limit of the $n=\infty$ mode in the Levitated Octupole increases to 4.70%, compared to 4.33% for the MHD case. Since this represents a small relative correction, neglecting the effect of heat flow along field lines is justified.

It is interesting to note that if we start with the original kinetic equations and take the limit $\omega >> \omega_{bi}$, $\omega >> \omega_{be}$, to lowest order in gyroradius, we again get Eq. (17). Thus, if the effect of heat flow is small, Eq. (17) is correct in either limit of the ratio of wave to bounce frequency. This is similar to results of Lee and Catto[17] who found that the kinetic-ballooning mode equation for tandem mirrors could be generalized for arbitrary ratio of wave to bounce frequency.

As before (Section E) the lowest order solution to Eq. (17) is written as $X_o(\psi,\chi)=U_o(\psi,\chi)R_o(\psi)$. The equation for the parallel (χ) structure $U_o(\psi,\chi)$ is the same as Eq. (13). Either p_o' or ω_o', the zeroth order solutions for pressure gradient and complex frequency, can be specified with the other solved as the eigenvalue. The FLR effects are contained in the equation for the radial (ψ) structure $R_o(\psi)$ which is

$$\frac{d}{d\psi}\left[A(\psi)\frac{dR_o(\psi)}{d\psi}\right] + \left[B(\psi) + n^2C(\psi)\right]R_o(\psi) = 0 \quad (18)$$

where

$$A(\psi) = a_o - \mu_o n_o m_i \omega(\omega-\omega_i^*)a_1$$

$$B(\psi) = \frac{d}{d\psi}[a_2 - \mu_o n_o m_i \omega(\omega-\omega_i^*)a_3] - a_4 + \mu_o n_o m_i \omega(\omega-\omega_i^*)a_5$$

$$C(\psi) = -\mu_o(p'-p_o')a_6 + [\omega_o^2-\mu_o n_o m_i \omega(\omega-\omega_i^*)]a_7$$

and the coefficients a_o to a_7 are surface integrals which are given in the appendix. Equation (18) contains three unknown constants--the real oscillation frequency ω, the toroidal mode number, n, and the temperature, T_i, appearing in ω_i^*.

Two additional constraints are necessary to eliminate two of the constants with the third remaining as the eigenvalue of Eq. (18). The first constraint is obtained by multiplying Eq. (18) by $R_o(\psi)$ and integrating over ψ to obtain

$$\int_{\psi_a}^{\psi_b} \left\{A(\psi)\left(\frac{dR_o}{d\psi}\right)^2 - \left[B(\psi) + n^2(C(\psi)\right]R_0^2(\psi)\right\}d\psi = 0 \quad (19)$$

where the limits ψ_a and ψ_b are the boundaries of $R_o(\psi)$. Equation (19) is quadratic in ω. The condition of marginal stability ($\mathrm{Im}(\omega)=0$) requires the discriminant of quadratic Eq. (19) be zero or

$$\frac{T_i}{e^2}\,\frac{1}{(1+\tau)} = 4\,\frac{(n^2C_o+C_1)(n^2C_2+C_3)}{n^2(n^2C_4+C_5)^2} \qquad (20)$$

where $\tau=T_e/T_i$ and the coefficients C_o to C_5 are ψ-integrals which involve p' and R_o and are given in the appendix. Equation (20) gives a relation between T_i and n for a marginally stable mode. As shown schematically in Fig. 6, for a given β, T_i has a maximum as a function of n. For an arbitrary temperature $T_{io} < T_{max}$, shown in the figure, *all* modes with $n_1<n<n_2$ are unstable. Thus, each point on the stability boundary (β versus ρ_i plot shown later in Fig. 7) is determined by the mode with $T_i=T_{imax}$ and corresponding n_c. For temperatures $T>T_{max}$, all modes in the plasma are stabilized by FLR effects. The stability boundary to the *right* of the maximum point also represents the effect of FLR stabilization. For fixed T_i, if the boundary is crossed by increasing n, stability occurs since the gyroradius increases relative to the decreasing toroidal wavelength (~1/n). The *left* boundary represents the stabilizing effect of low n that is present in MHD (making $n=\infty$ most unstable) and discussed in Section D.

To determine the mode number, n_c, and its temperature T_{imax} at the stability boundary, we use Eq. (20) to set the derivative of T_i with respect to n^2, holding τ fixed, equal to zero. This yields a cubic equation in n^2,

$$C_oC_2C_4n^6 + (2C_oC_3C_4+2C_1C_2C_4-C_oC_2C_5)n^4 + 3C_1C_3C_4n^2 + C_1C_3C_5 = 0. \quad (21)$$

For given p', this determines the mode number n at the stability boundary.

The real oscillation frequency for marginal stability is easily computed from Eq. (19), the quadratic equation in ω, and is given by

FIG. 6. Schematic representation of Eq. (12) showing T_i versus toroidal mode number, n, for marginally stable modes at a given value of β. For some $T_{io}<T_{imax}$ there is a range of unstable modes with $n_1<n<n_2$. If T_i is increased, FLR stabilization increases and for $T_i>T_{imax}$ all modes are stable. Thus, for a given β, the stability boundary is determined by the mode with the maximum T_i.

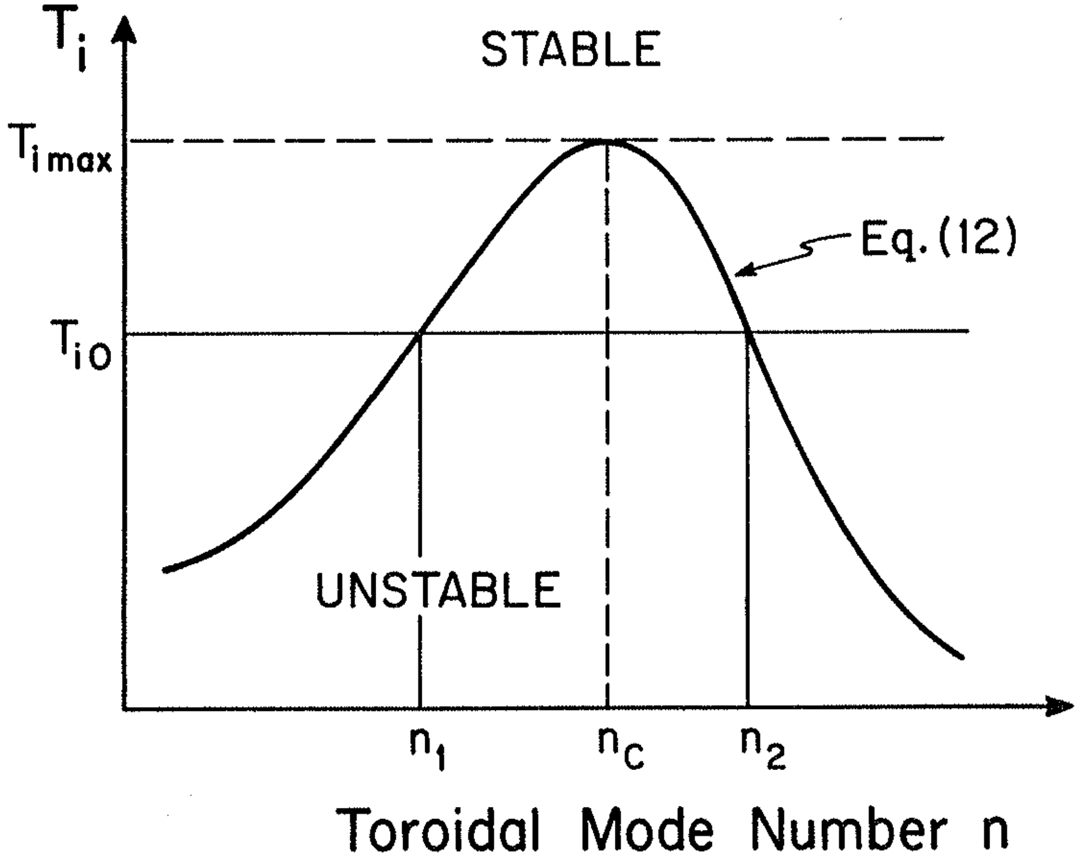
T_i
STABLE
$T_{i\,max}$
Eq. (12)
T_{i0}
UNSTABLE
n_1
n_c
n_2
Toroidal Mode Number n

$$\omega = -\frac{n}{e} T_i \frac{(n^2C_4+C_5)}{(n^2C_o+C_1)} \qquad (22)$$

In the case where the mode is higly localized it can be easily seen that $\omega \simeq (1/2)\omega_i^*$ where ω_i^* is the local diamagnetic frequency.

In summary, determining the stability boundary consists of solving five simultaneous equations: Eq. (13) which is an ordinary differential equation in χ which is solved on each flux surface and determines the structure of the modes along field lines, Eq. (18) which is an ordinary differential equation determining the structure in the radial ϕ-direction for a given mode number n, Eq. (20) which determines the ion temperature for a given n, Eq. (21) which determines the toroidal mode number at the stability boundary, and Eq. (22) which determines the oscillation frequency. This solution procedure was applied using the experimental pressure profiles to find the marginally stable beta at a given ion gyroradius, ρ_i. Results, shown in Fig. 7 indicate the strong stabilizing influence of finite gyroradius.

FIG. 7. Finite gyroradius kinetic theory prediction for the critical β versus ρ_i, where ρ_i is the ion gyroradius on the separatrix in the bridge. The theory is solved for the Levitated Octupole device.

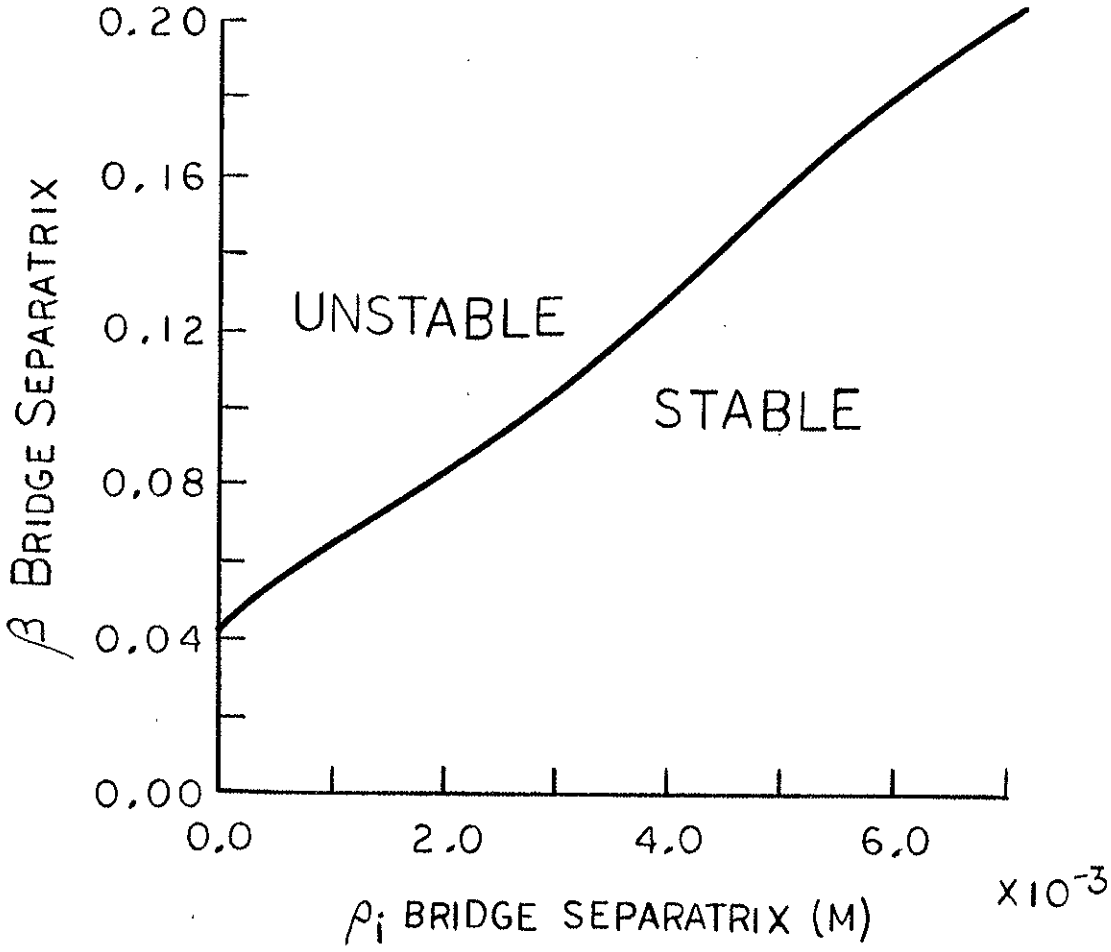
0.20
0.16
0.12
0.08
0.04
0.00
β Bridge Separatrix
UNSTABLE
STABLE
0.0
2.0
4.0
6.0
X10^{-3}
ρ$_i$ BRIDGE SEPARATRIX (M)

References for Chapter 3

1. M.W. Phillips, University of Wisconsin Ph.D. Thesis, DOE/ET/53051-29 (1982).

2. I.B. Bernstein, E.A. Frieman, M.D. Kruskal, R.N. Kulsrud, Proc. Roy. Soc. A 244, 17 (1958).

3. M.N. Rosenbluth, C.L. Longmire, Ann. Phys. 1, 120 (1957).

4. H.P. Furth, J.K. Killeen, M.N. Rosenbluth, and B. Coppi, Plasma Physics and Controlled Nuclear Fusion Research, Vol. I, (IAEA, Vienna, 1966).

5. L.C. Bernard and R.W. Moore, Phys. Rev. Lett. 46, 1286 (1981).

6. R.Y. Dagazian and R.B. Paris, Plasma Physics 24, 661 (1982).

7. W.M. Tany, J.W. Connor, and R.J. Hastie, Nucl. Fusion 20, 1439 (1980).

8. J.W. Connor, L. Chen, and M.S. Chance, PPPL 1957 (1982).

9. R.Y. Dagazian and R.B. Paris, Ann. Phys. 140, 101 (1982).

10. T. Ohkawa and D.W. Kerst, Nuovo Ciemento 22 785 (1961).

11. J.L. Johnson, R.M. Kulsrud, K.E. Weimer, Plasma Physics 11, 463 (1969).

12. D.A. D´Ippolito, E.A. Adler, Y.C. Lee, Phys. Fluids 23, 794 (1980).

13. M.N. Rosenbluth, N.A. Krall, N. Rostoker, Nucl. Fusion, 1962 Supp. Part. 1, 143 (1962).

14. E.A. Adler and Y.C. Lee, Phys. Fluids 24, 1086 (1981).

15. G.O. Spies, Phys. Fluids 19, 427 (1976).

16. P.J. Catto, W.M. Tang and D.G. Baldwin, Plasma Physics 23, 639 (1981).

17. X.S. Lee and P.J. Catto, Phys. Fluids 24, 2010 (1981).

CHAPTER 4

High Beta--Experimental Results

This chapter contains a brief summary of the optimization of the plasma guns to obtain high beta, a survey of the high beta plasmas obtained, and a more complete discussion of the equilibrium and stability properties of some representative plasmas. In particular, plasmas are found to be stable far in excess of the ideal MHD limit of β=4.33%, and often their equilibrium properties differ widely from ideal MHD equilibrium predictions.

4.A. Optimization of Gun Plasmas

The high beta plasmas are created from simultaneous or nearly simultaneous injection of three Marshall guns. Each gun is individually optimized for production of high beta, and optimal results from the configuration are achieved when each gun is operated at its "personal" best.

The gun plasma parameters are most sensitive to the gun capacitor bank voltage, the gas fill pressure, and the resistance of the transmission line. Broad ranges of other variables can be found over which gun performance is relatively unaffected. These include the delay between the gas puff and the gun high voltage trigger, the transmission line inductance and the length of the inner electrode. The optimal value of the gun voltage depends critically on the resistance of the transmission line. Figure 1 shows the behavior of electron density and temperature as a function of gun voltage for different amounts of resistance added to the transmission line. The amount added varies from zero to enough to critically damp the capacitor bank. The densities and temperatures quoted are measured on the separatrix between the outer ring and wall at 400 μsec after injection of the gun. Resistance was added to the transmission line in order to reduce the number of oscillations of the gun current and voltage and potentially minimize the production of impurities and cold plasma that accompanies each subsequent oscillation after the main burst of plasma. It can be seen that additional resistance requires increasing the capacitor bank voltage in order to achieve optimal parameters; however, the maximum value of the nT product is not significantly different for any of the resistance values except for the case of full damping resistor where both the density and temperature are still rising at the highest voltage tested. Therefore, for the high β experiments, the gun was operated with either no additional resistance or one-quarter of the critical damping resistance. Plasma density increases almost linearly with increasing gas fill pressure in the gun (Fig. 2). The density eventually falls at sufficiently high gas pressure for a fixed gun voltage, however, if the voltage is increased or the resistance reduced, the linear behavior can be sustained to a higher gas pressure. Comparison of the experimental data with the predicted densities if 100% of the injected gas is ionized indicates that the

FIG. 1. Density and temperature versus gun voltage for different amounts of resistance in the transmission line. Peak value of the nT product does not improve significantly when resistance is added.

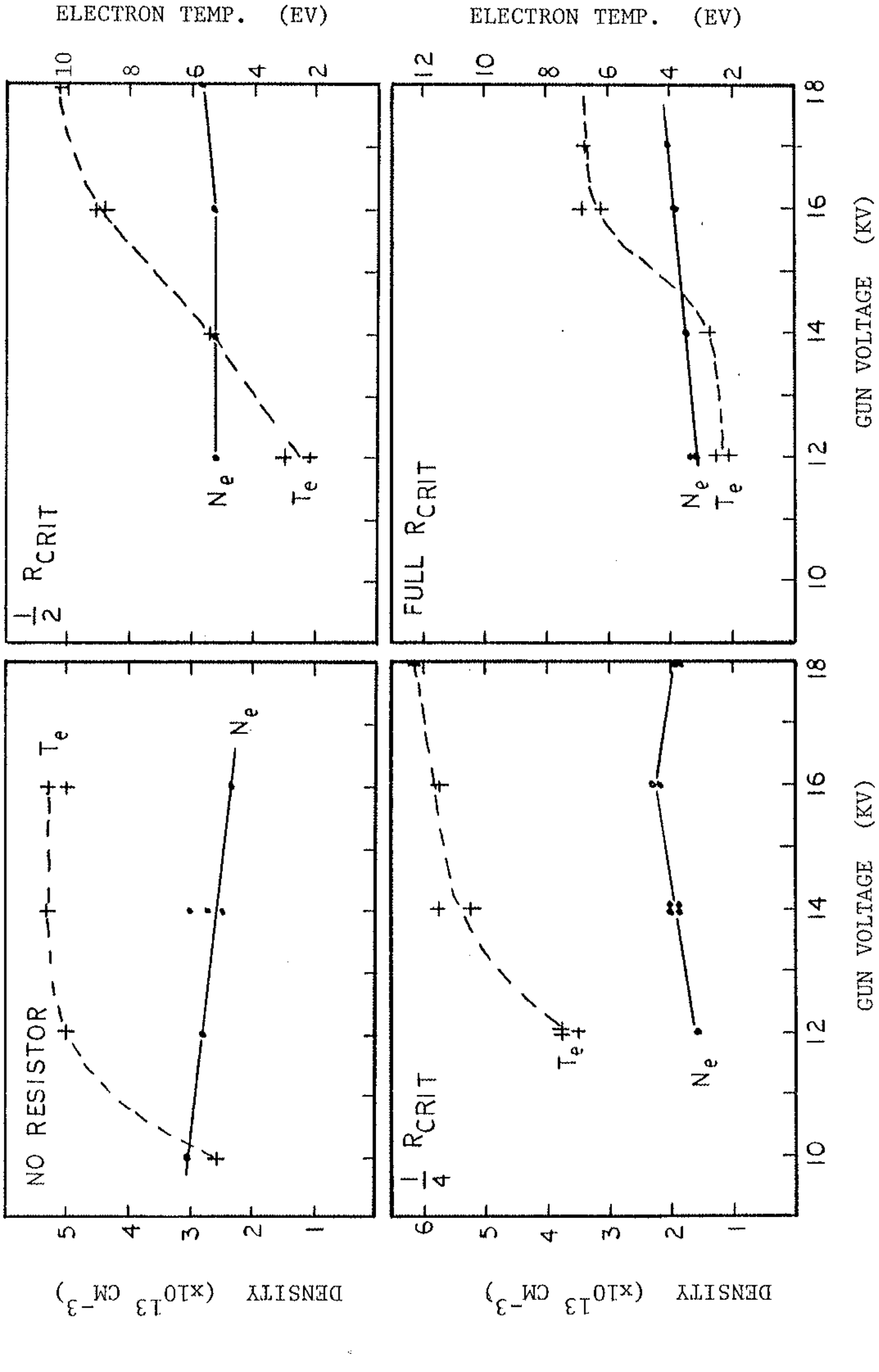
NO RESISTOR
1/2 R_CRIT
1/4 R_CRIT
FULL R_CRIT
N_e
T_e
ELECTRON TEMP. (EV)
DENSITY (x10^13 CM^-3)
GUN VOLTAGE (KV)
10
12
14
16
18
2
4
6
8
10
12
1
2
3
4
5
6

ionization fraction is approximately 75%. The deviation from linear behavior at low gas pressure may be due either to a larger percentage ionization or an increased utilization of gas adsorbed on the gun electrodes.

For a fixed gun voltage the electron temperature decreases as gas pressure is increased (Fig. 3). Although higher temperatures can be recovered if the gun voltage is increased, typically the peak temperature at high gas pressure is below that for the lower gas pressures.

Temperature and density are relatively insensitive to the delay between the gas puff and application of the gun high voltage (Fig. 4) for delay values between 500 μsec and 1500 μsec. For delay times shorter than 500 μsec, spectroscopic observations indicate that the arc breakdown does not occur at the rear of the gun and thus part of the input gas is not ionized. The addition of up to 300 nH series with the transmission line does not significantly affect the gun performance. Typical operating parameters for the big guns are shown below. Similar optimization was performed on the intermediate density gun.

FIG. 2. (Upper figure). Density versus gas fill pressure in the plasma gun plenum. At pressures above 50 psia, the fraction of the input gas that is ionized and trapped in the Octupole field is approximately 75%.

FIG. 3. (Lower figure). Electron temperature versus gun voltage for different gas fill pressures in gun. For higher gas pressure, a higher gun voltage is required to achieve the same temperature.

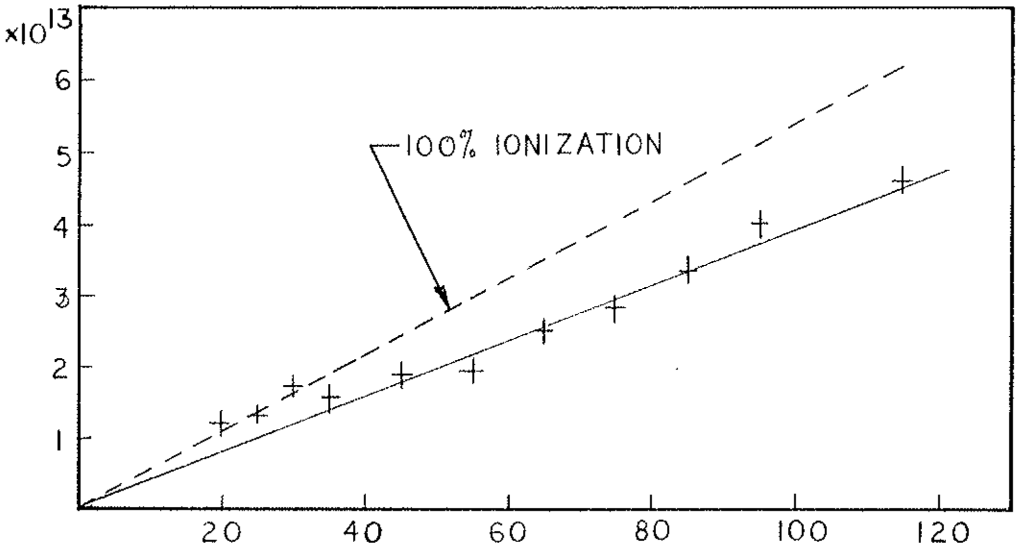
x10^13
6
5
4
3
2
1
100% IONIZATION
20
40
60
80
100
120

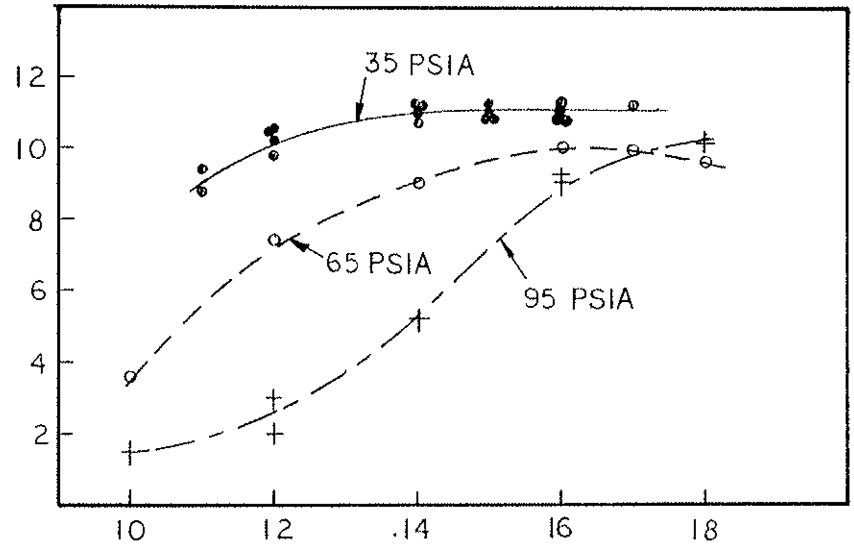
12
10
8
6
4
2
35 PSIA
65 PSIA
95 PSIA
10
12
.14
16
18

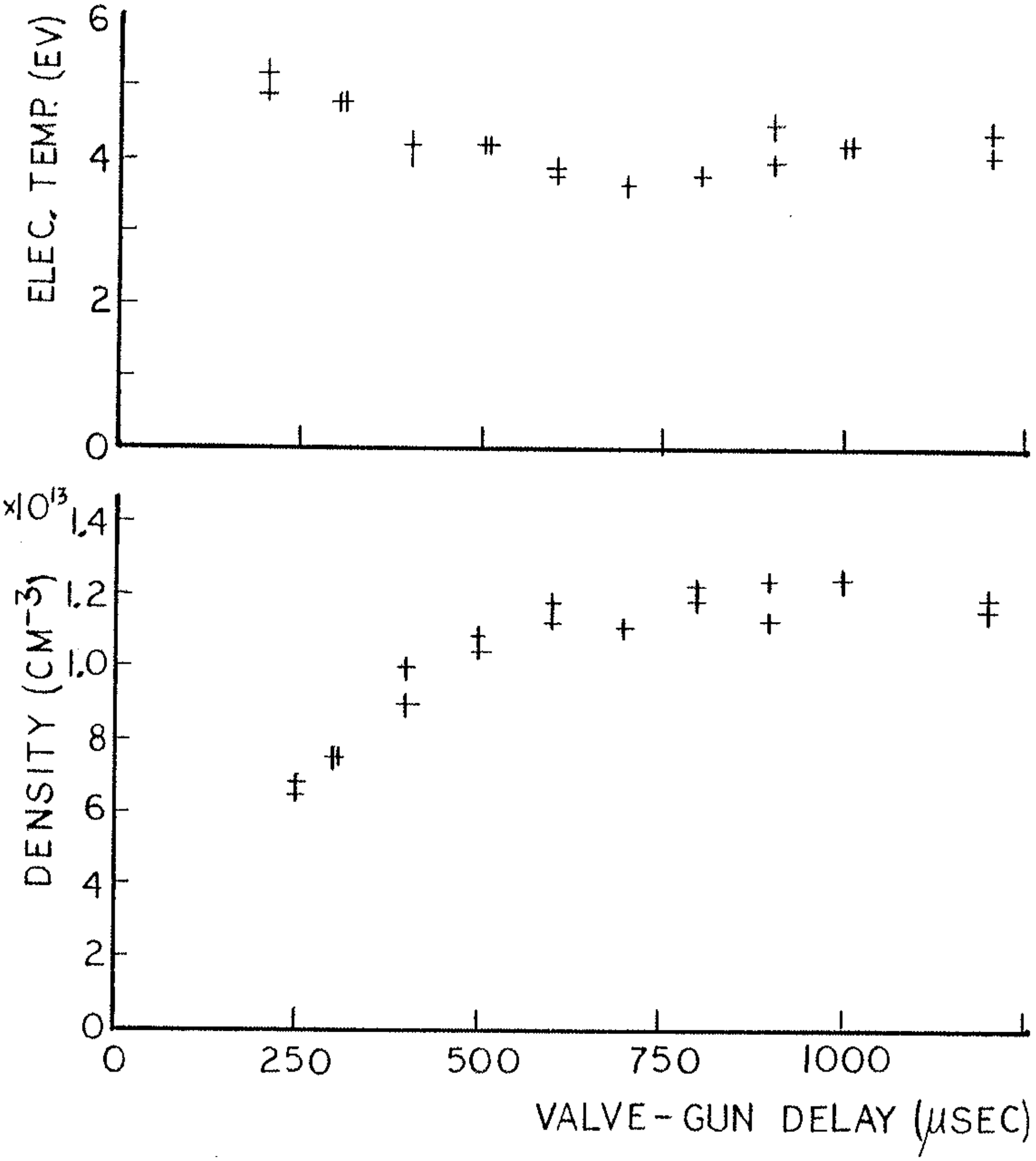

FIG. 4. Electron temperature and density as a function of the valve-gun delay time (250 μsec - 1200 μsec). For times longer than 500 μsec, the plasma parameters are not a strong function of the delay time.

TABLE 1

	Big Gun #1, #2	I.D. Gun
VALVE-GUN DELAY	600-700μsec	400 μsec
GUN VOLTAGE	15-16 kV	16 kV
GAS PRESSURE	95-115 psia	95-115 psi
INDUCTANCE (w/o gun)	200 nH	600 nH
RESISTANCE	$\lesssim 1/4\ R_{crit}$	$<1/4\ R_{crit}$

Simultaneous injection of gun plasmas leads to higher plasma beta than any gun can produce individually, however, the resultant beta is less than the sum of the separate plasma beta (Table 2). The decrease in the temperature of the combined plasma was typical, but not a rule. Ten percent changes in electron temperature in both directions have been observed.

TABLE 2

	Big Gun #1	Big Gun #2	Combined
N_e	2.85×10^{13} cm^{-3}	3.1×10^{13} cm^{-3}	4.8×10^{13} cm^{-3}
T_e	10.0eV	9.7 eV	8.7 eV
J_{sat}	190 ma	223 ma	290 ma

Slight increases of up to 10% have been observed if plasma from one gun is injected 100 μsec before the simultaneous injection of the remaining two guns. The process of injection of two or more gun plasmas is not well understood and may depend on the relative position of the guns toroidally. These guns were located at 135° (B.G. #1), 155° (Int. Gun), and 315° (B.G. #2).

4.B. Alternative Methods of Obtaining High β

Various methods of attaining higher plasma β than the gun plasma were examined, such as ohmic heating with oscillating electric field in the toroidal or poloidal direction, gun injection into ohmic discharges, and ion cyclotron resonance heating (ICRH) of gun plasmas. Two methods, oscillating poloidal electric field and ICRH look promising although neither method succeeded in actually producing higher β plasmas than could be achieved with the guns alone. The advantage of heating a gun plasma to achieve higher beta is that one could watch the plasma instability turn on. For gun plasmas, the plasma may go ballooning unstable early in time causing poor confinement and a large plasma loss and then settle into a stable configuration. Thus, in some sense, experiments with the gun plasmas alone are exploring regions of parameter space that are stable to ballooning modes whereas by heating one might hope to observe the instability growth.

Heating plasma with an oscillating poloidal electric field has been studied extensively[1] in lower density plasmas ($n_c < 1 \times 10^{13}$ cm^{-3}). These experiments indicated coupling of significant power to the plasma; however, a current driven instability degraded plasma confinement and prevented significant heating without plasma loss. At the higher plasma density in these experiments, there is some indication that the plasma is not as unstable. Sufficient power is coupled to the plasma to sustain the beta at modest levels, however, arcing of the toroidal gap at voltages above 75 volts prevents coupling in enough power to actually increase plasma beta above the peak values.

ICRH experimental results are promising (Fig. 5)[2]. Plasma beta up to 3% is sustained for 10 msec by gas puffing and heating. For this case $n_e = 1 \times 10^{13}$ cm^{-3}, $T_e = 15$ eV and $T_i \sim 40$ eV, and the input power is 1.1 MW. Plasma beta continues to improve with input power up to the highest power available; however, additional power is required to sustain the highest beta plasmas.

FIG. 5. Electron and total plasma beta versus RF power coupled into the plasma.

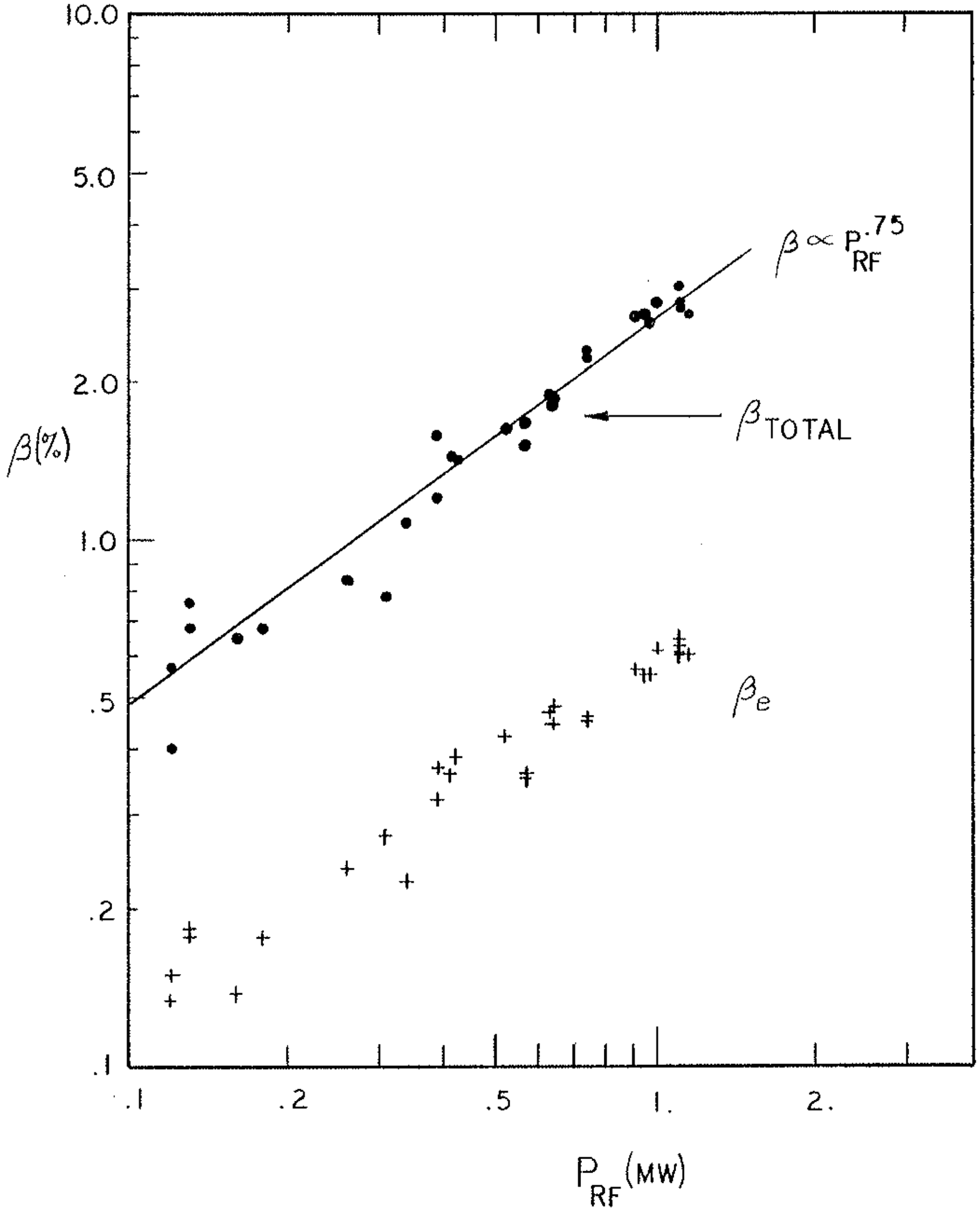
10.0
5.0
2.0
1.0
.5
.2
.1
$\beta(\%)$
.1
.2
.5
1.
2.
P_{RF}(MW)
$\beta \propto P_{RF}^{.75}$
β_{TOTAL}
β_e

4.C. High Beta Plasmas - Introduction

Plasma injection occurs at peak magnetic field so there is negligible toroidal electric field during the plasma lifetime. Because the plasma lifetimes are typically short in these experiments ($\tau \sim 5$ msec), the passive crowbar is generally not required. After injection, the plasma spreads toroidally around the machine and adopts a pressure profile peaked on or very near to the separatrix after which it decays diffusively. Here, as in the theory section, β is evaluated locally on the separatrix between the outer ring and wall at 400μsec after injection. β is evaluated here since the ballooning mode should maximize in this region between the separatrix and the critical flux surface where the field lines have local bad curvature.

4.D. Toroidal and Poloidal Symmetry

At 400 μsec after injection, the plasma has fully spread around the toroid, injection transients have damped away and the separatrix pressure varies toroidally by less than 20%.

Figure 6 shows the ratios of ion saturation current taken at five different locations toroidally and poloidally to a reference probe at 45° in the lower outer bridge (LOB). Perfect axisymmetry is indicated by ratios that are independent of time. The ratios are not the same for different pairs of probes because of variations in the probe tip areas. The intermediate gun plasma (Fig. 6a) data are for an electron density, n_e, of 8×10^{12} cm^{-3} and an electron

FIG. 6. Ratio of ion saturation current at various locations to ion saturation current at 45° lower outer bridge. All probes are located on the separatrix.

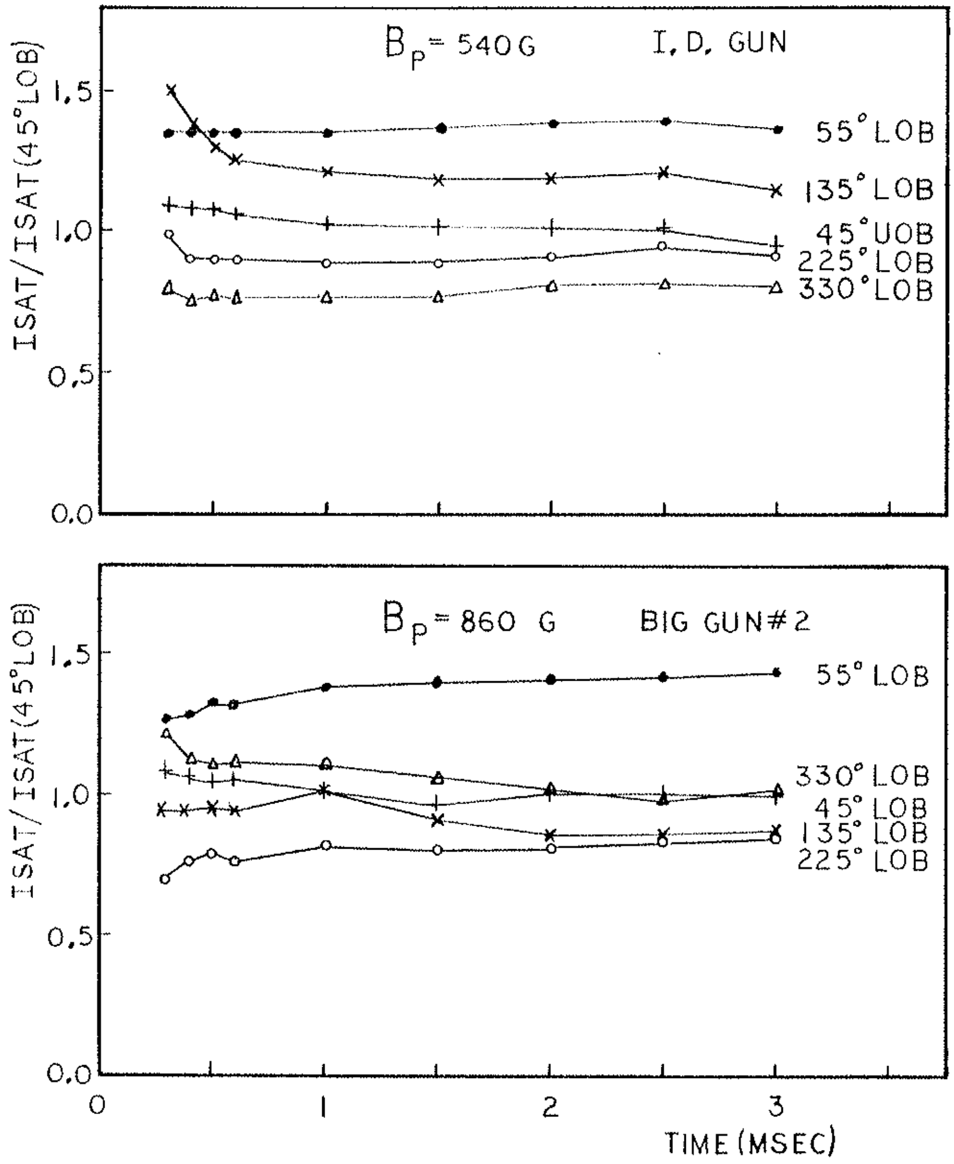
B_P = 540 G
I. D. GUN
55° LOB
135° LOB
45° UOB
225° LOB
330° LOB
ISAT/ISAT(45° LOB)
1.5
1.0
0.5
0.0
B_P = 860 G
BIG GUN # 2
55° LOB
330° LOB
45° LOB
135° LOB
225° LOB
ISAT/ISAT(45° LOB)
1.5
1.0
0.5
0.0
0
1
2
3
TIME (MSEC)

temperature, T_e, of 16 eV. For all probes except the one located near the gun injection port (135° LOB), the ratios are constant in time to within experimental error (5-10%). The probe near the gun injection port has a higher value than the other probes for the first 600-800 μsec. This may be due to ionization of neutral gas drifting out of the gun after injection or of neutrals knocked off the wall by plasma not trapped during injection. This equilibration time is sometimes as long as 1500 μsec. For big gun plasmas the results are similar but the asymmetries are typically larger. For the plasma shown in Fig. 6b, $n_e \sim 2\times10^{13}$ cm^{-3} and $T_e \sim 11$ eV at 400 μsec. Axisymmetry was examined for various gun plasmas by varying valve-gun delay time (300-800 μsec), gas pressure (5-80 psig), and magnetic field (200-1000 G). Typically, the separatrix pressure varies less than 5% over distances of five times the expected toroidal wavelength of a ballooning mode (5-10 cm), and less than 20% around the entire toroid. Radial profiles taken on the outer bridges between the hoop and wall show excellent agreement everywhere toroidally for the intermediate gun plasmas (Fig. 7a). The data have been normalized to allow comparison of profile shapes. The slight misalignment of the profiles is probably due to an uncertainty in probe position. Profile shapes for the higher density big gun plasmas do not agree as well (Fig. 7b), however, as in the previous case, the agreement is within 5% over distances of 5-10 times the ballooning toroidal wavelength (45° LOB-55° LOB).

FIG. 7a. Radial profile of ion saturation current at 5 different toroidal azimuths in the lower outer bridge for an I.D. gun plasma . Plasma density and temperature on the separatrix are $n \sim 9.5 \times 10^{12}$ cm^{-3} and $T_e \sim 15$ ev, with $B_p = 860$ G. Toroidal agreement is very good.

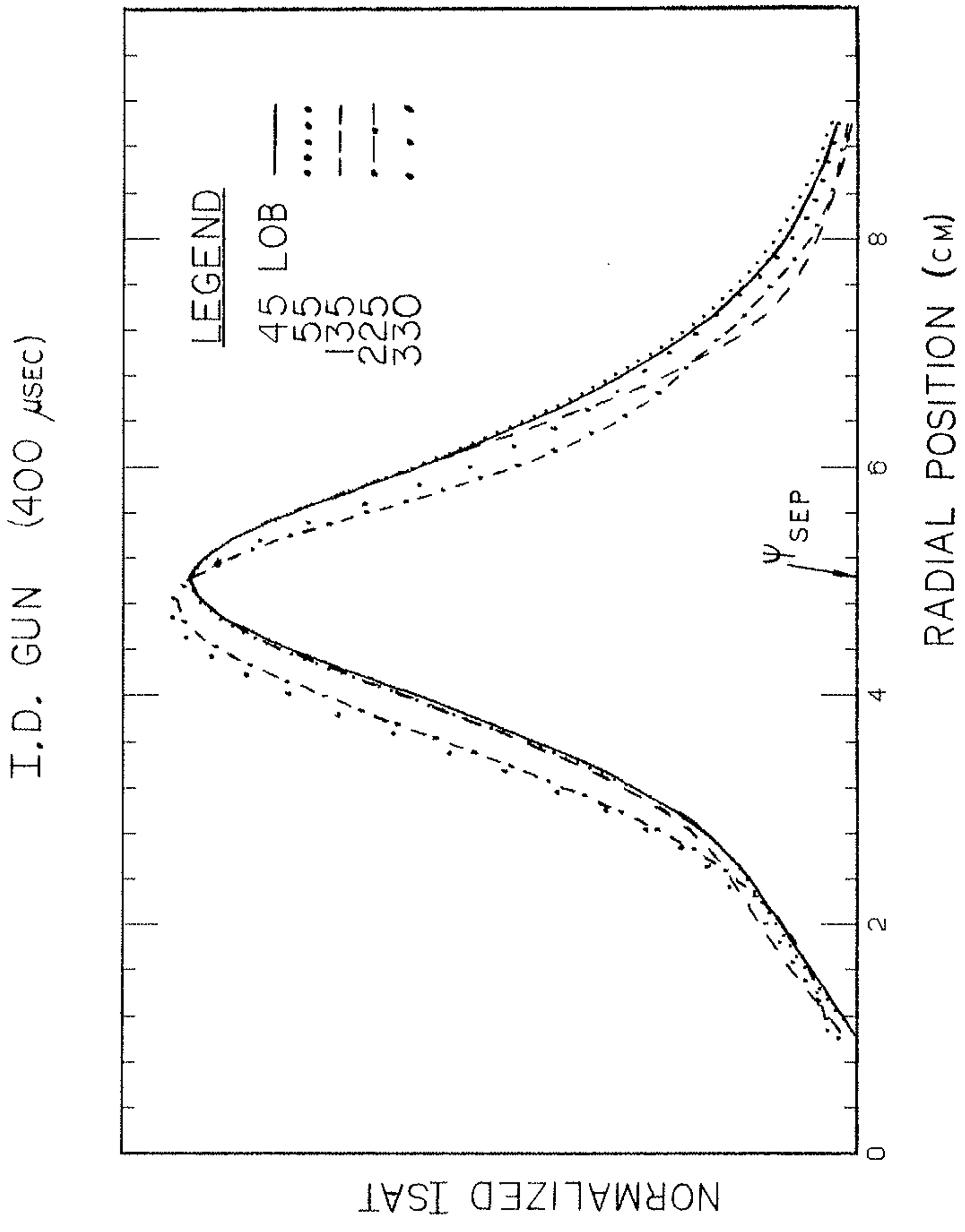
I.D. GUN (400 μSEC)
NORMALIZED ISAT
RADIAL POSITION (CM)
0
2
4
6
8
LEGEND
45 LOB
55
135
225
330
Ψ SEP

FIG. 7b. Radial profile of ion saturation current at 5 different toroidal azimuths in the lower outer bridge for a Big Gun plasma . Plasma density and temperature on the separatrix are $n \sim 1.5\times10^{13}$ cm^{-3} and $T_e \sim 6$ ev, with $B_p=380$ G. Agreement is good for small probe separation (45° to 55°), but is not as good for large separations.

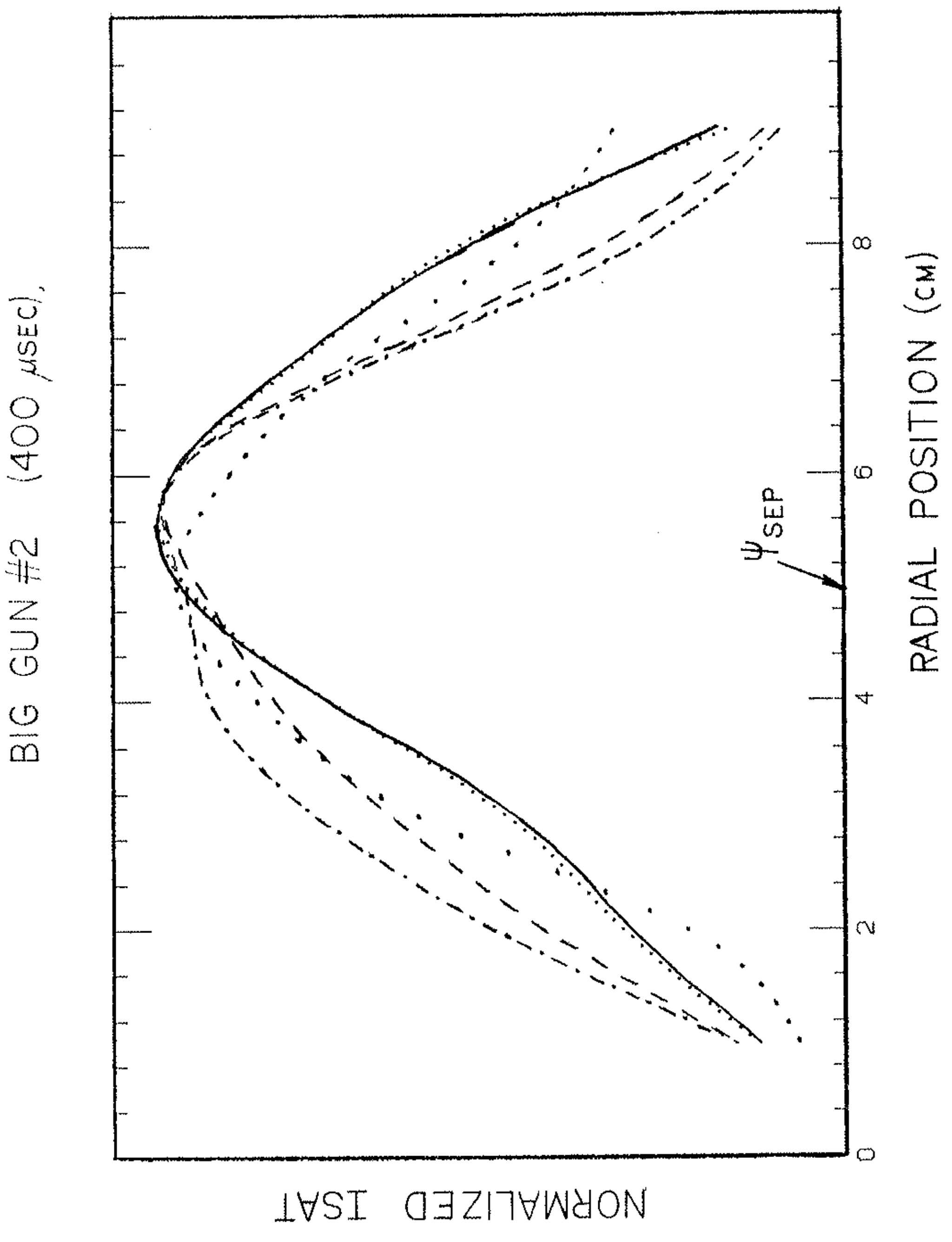
BIG GUN #2 (400 μSEC),
NORMALIZED ISAT
RADIAL POSITION (CM)
0
2
4
6
8
ψSEP

Density invariance along field lines has also been verified. Comparison of ion saturation current in the upper and lower outer bridges (Fig. 6 45 UOB/45 LOB) and separate measurements of n_e and T_e in the bridge and midcylinder (Fig. 8) indicate the agreement is within the experimental uncertainty after 300 μsec.

4.E. High Beta Plasma Parameters

A wide range of plasmas with beta significantly above the ideal MHD β limit of 4.3% have been created. Some representative cases are summarized in Table 3. These plasmas are macroscopically stable in that beta decay times are in excess of 1000 Alfvén transit times (typical MHD growth times) or 10 drift wave periods and no β-related fluctuations occur.

For these plasmas, the measured T_e and T_i are equal, as expected, since the electron-ion equilibration time is ~50 μsec which is much less than the energy decay time of ~500 μsec. Electron temperature measurements with double Langmuir probes are checked by time-dependent computer modeling of observed oxygen line radiation[3] and by measuring intensity ratios of different CIII line radiation (CIII 4647Å and CIII 977Å). Measurement of the Doppler broadening of H_β radiation indicates that the neutral hydrogen temperature is ~50% of the electron temperature. This is consistent with the measurement of equal ion and electron temperatures since in this temperature range (~10 eV), the typical energy of a neutral backscattered from the wall is ~40% of the incident ion energy[4].

FIG. 8. Measurement of density and temperature along the same field line in the bridge (dots) and on the midcylinder (circles) indicate the agreement is within experimental uncertainty after 300 μsec.

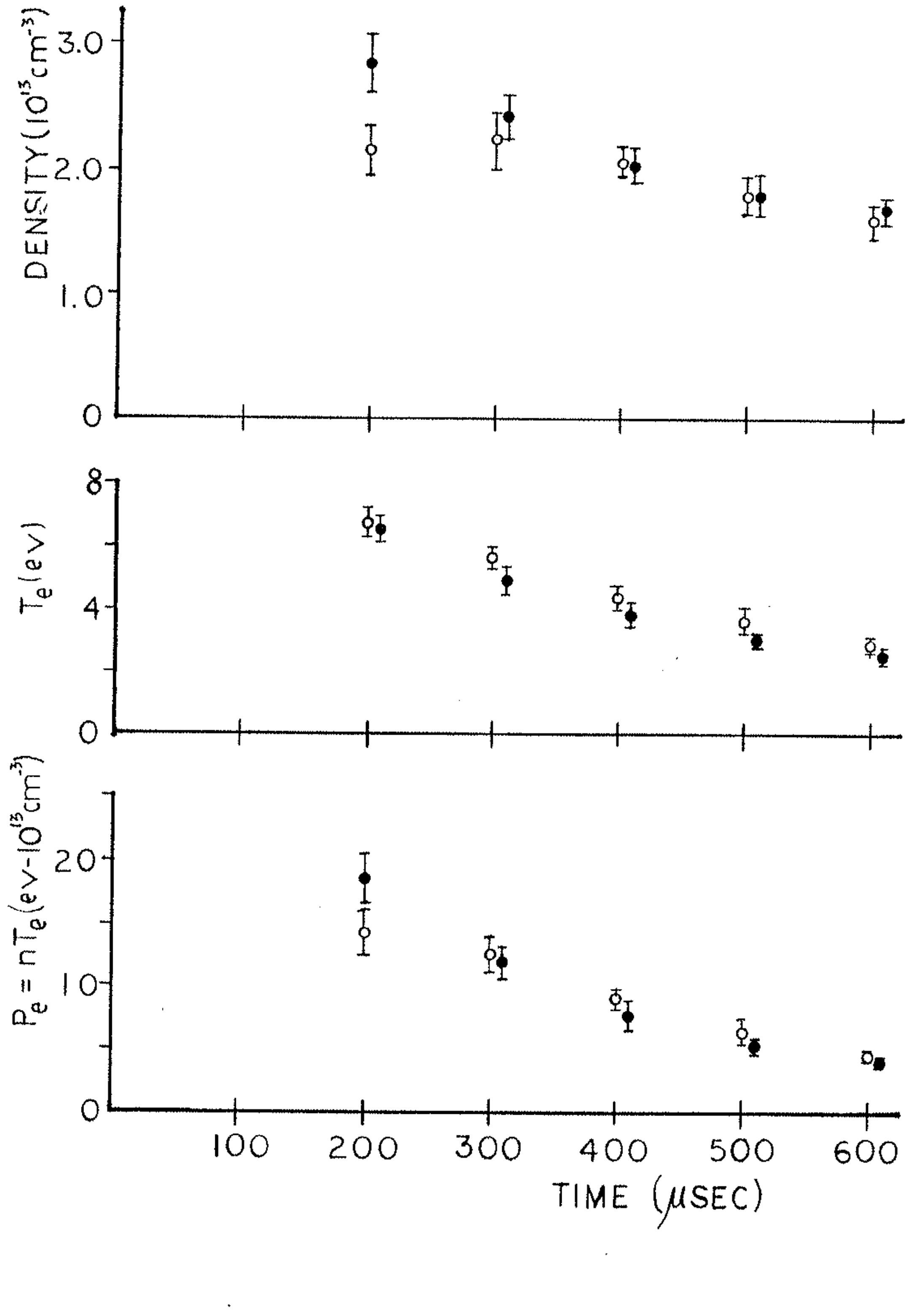
DENSITY (10^{13} cm^{-3})
3.0
2.0
1.0
0
T_e (ev)
8
4
0
$P_e = nT_e$ (ev-10^{13} cm^{-3})
20
10
0
100
200
300
400
500
600
TIME (μSEC)

TABLE 3: HIGH β PLASMA PARAMETERS

β	n	T_e	B_P	f_{ci}/ν_{ii}	τ_β/τ_{ALF}	ρ_i	$\lambda_{ii}=\lambda_{ee}\sim\lambda_{ei}$
34%	1.9×10^{13} cm^{-3}	9.0 eV	200 G	0.48	1170	1.53 cm	2.49 cm
44	5.85	13.7	380	0.55	750	0.99	1.88
30.5	5.1	10.8	380	0.44	640	0.88	1.34
11	5.7	17.9	860	1.91	2850	0.50	3.29
5.3	6.6	20.1	1429	3.27	5570	32	3.61
8	3.6	20.0	860	3.57	6230	0.53	6.49
12	.47	15.0	200	4.13	2670	2.35	2.80

The various diagnostics yield a measurement of β with a relative error of 0.25.

It can be seen that the plasmas obtained can be divided into three groups. The highest β plasmas occur at relatively low magnetic field and are highly collisional with large ion gyroradii. The ratio of ion-ion collision time to a ion gyroperiod, f_{ci}/ν_{ii}, is less than one, and the mean free path, λ, is much less than the connection length, L_c, between good and bad curvature. At a higher magnetic field, less collisional, smaller gyroradius plasmas have been obtained. The final group, represented by a β=12% plasma, is a large gyroradius plasma with $\lambda \sim L_c$. For this plasma, the electron-ion equilibration time is long enough for T_e and T_i to differ significantly, and thus we obtained β=12% at $n_e=4.7\times10^{12}$ cm^{-3} with T_e=15 eV and T_i=7 eV.

The highest beta plasmas achieved to date with all three plasma guns are $\beta \sim 11\%$ at 860 G (with $n=5.7\times10^{13}$ cm^{-3} and $T_e \sim T_i \sim 18$ eV) and $\beta \sim 44\%$ at 380 G (with $n=5.9\times10^{13}$ cm^{-3} and $T_e \sim T_i \sim 14$ eV). Spatial and temporal profiles of density, temperature and plasma pressure are illustrated in Fig. 9 for the $\beta \sim 11\%$ case. Beta decay times are 200 μsec (1000 Alfvén times) and 350 μsec (3000 Alfvén times) for the 44% and 11% cases, respectively. Hereafter, however, two lower β plasmas will be discussed (8% and 35%) because their equilibria are more fully documented and it is easier to distinguish the dominant effects that lead to their enhanced stability.

FIG. 9. β=11% plasma. (a) Electron density and temperature on the separatrix and (b) pressure and electron temperature radial profiles at t=400 μsec. Radial profiles are measured between the outer ring and wall. β is evaluated at t=400 μsec on the separatix field line (5 cm from ring) where B=860 G. Typical error bar of 10% due to shot to shot variation is shown. t=0 is the time of plasma injection into the machine.

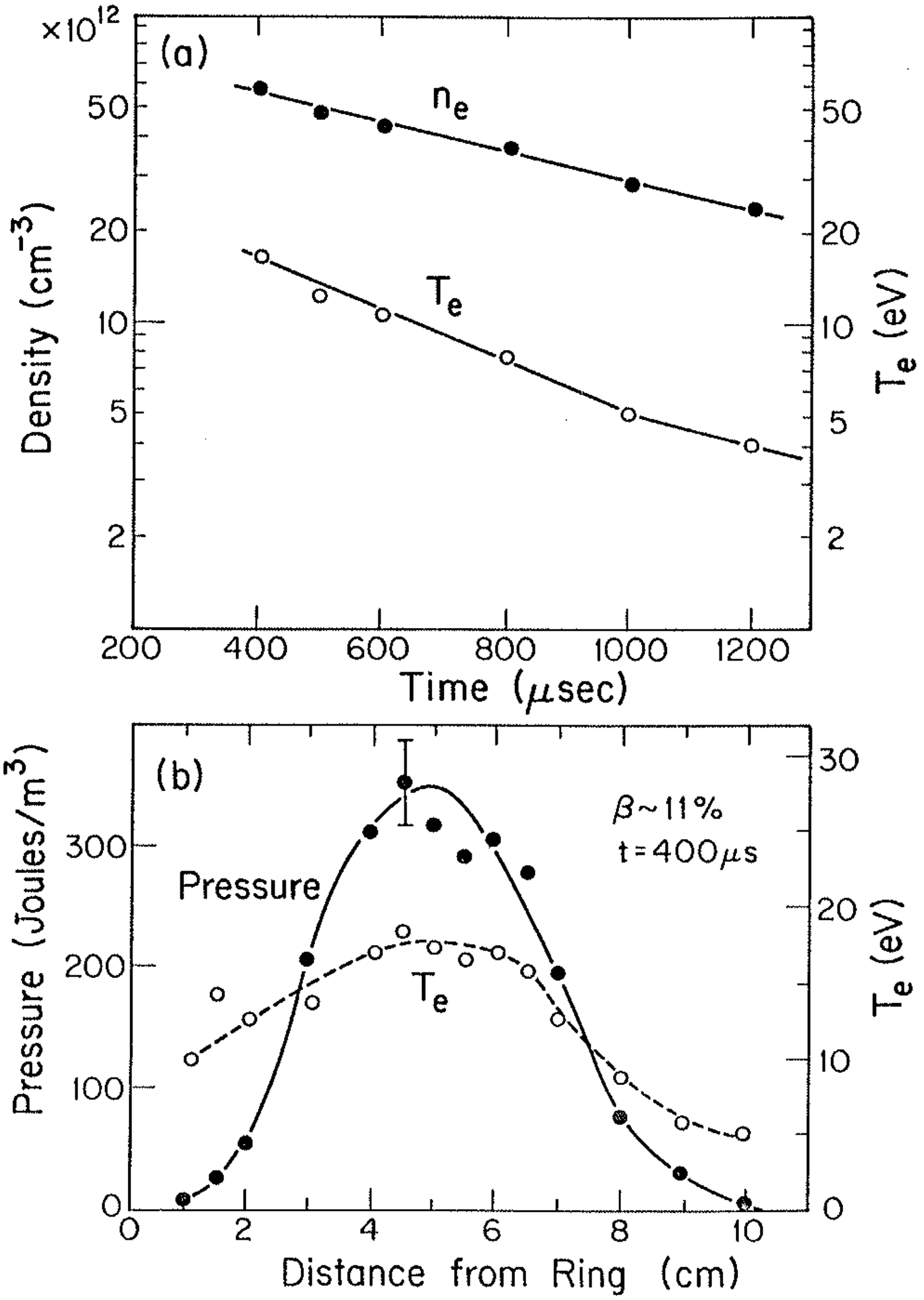
(a)
×10^12
Density (cm^-3)
50
20
10
5
2
n_e
T_e
50
20
10
5
2
T_e (eV)
200
400
600
800
1000
1200
Time (μsec)
(b)
Pressure (Joules/m^3)
300
200
100
0
Pressure
T_e
β~11%
t=400μs
30
20
10
0
T_e (eV)
0
2
4
6
8
10
Distance from Ring (cm)

The β=8% case is obtained with B_p=860 G, n=3.6×10^{13} cm^{-3} and T_e~T_i~20 eV. For this case, there are 5 ion gyroradii in a pressure scale length (25 between the ring and wall), and $\omega_{ci}\tau_{ii}$=23, where $\omega_{ci}\tau_{ii}$ is 2π times the ratio of ion-ion collision time to an ion gyroperiod. The β decay time is 600 μsec or ~6000 Alfvén times. Measured equilibrium diamagnetism agrees well in both magnitude and shape with ideal single fluid theory predictions (Fig. 10a). The magnetic Reynolds number, S, (resistive diffusion time/Alfvén time) is 1500, so that the effect of resistivity is negligible (see Chapter 5).

At a lower magnetic field, in the highly collisional, large gyroradius regime, we have obtained β~35%, with n_e=2×10^{13} cm^{-3} and T_e~T_i~8 eV and a poloidal field of 200 G (Fig. 11). As stated above, the coulomb mean free paths are much less than the connection length between good and bad curvature (0.5 m). Finite ion gyroradius effects will be important since there are barely two ion gyroradii in a pressure scale length (ρ_i/L_p=.42). Gyroviscous effects are also important in this plasma since the ordinary Reynolds number $R=V_A\ell\rho/\mu$~1 and $\omega_{ci}\tau_{ii}$=3 where V_A, ℓ, ρ, and μ are the Alfvén speed, perpendicular scale length, mass density, and ordinary viscosity respectively. A Reynolds number of unity implies that inertial and viscous forces are of comparable magnitude. The magnetic Reynolds number is 100, so resistivity can again be ignored, and the β decay time is ~270 μsec, which is 1000 Alfvén transit times. For this plasma, the measured diamagnetism is a

FIG. 10. Single fluid theoretical and experimental radial profile (between outer ring and wall) of perturbation, ΔB, to the poloidal magnetic field due to the equilibrium diamagnetic currents at t=400 μsec for (a) $\beta=8\%$ and (b) $\beta\sim35\%$. Typical error bar is shown.

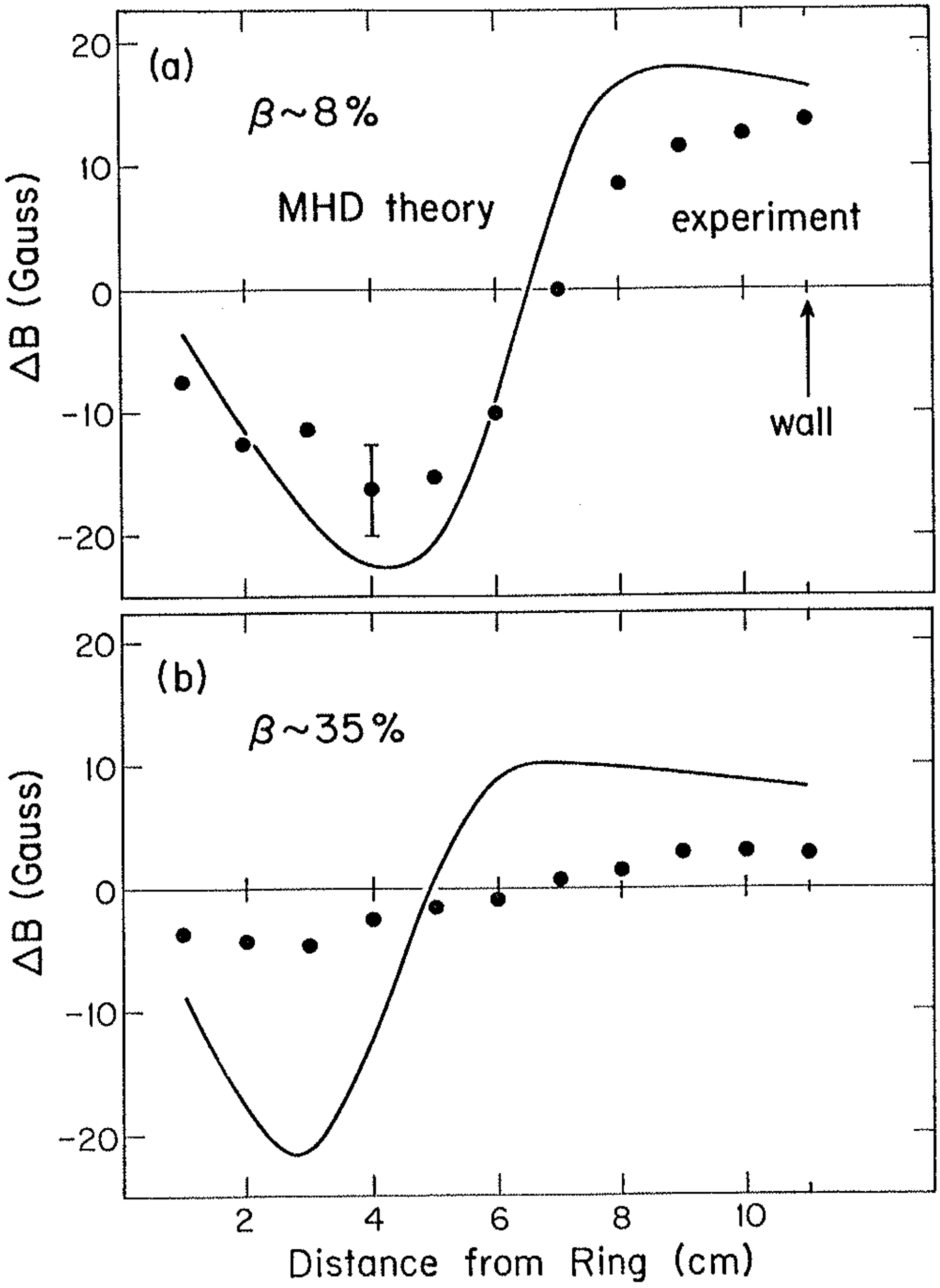
(a)
β~8%
MHD theory
experiment
wall
ΔB (Gauss)
20
10
0
-10
-20
(b)
β~35%
ΔB (Gauss)
20
10
0
-10
-20
2
4
6
8
10
Distance from Ring (cm)

FIG. 11. β~35% plasma. (a) Electron density and temperature on the separtrix and (b) pressure and electron temperature radial profiles at t=400 μsec. B=200 G.

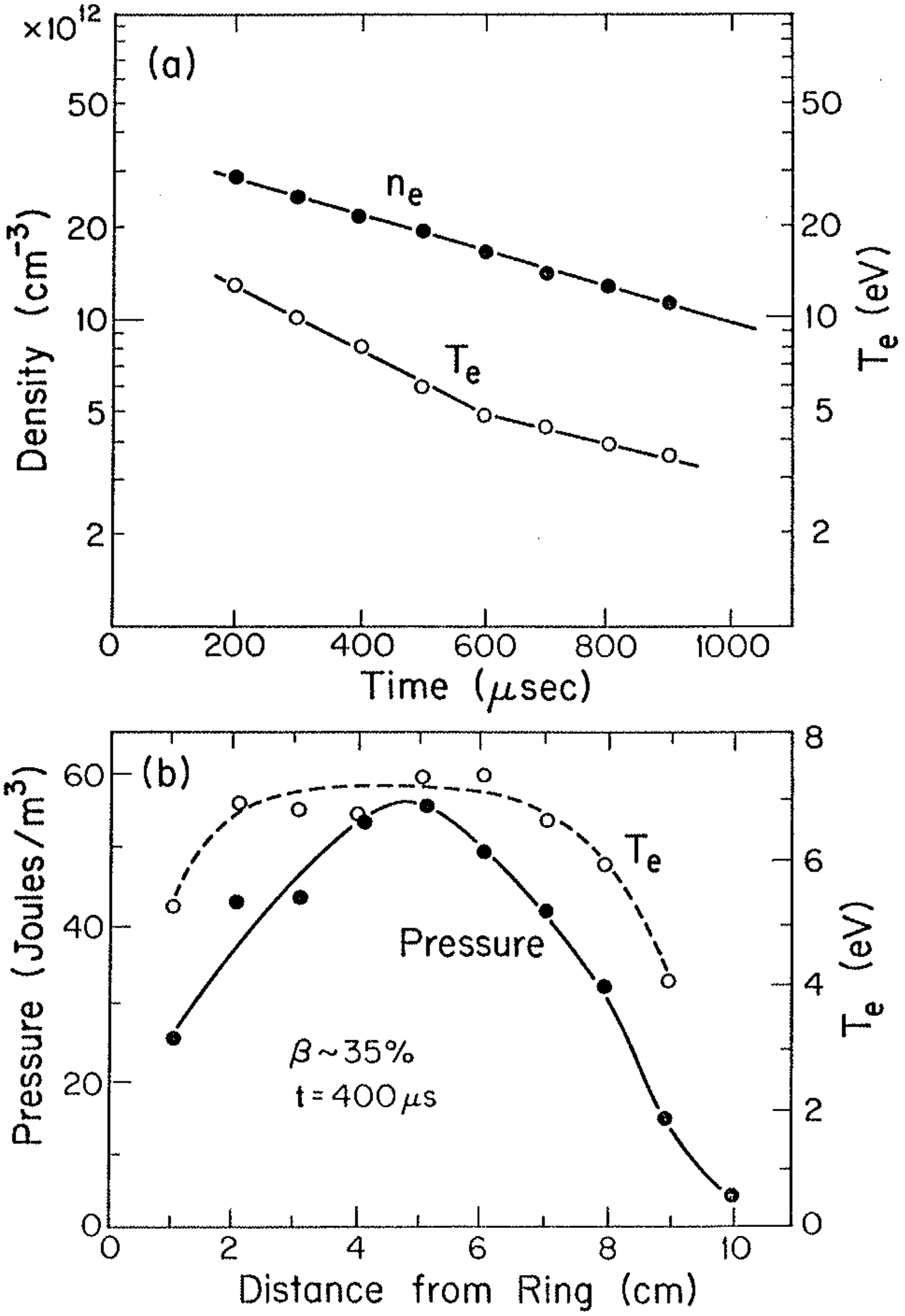
×10^12
(a)
n_e
T_e
Density (cm^-3)
T_e (eV)
50
20
10
5
2
0
200
400
600
800
1000
Time (μsec)
(b)
T_e
Pressure
β ~ 35%
t = 400 μs
Pressure (Joules/m^3)
T_e (eV)
60
40
20
0
8
6
4
2
0
2
4
6
8
10
Distance from Ring (cm)

factor of five smaller than predicted by ideal single fluid theory, but the profile shape is correct (Fig. 10b).

For the plasmas we have studied, no beta related fluctuations have been identified to within $\tilde{B}/B<0.1\%$ and $\tilde{n}/n<5\%$. Although fluctuation levels for magnetic field, electrostatic potential, and density maximize in the bad curvature region, these fluctuations are typically small when the beta is highest, with the fluctuation level increasing as the plasma beta decreases. Classical particle transport ($D \sim nT^{-1/2}B^{-2}$) is observed in the low magnetic field (B_p=200 G), high beta plasma ($\beta \sim 35\%$). The particle diffusion rate is above the classical rate for all other cases studied in the range of β from 1% to 35%, and the enhancement factor above classical increases with magnetic field.

Diffusion and fluctuations will be examined in more detail in Chapter 6.

4.F. High Beta Equilibrium

In order to interpret these results the equilibrium must be analyzed further.

In Section 3B it was shown that the quantity $\Delta B/B\beta$ depends only on the profile shape; i.e. for a given profile shape $\Delta B/B\beta$ does not depend on the magnetic field or β. Measurement of this quantity, however, indicates a strong dependence on the magnetic field (Fig. 12). As the magnetic field is raised and the ratio of ion gyroradius to density scale length decreases, there is a steady

FIG. 12. Theoretical and experimental fractional change in the magnetic field (at the separatrix in the bad curvature region), $\Delta B/B$, due to plasma diamagnetic currents versus the poloidal magnetic field strength. $\Delta B/B$ is normalized to the separatrix β value so that single fluid theory yields a horizontal line (Sect. 3C).

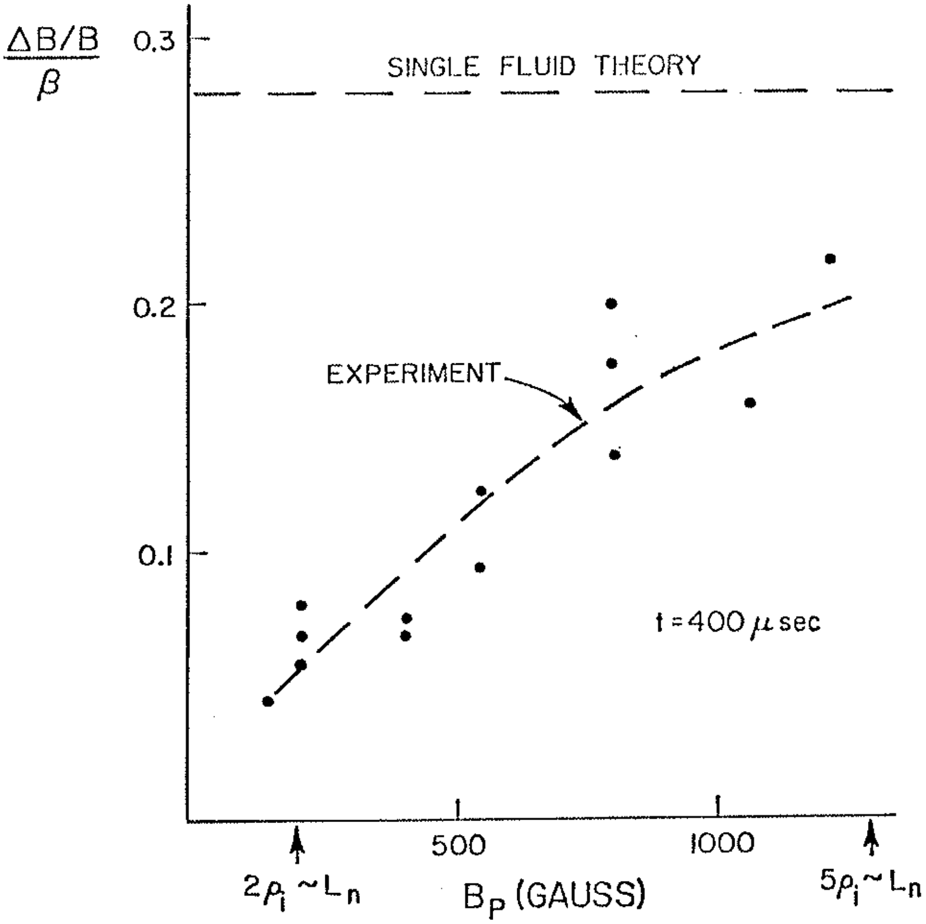

$\frac{\Delta B/B}{\beta}$
0.3
0.2
0.1
SINGLE FLUID THEORY
EXPERIMENT
t = 400 μ sec
500
1000
$2\rho_i \sim L_n$
B_P (GAUSS)
$5\rho_i \sim L_n$

improvement in the agreement between the experimental values and the predictions of single fluid theory. For these data, the value of β ranges from 2% to 30% and typically, the β decreases as the field is increased. The theoretical value has been shown as a constant because its value on the separatrix is a weak function of the profile shape.

Similarly, because the profile shape changes only slightly during a beta decay time, both $\Delta B/B$ and β should have the same decay time. Experimentally, however, $\Delta B/B$ decays more rapidly than β. This is true even at high field where the β decay time is 520 μsec and $\Delta B/B$ decays with a time constant of 250 μsec (Fig. 13).

It was shown above that independent of the absolute magnitude of ΔB, the shape of the experimental and theoretical ΔB profiles agreed for both large and small gyroradius plasmas at 400 μsec after injection. This agreement between the predicted and measured shape continues throughout the decay of the plasma (Fig. 14). An interesting thing to note about the profile shape is that the plasma "diamagnetic" current actually causes the magnetic field to increase near the ring and wall. As pointed out in Chapter 3 this is a consequence of the fact that the resistive skin time for the magnetic field diffusing into the aluminum ring and wall is much longer than either the rise or decay time of the plasma diamagnetic effect. This effect can be clearly seen in the data. Detailed measurement of ΔB near the ring surface shows a positive magnetic field perturbation which increases as the ring is approached and

FIG. 13. Comparison of experimental $\Delta B/B$ to electron β. Ideal MHD predicts similar decay times, however, a more rapid decay is observed for $\Delta B/B$, even at high magnetic fields.

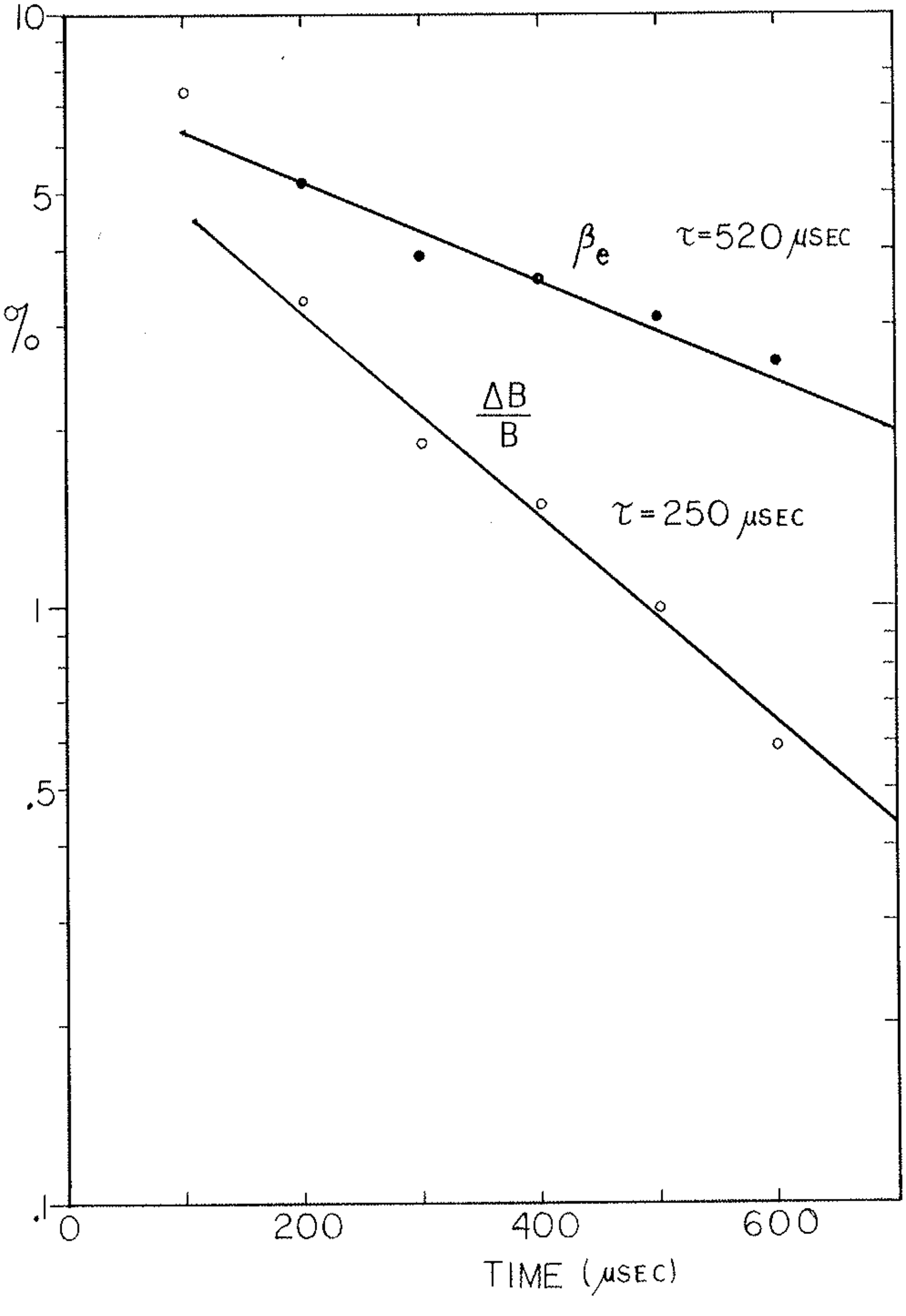
10
5
%
1
.5
.1
0
200
400
600
TIME (μSEC)
β_e
τ=520 μSEC
$\frac{\Delta B}{B}$
τ=250 μSEC

FIG. 14. Comparison of experimental and theoretical radial profiles of ΔB in bridge region for t=400 μsec and 1400 μsec. Agreement in sign and shape is good at all times. The magnitudes have been adjusted to allow shape comparison.

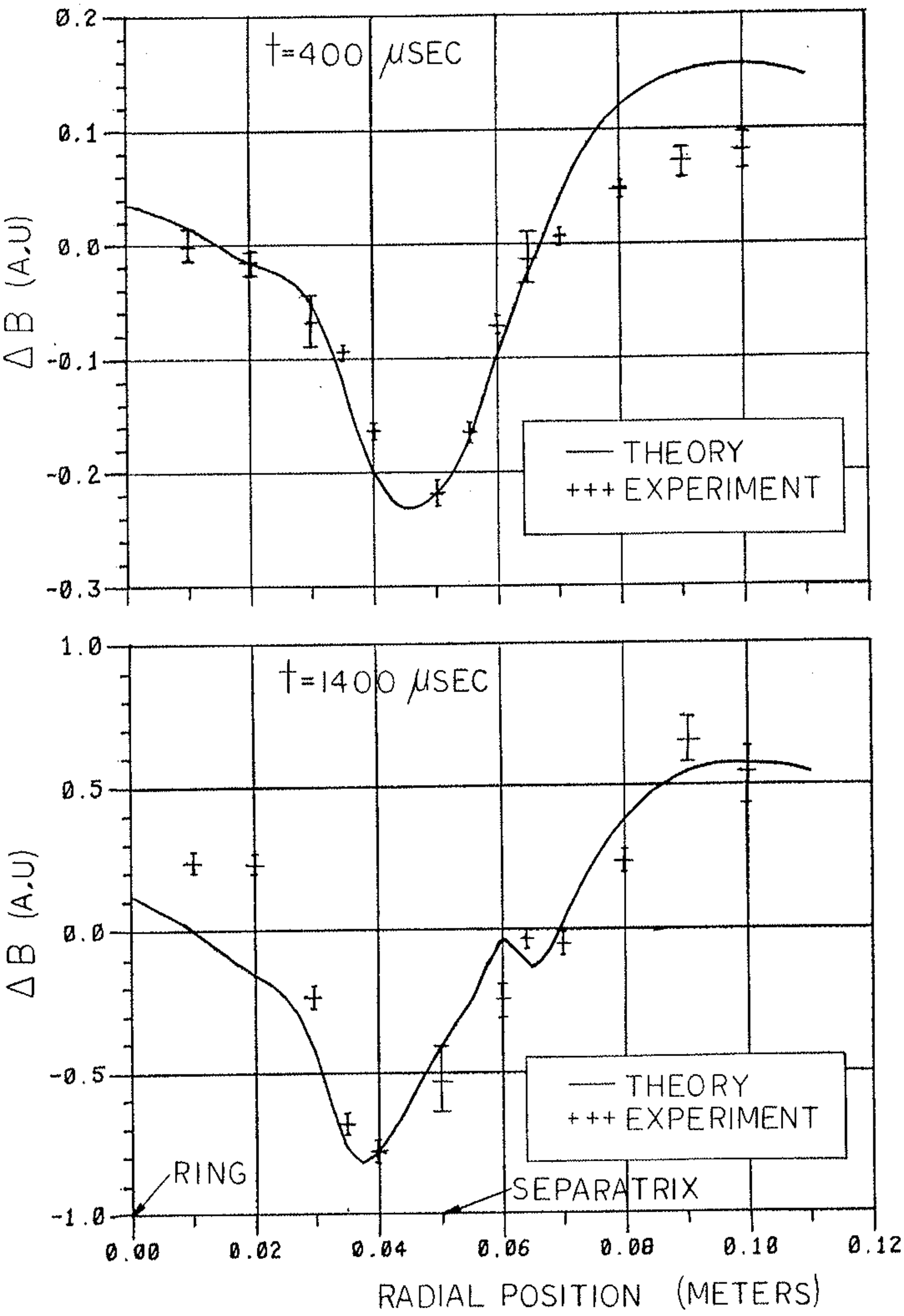
t=400 μSEC
THEORY
+++ EXPERIMENT
ΔB (A.U)
0.2
0.1
0.0
-0.1
-0.2
-0.3
t=1400 μSEC
THEORY
+++ EXPERIMENT
ΔB (A.U)
1.0
0.5
0.0
-0.5
-1.0
RING
SEPARATRIX
0.00
0.02
0.04
0.06
0.08
0.10
0.12
RADIAL POSITION (METERS)

then falls off rapidly inside the surface of the ring. Access to the inside of the ring is obtained by insertion of the probe into a 3/8" hole that is drilled into the ring.

There is an additional discrepancy between the measured equilibrium and that predicted by ideal MHD theory. Numerical solution to the Grad-Shafranov equation for high beta plasmas in the Octupole indicates that both the separatrix and the critical flux surface for MHD stability move closer to the ring as the plasma beta is increased (Fig. 15). The position of ψ_{sep} moves from 5.0 cm to 3.4 cm from the ring as β increases from zero to 30%. Over the same range of β, ψ_{crit} moves from 9.3 cm to 6.7 cm. Thus, the radial pressure profile for the β=34% plasma (Fig. 11) should be much narrower than is observed with its peak near 3.4 cm and its edge near 7 cm. This is not observed. Moreover, the fluctuation level at 7 cm ($\delta I/I$ measured with a Langmuir probe) is less than 25% when the plasma beta is high, whereas fluctuation levels of 50-80% are typically observed outside of ψ_{crit}. In addition, the time decay of the ion saturation current at 7 cm and 8 cm do not resemble typical time decays for positions outside of ψ_{crit} (Fig. 16).

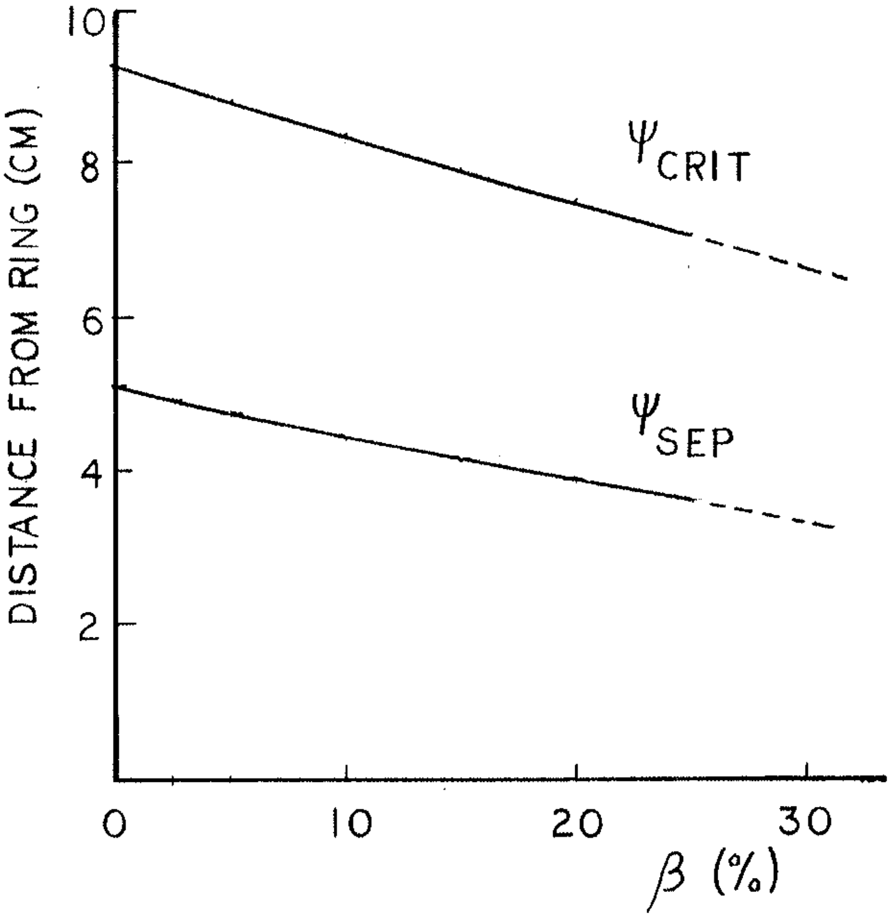

FIG. 15. Position of the critical flux surface and the separatrix in the lower outer bridge versus β. The numerical solution of the Grad-Shafranov equation predicts that both move in toward the ring as β increases.

FIG. 16. Fluctuations in the ion saturation current at three radial positions from the ring surface. Fluctuations outside of ϕ_{crit} typically resemble the 10 cm trace shown here. ϕ_{crit} is located at 9.2 cm with no plasma.

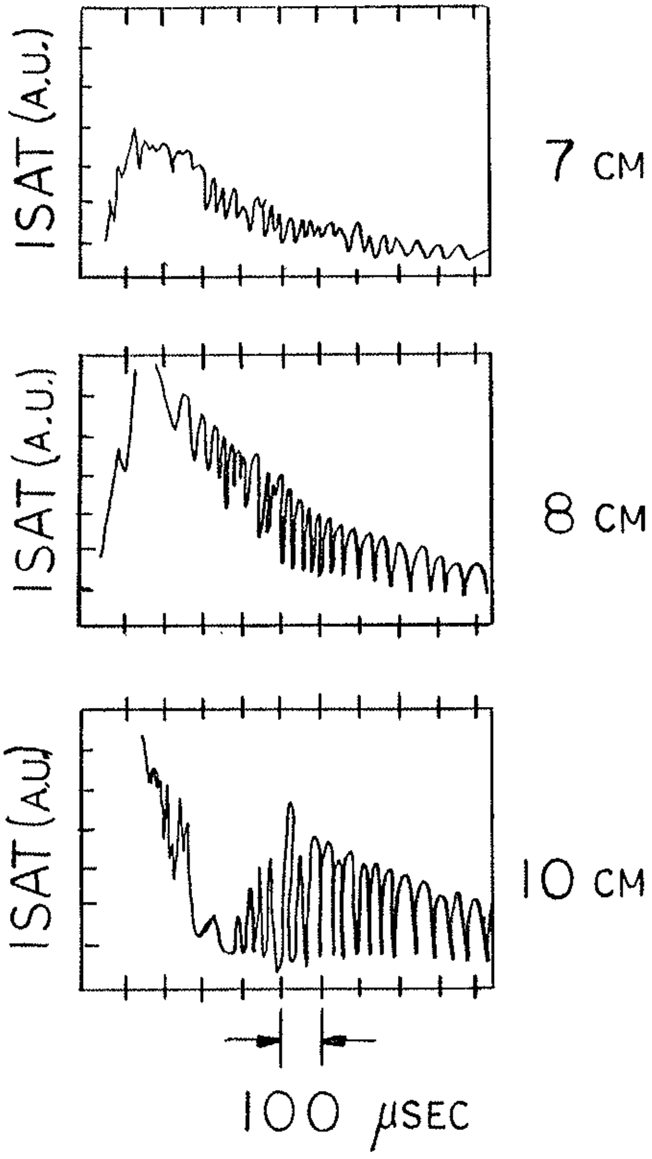
ISAT (A.U.)
7 CM
ISAT (A.U.)
8 CM
ISAT (A.U.)
10 CM
100 μSEC

References for Chapter 4

1. D. Holly, University of Wisconsin-Madison, Ph.D. Thesis (1982).

2. C.M. Fortgang, J.C. Sprott, and E.J. Strait, accepted for publication in Plasma Physics; C.M. Fortgang, University of Wisconsin-Madison, Ph.D. Thesis (1983).

3. R.J. Groebner, University of Wisconsin-Madison, Ph.D. Thesis (1979).

4. G.M. McCracken and P.E. Stott, Nucl. Fusion 19, 889 (1979).

CHAPTER 5

Interpretation of Experimental Results

5.A. Application of Stability Theory

The experimental results make it evident that the ideal MHD ballooning mode theory is not sufficient to explain the stability of these high beta plasmas. As described in the previous section, inclusion of certain kinetic effects can substantially increase plasma stability to ballooning modes. Resistivity is ignorable in all the experimental cases since $S>>1$; also, since the predicted ballooning-mode amplitude varies along the field ($\underline{k}\cdot\underline{B}\neq 0$), which is shearless, special resistive effects such as magnetic reconnection and defeat of shear stabilization play no role. The so-called resistive ballooning mode[1,2] (or resistive interchange) has not been addressed in this work, either experimentally or theoretically. Experimentally, we have searched for a mode that becomes unstable above a critical value of beta (such as the ideal MHD ballooning mode which is localized along a field line), whereas the resistive ballooning mode is unstable at all beta values (and is nearly constant along $\underline{B}$). Although $S>>1$, the growth rates for short toroidal wavelength (high-n) resistive ballooning modes are rapid enough in these low temperature plasmas for these modes to grow in times less than the β-decay time; however, no clear indication of their presence is seen, and if they exist in these plasmas, they are of small amplitude and immersed within the low level fluctuation spectrum ($\tilde{n}/n<5\%$, $\tilde{B}/B<0.5\%$). Trapped particle effects yield a negligible increase in plasma stability as demonstrated by the collisionless energy principle of Kruskal and Oberman (Phillips-Ref.16 Ch.3). The stability of the two cited cases, $\beta=8\%$ and $\beta=35\%$, are attributed to different causes. The $\beta=8\%$ case is explicable by the finite Larmor radius effect which is described in Chapter 3 and enhances the critical β value through coupling of the ballooning mode to an oscillatory ion drift wave. However, this FLR effect is not sufficient to explain stability at $\beta=35\%$. Stability in this case is attributed to the observed reduction in the diamagnetic current, (presumably due to ion gyroviscosity) which, as explained in Chapter 3, is the energy source for the ballooning mode.

For the $\beta=8\%$ case, the requirements are satisfied for the applicability of the kinetic theory described in Section 3F; namely, $\omega/\omega_{ci}<<1$, $\rho_i/L_B<<1$ and $\rho_i/L_p<<1$ where the wave frequency $\omega\simeq\omega_i^*/2\simeq75$ kHz; the ion cyclotron frequency $\omega_{ci}\simeq1.3$ MHz, electron bounce frequency $\omega_{be}\simeq1.7$ MHz, ion bounce frequency $\omega_{b_i}\simeq40$ kHz, ion gyroradius$\simeq0.5$ cm, magnetic gradient scale length $L_B\simeq15$ cm, and pressure gradient scale length $L_p\simeq2.5$ cm. The theory predicts that for the given profile shape, for $\rho_i/L_p\simeq0.2$, the critical beta for instability increases to $\beta_c=10\%$ (Fig. 1). Thus, the $\beta=8\%$ plasma described above should be stable, and this is in agreement with the

FIG. 1. Comparison of stability theory and experiment. The solid line is the finite gyroradius kinetic theory prediction for the critical β versus ρ_i/L_p, where ρ_i/L_p is the ion gyroradius normalized to pressure gradient scale length. The dashed line is the gyroradius independent ideal MHD prediction for β_c. Stable experimental plasmas (including the β=8% and 35% cases) are shown for comparison.

PREDICTED STABILITY REGION FOR BALLOONING MODES IN OCTUPOLE

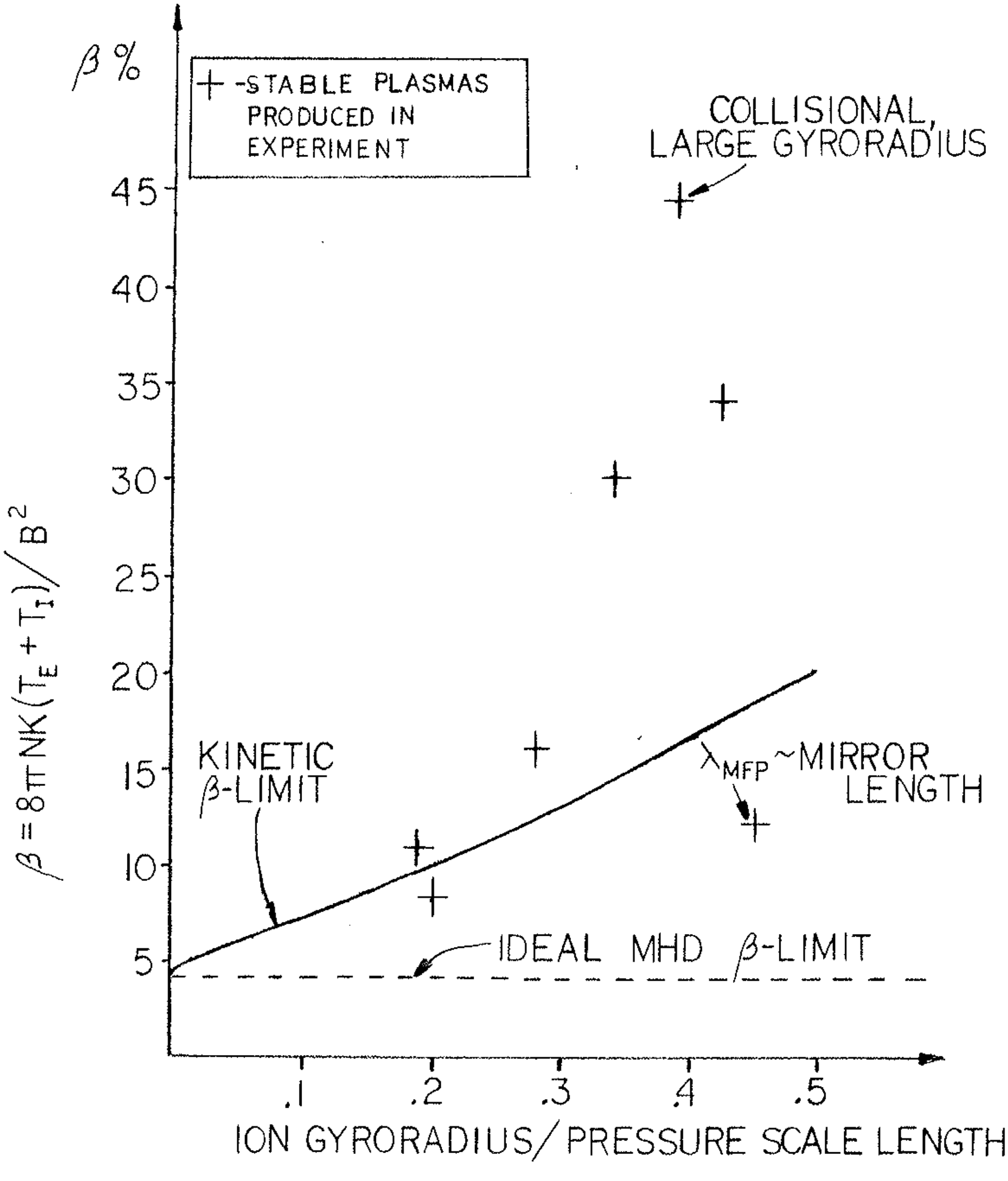

experimental observation. Within experimental uncertainty, the β=11% plasma (ρ_i/L_p=0.19) may also be stabilized solely due to this FLR effect. Additional stabilizing forces may be present, however, because there is no indication that either the β=8% or 11% plasmas are limited by instability, but rather a limitation of the plasma sources available.

At the lower magnetic field (B_p=200 G), β=35% plasma, the gyroradius increases to ρ_i/L_p=0.42. The kinetic theory requirements on the gyroradius, density and magnetic scale length, and bounce frequencies are satisfied for this plasma as for the β=8% plasma. The FLR effects increase the critical beta significantly to 17%. However, this is still a factor of two below the observed value. Comparison of the experimentally measured ΔB with that predicted by ideal MHD for this profile shape and beta reveals that the measured value is a factor of five too small, whereas, for the smaller gyroradius β=8% plasma, agreement with theory is very good (Section 4E). For this plasma, the role of collisional gyroviscosity must be considered.

5.B. Role of Gyroviscosity

A calculation of the effect of gyroviscosity on ballooning stability is outside the scope of this work; however, the role of gyroviscosity in explaining the experimental deviation from single fluid equilibrium can be examined, and this may give some insight into its effect on stability.

To investigate the equilibrium, the region between the ring and wall is modeled by an infinite straight plasma annulus bounded by two coaxial cylinders, representing a ring and the wall. This model accurately describes the corresponding octupole region; the analytical single-fluid coaxial solution is nearly identical to the exact solution of the two-dimensional Grad Shafranov equation for the Octupole. Gyroviscosity is included through the two-fluid equilibrium equations[3]

$$n_\alpha m_\alpha \frac{d\underline{V}_\alpha}{dt} = n_\alpha q_\alpha(\underline{E}+\underline{V}\times\underline{B}) - \nabla p_\alpha - \nabla \cdot \underline{\underline{\pi}}_\alpha + \underline{R}_\alpha \qquad (1)$$

where p_α is the scalar pressure, $\underline{\underline{\pi}}$ is the stress tensor, and $\underline{R}_\alpha$ is the friction force between ion and electrons. If we neglect electron viscosities which are smaller by the mass ratio, Eq. (1) becomes

$$nMv_{ir}v_{ir}' = neE_r - nev_{iz}B - p' - mn(v_{ir}-v_{er})\nu_{ei}$$

$$+ \frac{1}{r}\left\{\frac{2rp\tau}{1+4\omega^2\tau^2}\left[\frac{2}{3}(1+\omega^2\tau^2)v_{ir}' - \omega\tau v_{iz}'\right]\right\}' \qquad (2)$$

$$nMv_{ir}v_{iz}' = neE_z + nev_{ir}B - mn(v_{iz}-v_{ez})\nu_{ei}$$

$$+\frac{1}{r}\left[\frac{2rp\tau}{1+4\omega^2\tau^2}\left(\frac{1}{2}\ v_{iz}+\omega\tau v'_{ir}\right)\right]' \qquad (3)$$

$$nmv_{er}v'_{er} = -neE_r + nev_{ez}B - p' + mn(v_{ir}-v_{er})\nu_{ei} \qquad (4)$$

$$nmv_{er}\nu_{ez}' = -neE_z - ne\nu_{er}B + mn(\nu_{iz}-\nu_{ez})\nu_{ei} \qquad (5)$$

where $'=\partial/\partial r$, and v_{ir}, v_{er}, v_{iz}, v_{ez}, ω, and τ are the ion and electron radial and axial velocities, ion cyclotron frequency, and ion-ion collision time, respectively. Although electron viscous terms are absent, the electron velocity can deviate from its single fluid value since electrons collisionally and electrostatically couple to ions.

Assuming radial velocities on the order of the collisional diffusion velocity, the ion viscous terms are of comparable magnitude to the other terms for the β=35% plasma. For $\omega\tau>1$, the relative magnitude of the viscosity increases as $(\rho_i/L_p)^2$, indicating a large effect as gyroradius increases. With the assumed ordering, terms containing v_{ir} and v_{er} are small (except near the edge where p becomes small). Setting $v_{ir}=v_{er}=0$, permits an analytical but qualitative solution for v_{iz}, v_{ez}, E_r, E_z, and consequently, axial (toroidal) current density, j,

$$j = p'/B - C(\omega\tau)'/rB \qquad (6)$$

where C is an integration constant. The last term represents the desired deviation from single fluid theory due to ion gyroviscosity. For $C<0$, this last term diminishes the current density, but maintains the overall shape as observed experimentally.

In any event, reduction of the diamagnetic current, by whatever cause, decreases the energy source for the instability and thus, may account for the enhanced stability of the $\beta=35\%$ plasma.

5.C. Summary and Discussion

Ideal MHD theory predicts that above a critical beta, $\beta_c=4.3\%$ for the Octupole, the plasma becomes unstable to an ideal ballooning mode. Experimentally, a wide range of MHD stable plasmas has been created with beta significantly above this ideal MHD stability limit. A kinetic treatment reveals that the ballooning mode couples to a electromagnetic drift wave ($\omega \sim \omega_i^*/2$) due to the inclusion of a finite ion gyroradius effect whereupon it becomes oscillatory and stable. The importance of this effect on the stability of the ballooning mode increases as the ratio of the gyroradius to pressure gradient scale length increases. For a $\beta=8\%$ plasma, (twice the ideal limit) with $\rho_i/L_p \sim 0.2$, this effect is sufficient to explain the plasma stability. For a $\beta=35\%$ plasma with $\rho_i/L_p \sim 0.42$, the effect is not large enough to explain the stability. In this plasma, the diamagnetic current is much smaller than predicted for an ideal MHD equilibrium, which may be due to ion gyroviscosity. The enhanced stability can be understood as a combination of the reduced driving force (i.e., diamagnetic current) for the instability and the collisionless FLR effect examined in detail in Chapter 3.

In current tokamaks and proposed reactor-size tokamak experiments, the magnetic field is large and ρ_i/L_p is small. While the stability may not be influenced by the gyroradius size of the bulk plasma, the beta limit may be enhanced significantly due to the large gyroradius of unthermalized neutral beam particles. Since the total plasma beta is the combination of the pressure of both the bulk plasma and the beam component, the predicted beta limit should include any stabilizing FLR effects due to the beam. This is true, not only for beam particles, but for minority species and impurity ions with large gyroradii that may also affect the overall plasma stability. This would be particularly important in inherently low magnetic field devices such as reverse field pinches, spheromaks, and field reversed mirrors.

The effect of ion gyroviscosity may also increase the stability to ballooning modes in other plasma experiments, since for the simple model considered above, if $\omega_{ci}\tau_{ii}>1$, the viscous terms that remain scale as $(\rho_i/L_p)^2$. Thus, for the above situations this effect should also be included in calculations of beta limits.

References for Chapter 5

1. R.M. Kulsrud, *Plasma Physics and Controlled Nuclear Fusion Research*, 1965 (International Atomic Energy Agency, Vienna, 1966), Vol. 1, p. 127.

2. G. Bateman and D.B. Nelson, Phys. Rev. Lett. 41, 1804 (1978).

3. S.I. Braginskii, in *Reviews of Plasma Physics*, edited by M.A. Leontovich (Consultants Bureau, N.Y., 1965), Vol. I, p. 205; S. Chapman and T.G. Cowling, *The Mathematical Theory of Nonuniform Gases* (Cambridge Univ. Press, Cambridge, 1961).

CHAPTER 6

Particle Transport and Fluctuations

This chapter will present the results of a study of particle transport and fluctuations in high density, high beta plasmas. Previous experimental work[1-5] on particle transport in the Octupole has examined low β ($\beta<1\%$) and low density plasmas ($n<1\times10^{12}\mathrm{cm}^{-3}$). Garner[6] examined the transport in a high density (1×10^{13} cm^{-3}) low beta plasma and separately in a lower density (6×10^{12} cm^{-3}), high beta ($\beta\sim10\%$) plasma. This work extends the range of densities and β to 6×10^{13} cm^{-3} and 35% respectively, which are obtained over a range of field strengths from 200 G to 2500 G. An examination of density profiles shapes and decay rates and results of a computer model indicate that the diffusion is classical for the lowest field, high beta plasma and is enhanced above the classical rate at higher magnetic fields. The enhanced level of transport is predominantly in the bad curvature region which may also account for the inward motion of the profile which is typically observed at the higher fields.

Fluctuations in density, electrostatic potential, and magnetic field are examined in plasmas with β from 0.1% to 40%. Though fluctuation levels are largest in the bad curvature region, they are not correlated to β and have similar properties over the entire range of β which includes values considerably below the ideal MHD limit. Particle transport induced by the density fluctuations is shown to be too small to account for the enhanced transport observed in the common flux region.

6.A. Particle Diffusion Equation

The derivation of the diffusion equation proceeds from the particle continuity equation

$$\frac{\partial n}{\partial t} + \nabla \cdot \Gamma = 0 \tag{1}$$

where n is the particle density and Γ is the particle flux. Using Fick′s law to relate the local flux with the local density gradient, $\underline{\Gamma}=-D\nabla n$, Eq. (1) can be written as

$$-\frac{1}{J}\frac{\partial}{\partial\psi}(JRBD_{\perp}\nabla_{\perp}n) - \frac{1}{J}\frac{\partial}{\partial\chi}\left(\frac{D_{\parallel}\nabla_{\parallel}n}{B}\right) = -\frac{\partial n}{\partial t} \tag{2}$$

where J is the Jacobian and $D_{\perp}$ and $D_{\parallel}$ are the diffusion coefficients perpendicular and parallel to the magnetic field. Multiplying by J and integrating along a field line eliminates the second term. Substituting $J=C/B^2$, where C is a constant on each flux surface, this can be written as

$$\frac{\partial n}{\partial t} = \frac{1}{V'}\frac{\partial}{\partial\psi}\left[\frac{\partial n}{\partial\psi}\oint R^2 D_{\perp} d\chi\right] , \tag{3}$$

where $V' \equiv \oint \frac{d\ell}{B_p}$ is the differential volume between flux surfaces and it is assumed that the density is constant along a field line so that $\partial n/\partial\psi$ can be taken outside of the integral. The final form for the diffusion equation is given by

$$\frac{\partial n}{\partial t} = \frac{D_o T^\gamma}{V'} \frac{\partial}{\partial\psi}\left[n^\delta \frac{\partial n}{\partial\psi} \oint R^2 B^{\beta+1} d\ell\right] \qquad (4)$$

where we have expressed $D_\perp = D_o n^\delta T^\gamma B^\beta$ and it is assumed that there is no temperature gradient, $\nabla T=0$. This latter assumption is appropriate for the experimental data since the temperature very rapidly adopts a flat profile and the diffusion coefficients that will be examined here have $|\gamma|=1/2$, so small variations in T across the profile are not significant. The integral $I(\psi) \equiv \oint R^2 B^{\beta+1} d\ell$ depends only on the form of the diffusion coefficient and the magnetic geometry of the machine.

In general, $\delta \neq 0$ and this is a non-linear partial differential equation. The properties of this equation, however, have been studied extensively by Berryman and Drake[7]. A key feature is that the equation is separable into a spatial and temporal part. Thus, for a given form of the diffusion coefficient, there is a time independent "normal mode" shape, i.e. at each position across the profile, the decay rate is the same. Greenwood[1] calculated the normal mode profile shapes in the Octupole for different diffusion coefficients. The shapes for different values of δ are shown in

Fig. 1. Thus, by examination of the shape of the density profile, the density scaling of the diffusion coefficient can be determined. Although the shapes are sensitive to the density scaling, they are relatively insensitive to the magnetic field scaling for the diffusion coefficients examined here ($-2 \leqslant \beta \leqslant 0$). Magnetic field scaling can be determined by measurement of the particle flux to a collector mounted on the surface of an internal ring and using the local density gradient to determine the diffusion coefficient. In the present experiment, this cannot be done because the particle collectors on the internal rings have been removed. Instead, comparisons of experimental decay rates at different field strengths are used to examine the magnetic scaling. The forms of some common diffusion coefficients are listed below.

Classical	$D \sim nT^{-1/2}B^{-2}$
Bohm	$\sim TB^{-1}$
Okuda-Dawson[17]	$\sim TB^{1/2}n^{-1/2}$
Kamimura Dawson[22]	$\sim T^{1/2}n^{-1}$
Ion-neutral	$\sim n_o TB^{-2}$

For ion-neutral collision dominated diffusion, n_o is the neutral density.

If the initial profile is not a normal mode shape, Berryman showed that it will relax to the normal mode in a time short compared to the particle confinement time. The full initial value problem can be handled numerically and the results of this are presented in section 6.D.

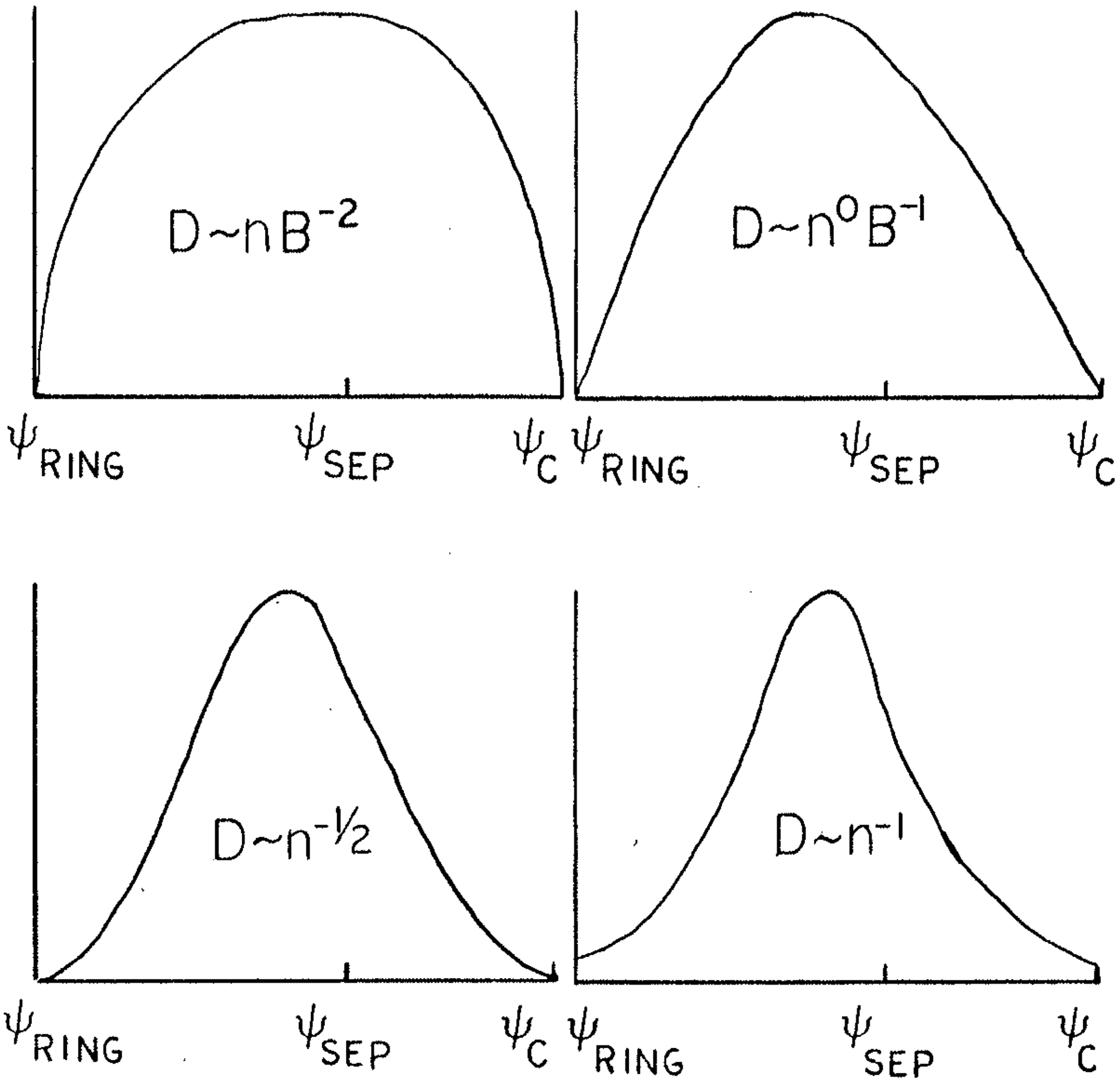

FIG. 1. Normal mode profiles shapes for four different diffusion coefficients. The dominant effect is due to the density dependence.

6.B. Experimental Results

All experimental profiles presented in this section were measured radially across the lower outer bridge between outer ring and outer wall in 1/2 cm to 1 cm intervals. Since the electron and ion temperatures are equal in these high density, low temperature plasmas, the particle density can be obtained by measurement of the ion saturation current. Each point is an average of several shots, and the line averaged interferometer density is used to normalize the shot to shot variations. If either the interferometer or the signal to a reference Langmuir probe is more than 20% from the average value, the shot is discarded. Typical shot to shot variation is only 10% and averaging and normalization generally improves the variability. Large amplitude fluctuations ($\tilde{I}/I>10\%$), generally observed in the common flux region, are smoothed over.

Certain features of the profile shapes are common to many of the plasmas. The initial profile shape, 300 μsec to 400 μsec after injection, is narrow with most of the plasma near the separatrix. Lower field profiles are typically broader than at high field in both the private and common flux regions. The concave up shape ($\partial^2 n/\partial\psi^2>0$) in the private flux at low field quickly ($\tau<\tau_p$) broadens and relaxes to a more time independent shape as is expected for a normal mode (Fig. 2). Although some broadening occurs in the common flux it is not as pronounced since the initial profile shape is not concave as in the private flux. The normal mode shape is relatively

FIG. 2. Density profiles for (a) β=3.5%, (b) β=9.1%, and (c) β=10.2% plasmas at B_p=380 G. Increased density accounts for most of the increase in β.

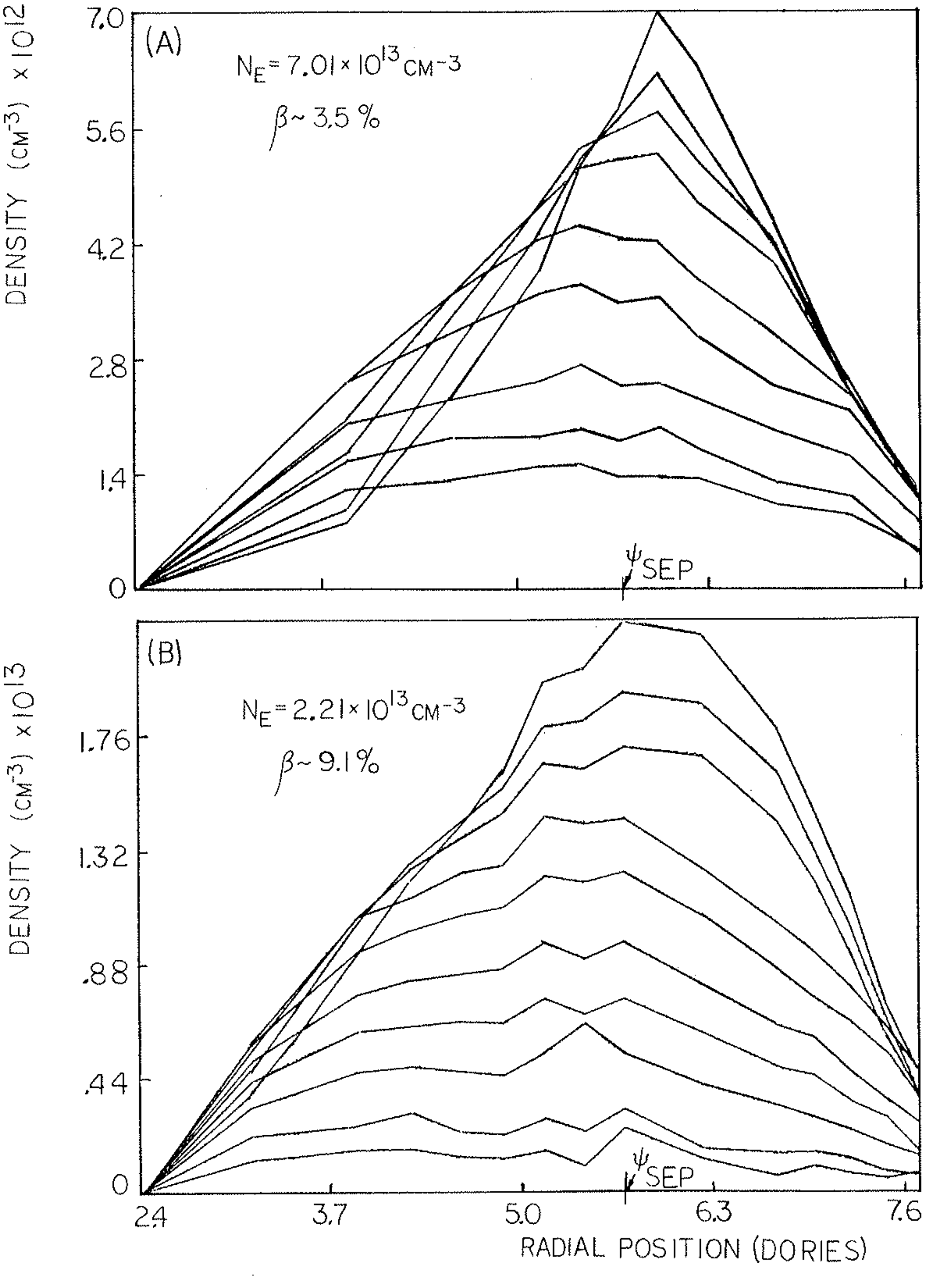
(A)
N_E = 7.01 × 10^13 CM^-3
β ~ 3.5 %
DENSITY (CM^-3) × 10^12
7.0
5.6
4.2
2.8
1.4
0
ψ SEP
(B)
N_E = 2.21 × 10^13 CM^-3
β ~ 9.1%
DENSITY (CM^-3) × 10^13
1.76
1.32
.88
.44
0
ψ SEP
2.4
3.7
5.0
6.3
7.6
RADIAL POSITION (DORIES)

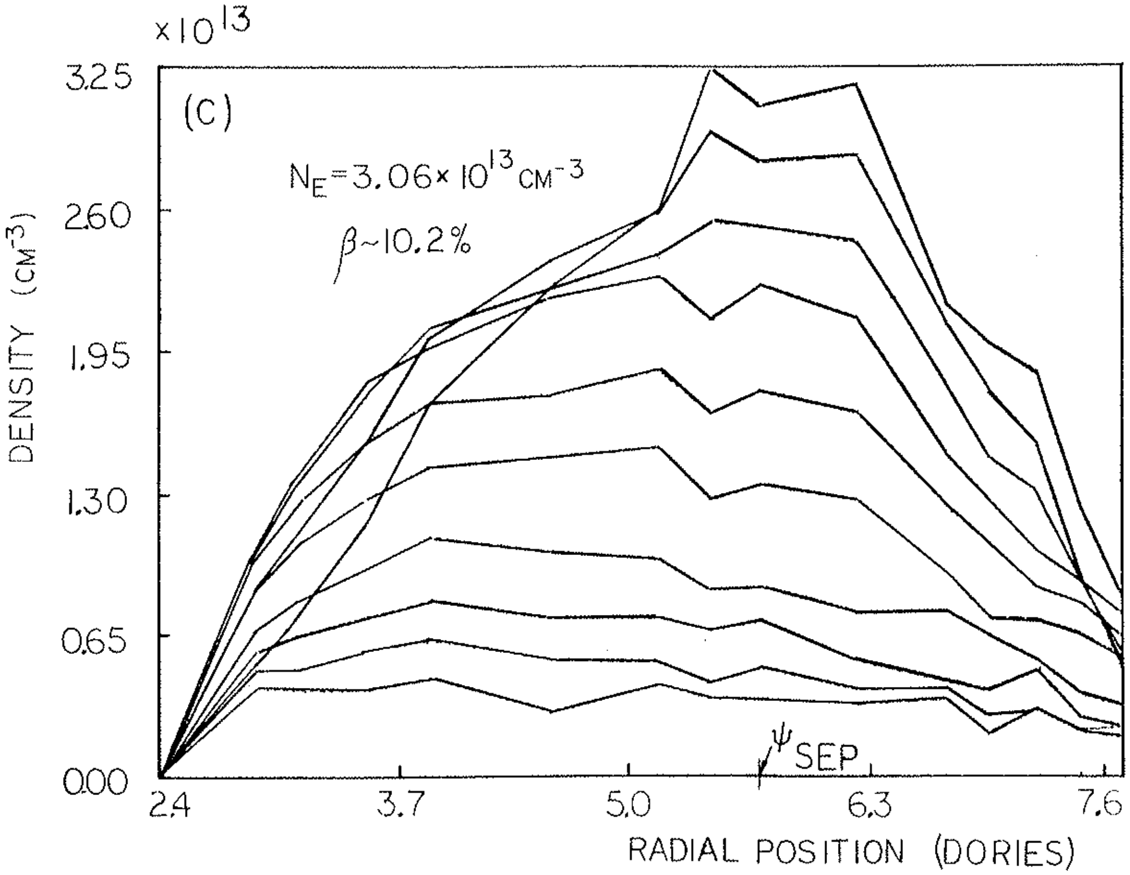
x10^13
3.25
2.60
1.95
1.30
0.65
0.00
DENSITY (CM^-3)
(C)
N_E=3.06×10^13 CM^-3
β~10.2%
ψ SEP
2.4
3.7
5.0
6.3
7.6
RADIAL POSITION (DORIES)

symmetric across the separatrix. For a fixed field strength the profile shape is broader at higher density (Fig. 2).

The broadening of the profile shape in the private flux is also observed at the higher fields (B_p>500 G). The time for relaxation is longer than at low field, but this consistent with a diffusion coefficient that varies with an inverse power of the field strength. The broadening of the profiles from concave to convex shape indicates that the diffusion coefficient is proportional to a positive power of the density.

There are certain differences, however, between the high and low field profiles. At high field, the profiles are not symmetric across the separatrix (Fig. 3). The initial concave shape in the common flux remains concave with the density decreasing everywhere. This profile evolution indicates that the diffusion coefficient (if it is actually a diffusive process) in the common flux is proportional to an inverse power of the density. Moreover, the peak of the profile moves inward toward the ring as the profile evolves. This may indicate a higher level of transport in the common flux than in the private flux. There is some indication of this at intermediate fields (B_p=380 G), however, the asymmetry is most noticeable at the higher fields. This inward motion has been independently verified by measurements of the diamagnetic perturbation to the vacuum magnetic field (ΔB). Measured profiles of ΔB agree with the shape of and position of the peak of

FIG. 3. Density profile at high field (B_p=860 G). The inward motion of the profile and strong asymmetry of the profile across the separatrix is typical of the high field profiles.

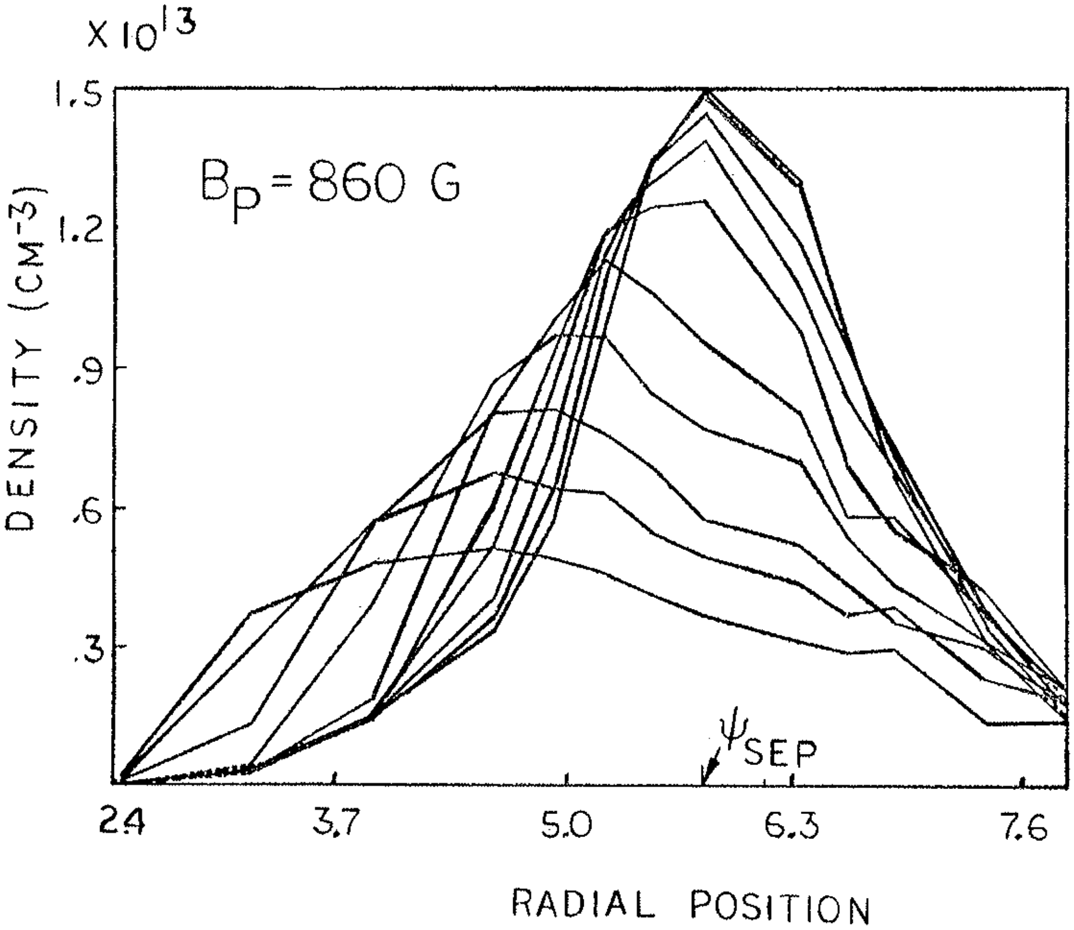
X 10^13
1.5
1.2
.9
.6
.3
DENSITY (CM^-3)
B_P = 860 G
ψ_SEP
2.4
3.7
5.0
6.3
7.6
RADIAL POSITION

theoretical ΔB profiles that use experimental pressure profiles as input.

It is interesting to note that if the density and pressure profiles move in toward the ring so that the pressure peak is inside the separatrix, then the region between the peak and the separatrix is MHD unstable. Fluctuation levels of the ion saturation current for profiles peaked on the separatrix are typically less than 1% in the private flux region up to the separatrix. For these high field cases, however, fluctuations with $\tilde{I}/I \geq 5\%$ are observed on the separatrix and the onset time is within 200 usec after the peak has moved into the private flux. Similar fluctuations are also observed at positions up to 3.5 cm from the ring with onset times that correspond to inward motion of the peak (Fig. 4).

Other investigators have seen "2-region" diffusion before. Drake, et.al.[8] reported Okuda-Dawson diffusion in the private flux and levels enhanced ten times above that in the common flux due to a trapped ion mode. Greenwood[1] reported inward motion of the profile peak in much lower density plasma; however, for that case, the motion was only observed when the rings were levitated. In the present case, levitation of the rings does not change either the evolution of the profiles shape or the decay rate (Fig. 5).

Measurements of the decay times also indicate that the scaling is not classical. Since the classical diffusion coefficient $D \sim nT^{-1/2}B^{-2}$, the confinement time should scale as $\tau \sim L^2/D \sim L^2T^{1/2}B^2/n$ where L is the density scale length. Thus, $n\tau/T^{1/2}$ should be

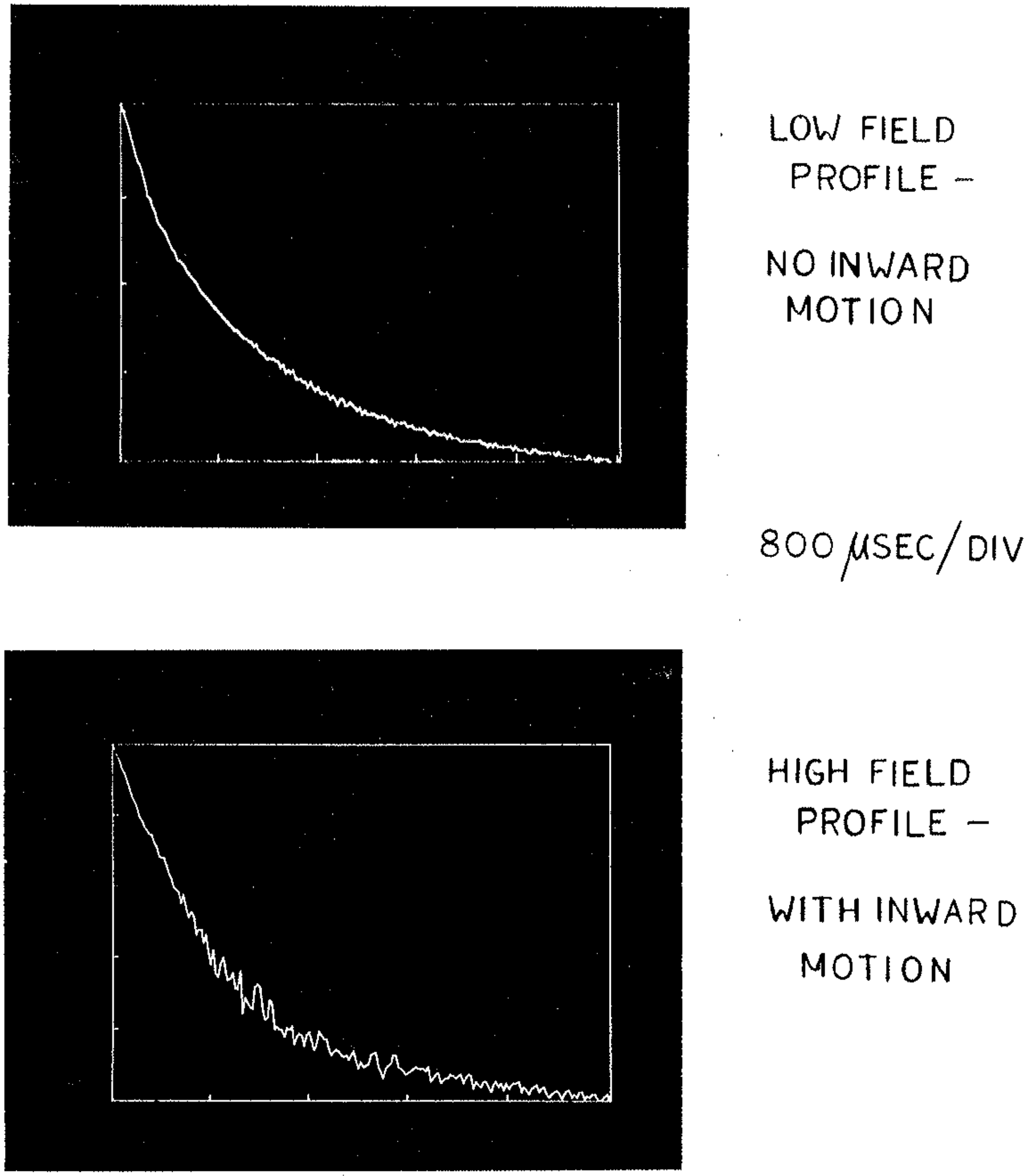

FIG. 4. Ion saturation current on the separatrix in the lower outer bridge for a low and high β profile. Fluctuations are observed in the high field profile associated with the inward motion of the profile.

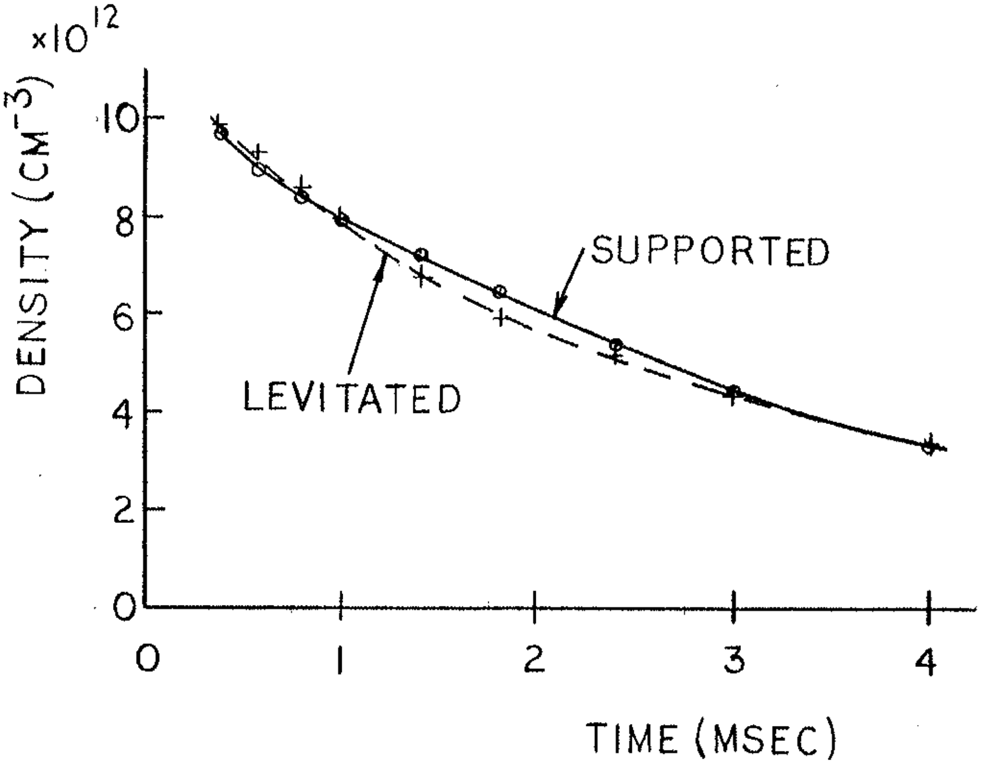

FIG. 5. Comparison of density profiles for cases with the internal rings supported and levitated. (B_p=860 G).

proportional to B^2 for a given profile shape. Fig. 6 is a plot of this quantity as the field was varied from 200 G to 2650 G. Although it increases with magnetic field, the increase is much slower than predicted by classical diffusion. Since the scale length varies only by a factor of two over this range, the effect of profile shape is not enough to bring the classical and experimental decay times into agreement. This is treated more exactly in the following section with the computer model.

6.C. Computer Model

In these high β plasmas, the beta decay time is generally much less than the density decay time because the temperature decays rapidly. Thus, by the time the profiles have relaxed to a normal mode shape, the plasma beta is no longer high. In addition, if the relative amount of different diffusion mechanisms is changing with time, a normal mode shape will not be adopted. In order to treat these problems, a computer program for the octupole diffusion was developed.

The program solves the particle diffusion equation in magnetic flux coordinates (Eq. 4) for the octupole magnetic geometry with magnetic scaling coefficient $\beta=-2,-1$, or 0, density coefficient $\delta>-1$, and any temperature coefficient γ. The treatment of $\delta=-1$ (relevant to Kamimura-Dawson diffusion) is discussed by Berryman and Drake[7] and more recently by Berryman and Holland[9]. The program

FIG. 6. Comparison of experimental density decay time and that predicted by classical scaling. The quantity $n\tau_n/T_e^{1/2}$ should scale as B^2, for similarly shaped profiles, if the diffusion is classical.

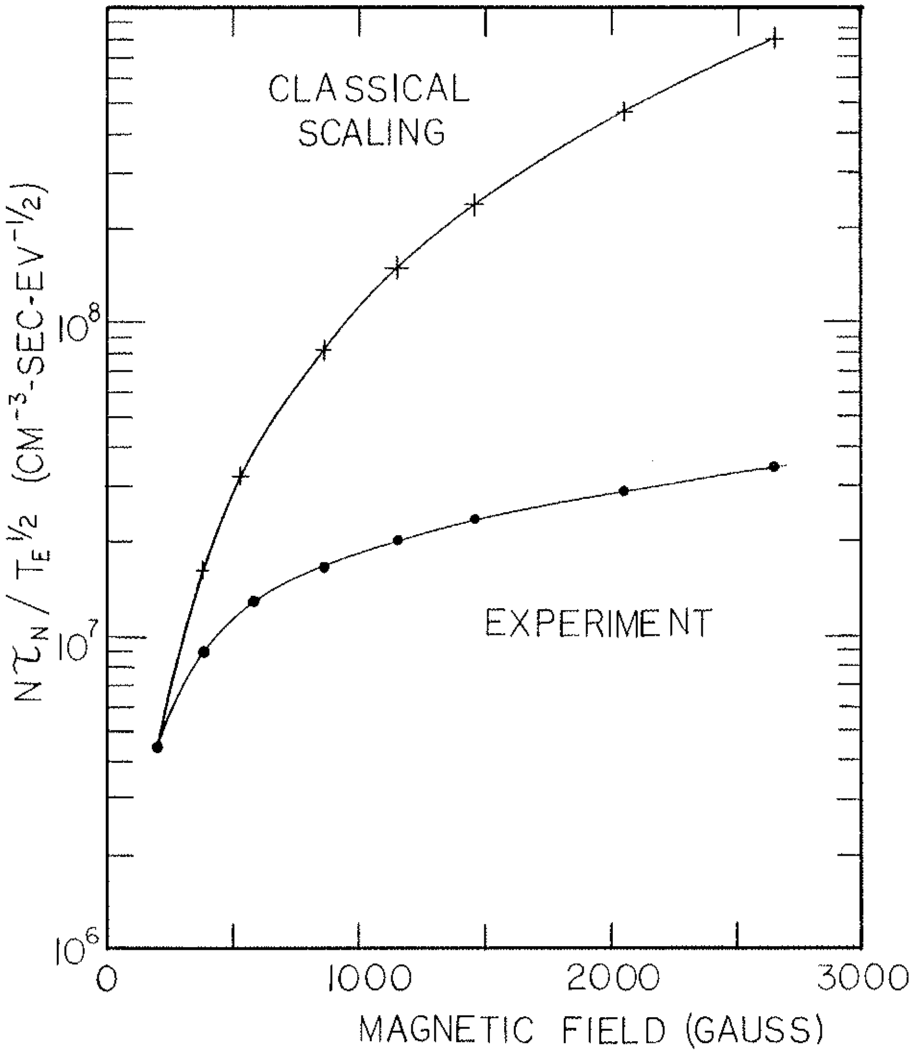
CLASSICAL SCALING
EXPERIMENT
$N\tau_N / T_E^{1/2}$ (CM^{-3}-SEC-EV$^{-1/2}$)
10^6
10^7
10^8
0
1000
2000
3000
MAGNETIC FIELD (GAUSS)

permits any of the above diffusion coefficients to be combined in the form,

$$D = C_1(\phi)D_1 + C_2(\phi)D_2e^{-\lambda t}$$

which enables the 2-region diffusion problem to be treated as well as the damping of one of the diffusion mechanisms.

Eq. (4) is a parabolic equation which is solved as an initial-boundary value problem, i.e. the initial density profile and the boundary conditions for all times are required input. The boundaries of the profile are the surface of the internal ring and the critical flux surface. The measured time dependence of the electron temperature and magnetic field strength are also required in order to evaluate the transport coefficients.

In order to solve Eq. (4), it is rewritten in the form

$$\frac{\partial n}{\partial t} - \left(\frac{A}{\delta+1}\right)\frac{\partial^2 n^{\delta+1}}{\partial\phi^2} - \left(\frac{B}{\delta+1}\right)\frac{\partial n^{\delta+1}}{\partial\phi} = 0 \qquad (5)$$

where,

$$A = \frac{D_o}{V'(\phi)}T(t)^{\gamma}I(\phi),$$

$$B = \frac{D_o}{V'(\phi)} T(t)^{\gamma} \frac{\partial I(\phi)}{\partial \phi},$$

$$I(\phi) = \oint R^2 B^{\beta+1} d\ell,$$

and V' and D_o are defined in Section 6.A. Eq. (5) is solved numerically by expanding it into a finite-difference equation[10-12]. The differencing scheme chosen is the Crank-Nicholson implicit method. Explicit schemes use the value of the density at a time when it is known to predict the density at the subsequent times. This has the advantage of simplicity, however, the stability of the solution depends on the choice of the time and spatial steps, Δt and $\Delta\phi$. The Crank-Nicholson scheme is stable for any choice of Δt and $\Delta\phi$. The 6 point differencing scheme is shown in Fig. 7. The index, n, represents the time steps and j is the spatial position. If the density is known at time n, the spatial derivatives at position j are evaluated at a time $(n + (1-\Theta))$, where Θ is between zero and one, by appropriately weighting the derivatives at step n and n+1. Thus, the density at time n and position j is given in terms of other unknown densities at that time. The Crank-Nicholson differencing scheme with $\Theta=1/2$ was chosen not only for its stability properties, but because of its high accuracy and more importantly because it conserves particles which is essential for a particle

CRANK-NICHOLSON 6-POINT CENTRAL DIFFERENCING SCHEME

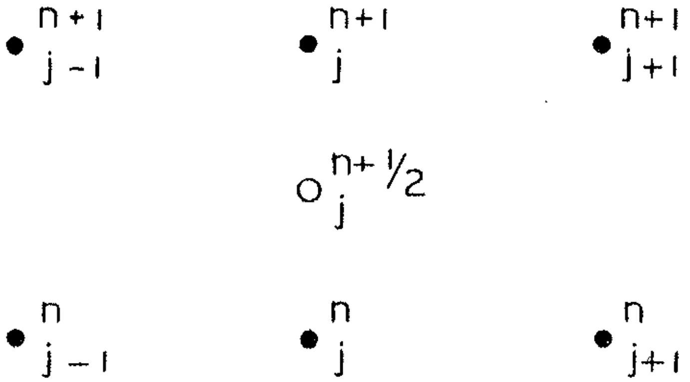

$$\left.\frac{df}{d\phi}\right|_j^{n+\frac{1}{2}} = \frac{1}{2}\left(\frac{f_{j+1}^{n+1} - f_{j-1}^{n+1}}{2\Delta\phi} + \frac{f_{j+1}^{n} - f_{j-1}^{n}}{2\Delta\phi}\right)$$

$$\left.\frac{d^2f}{d\phi^2}\right|_j^{n+\frac{1}{2}} = \frac{1}{2}\left(\frac{f_{j+1}^{n+1} - 2f_{j}^{n+1} + f_{j-1}^{n+1}}{(\Delta\phi)^2} + \frac{f_{j+1}^{n} - 2f_{j}^{n} + f_{j-1}^{n}}{(\Delta\phi)^2}\right)$$

$$\left.\frac{df}{dt}\right|_j^{n+\frac{1}{2}} = \frac{f_{j}^{n+1} - f_{j}^{n}}{\Delta t}$$

FIG. 7. Crank-Nicholson differencing scheme used for writing the diffusion equation as a finite-difference equation.

transport code[13]. The scheme is accurate to second order in both Δt and $\Delta\phi$.

The non-linearity is handled by the expansion of the non-linear term[10]:

$$(f^{\delta+1})_j^{n+1} = (f^{\delta+1})_j^n + (\delta+1)(f^{\delta})_j^n(f_j^{n+1}-f_j^n).(6)$$

In this way, the nonlinearity has been transferred to a time when the function is known. The solutions are obtained for the transformed variable $w_j^{n+1} = f_j^{n+1}-f_j^n$.

This differencing method results in a system of j-2 equations and j-2 unknowns where j is the number of spatial grid positions. The density at the end points is specified as a boundary condition. Each equation contains only three unknowns which results in a tridiagonal matrix. The system of equations is solved iteratively using a Generalized Newton's Method with an initial guess of $w_j=0$. Iterations are continued until the relative difference between successive solutions is less than 5×10^{-5}. Once a normal mode is reached, the number of iterations required per time step is generally only five or six. Typical time steps chosen are 2-10 μsec with the shorter time step used for the larger values of the diffusion coefficient. If the time step is varied, the solution can be seen to converge to a value that is within 0.3% of the solution that is presented here. Similar behavior is seen with variation in the spatial step. The actual step size used for these results was

$\Delta\psi=0.2$ Dories which results in 29 spatial positions between the ring and ψ_{crit}. The boundary condition chosen is small, but non-zero, to permit treatment of $\delta<0$, and is also independent of time. The actual boundary value used is $n=5\times10^{10}$ cm^{-3} which is smaller than any densities in the region of interest. Varying the edge density from 5×10^{9} to 2×10^{12} cm^{-3} has a negligible effect on the density decay rate and on the density more than one spatial step from the boundary.

6.D. Results of Computer Model

The results presented in this section are comparisons of experimental profiles and decay rates with those predicted by the model for various diffusion coefficients.

6.D.1. Classical

The first diffusion mechanism examined is classical diffusion. Comparison of the classical decay time, τ_{cl}, to the experimental decay time, τ_{exp} indicates that the enhancement over classical increases with increasing field strength. This is qualitatively the same result as in the rough scaling presented in Section 6.B. The average enhancement ranges from 1.5 at B_p=200 G to 3.0 at B_p=860 G. There are some high field cases (B_p=540 G and 860 G) where the enhancement is considerably larger (up to 13 × classical), however, the trend with magnetic field is clear. Speculation on these anomalously high cases will be discussed later.

There does not seem to be any clear dependence of τ_{cl}/τ_{exp} on plasma density. At a density of 2.25×10^{13} cm$^{-3}\pm0.2\times10^{13}$ cm^{-3}, the enhancement varies from 1.0 to 6.7, while at a constant field strength of 380 G, $\tau_{cl}/\tau_{exp}=2.05\pm.30$ over a density variation of more than a factor of seven.

There is also no indication of any direct dependence of the enhancement on the plasma beta (Fig. 8). It can be seen that at $\beta\sim11\%$, the enhancement varies as much as a factor of six, from 2.2 to 13.0. Of particular interest is that for the highest beta profile measured, the decay rate agrees with classical. Figure 9 shows the comparison between the experimental density decay and profile shape and those predicted by the model. The agreement for both is very good and the conclusion is that the diffusion in this high β, low field plasma is classical.

Even at this lowest field, however, the lower density profiles do not match classical diffusion. The results are similar at slightly higher field ($B_p=380$ G); the lower density profiles are not as convex as classical predicts but rather are more angular. It is only at the highest density profile at this field ($n_e\sim3.1\times10^{13}$ cm^{-3}, Fig. 2c) that the curvature approaches classical.

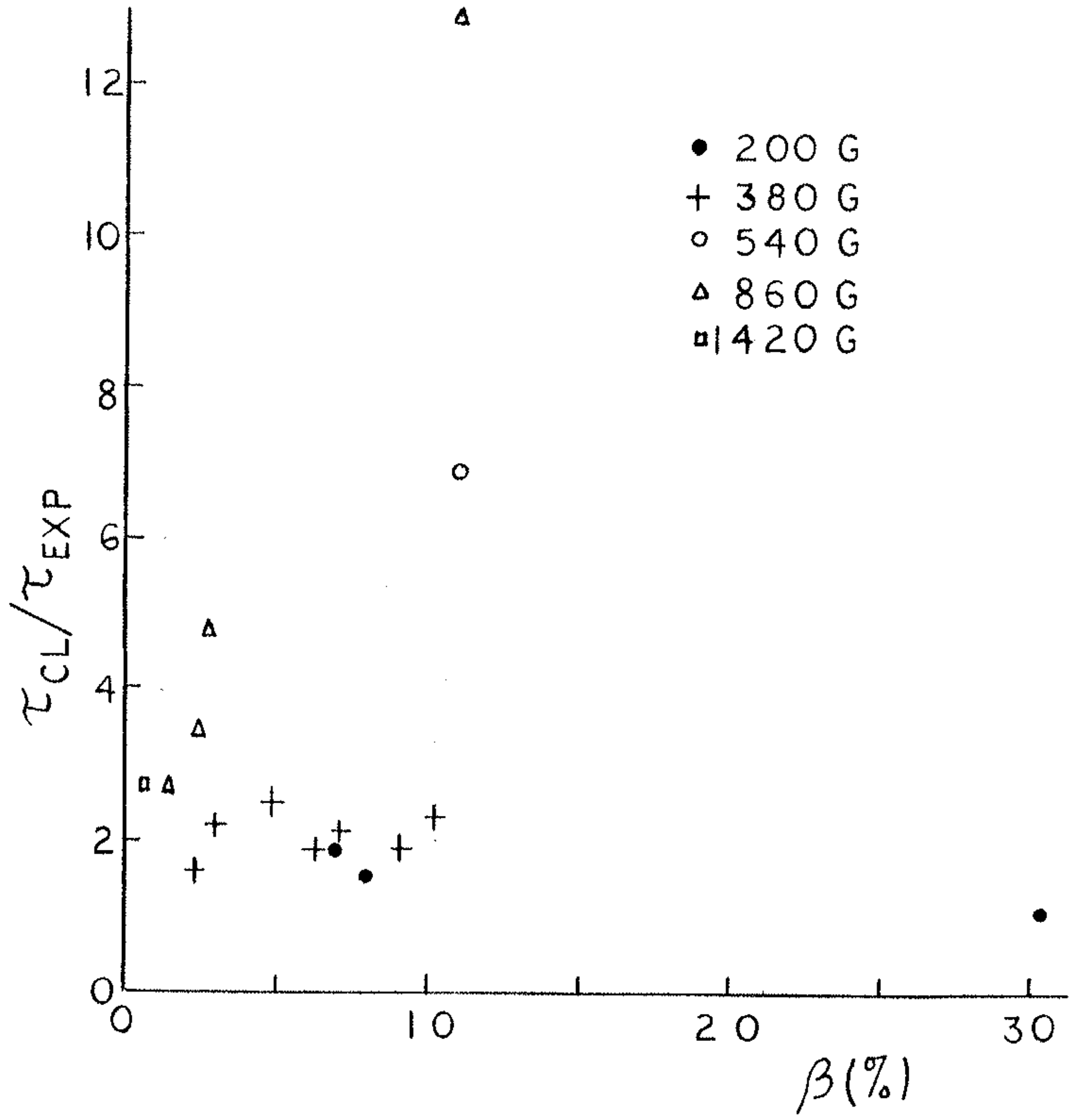

FIG. 8. Ratio of classical density decay time to experimental decay time (τ_{cl}/τ_{exp}) versus β. No dependence on β is observed.

FIG. 9. Comparison of experimental density decay and profile shape with those predicted by the model for classical diffusion. $\beta \sim 30\%$ at $t=400$ μsec with $B_p=200$ G.

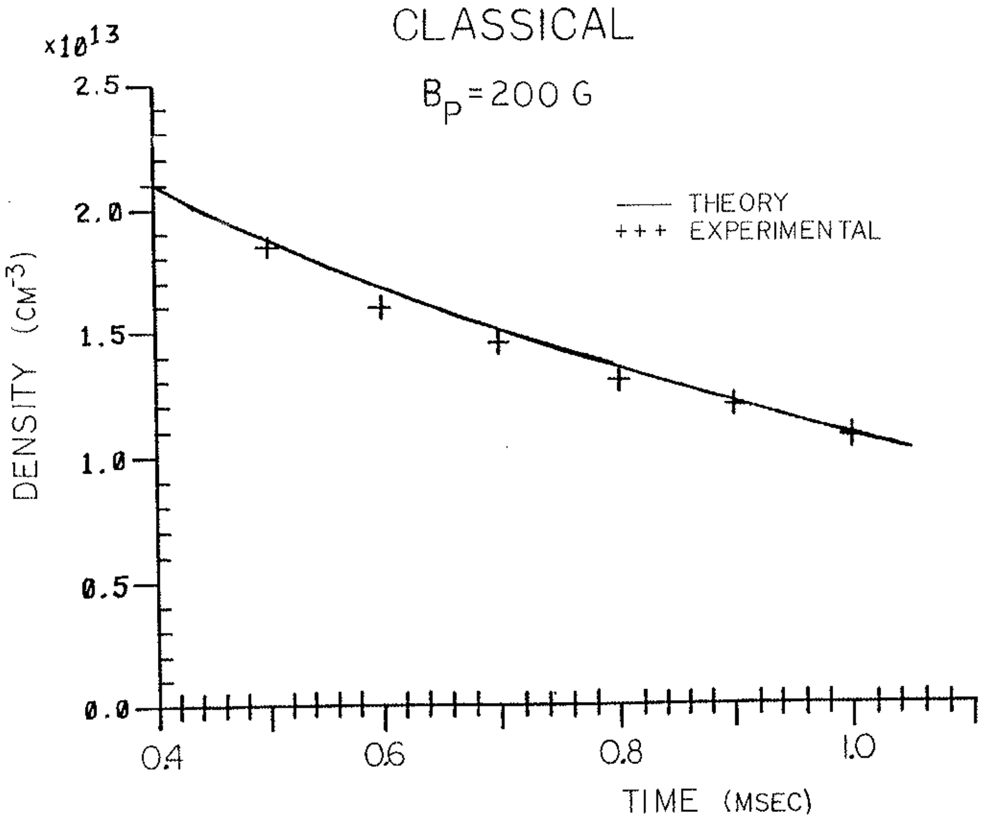
CLASSICAL
B_P = 200 G
x10^13
2.5
2.0
1.5
1.0
0.5
0.0
DENSITY (CM^-3)
THEORY
+++ EXPERIMENTAL
0.4
0.6
0.8
1.0
TIME (MSEC)

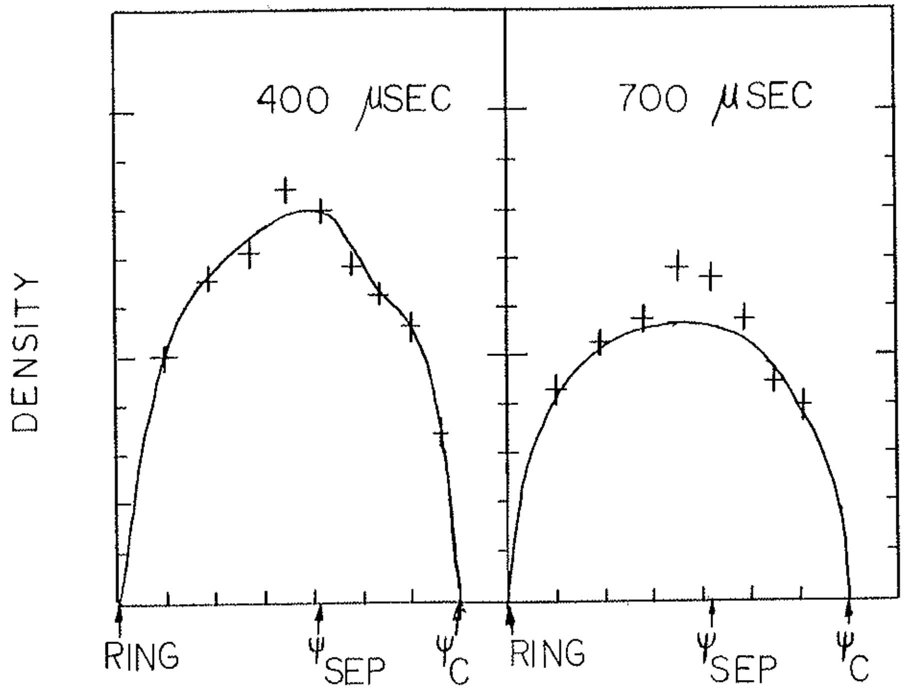
400 μSEC
700 μSEC
DENSITY
RING
ψ_SEP
ψ_C
RING
ψ_SEP
ψ_C

6.D.2. Neutral Dominated Diffusion

All these profiles indicate that if the diffusion is determined by a single coefficient, then $D \sim n^{\delta}$ where $\delta > 0$. Figure 10 shows a particular case where $D \sim n^{1/2}$ gives a reasonable match to the experimental data although the match is not perfect. In particular, however, no single diffusion coefficient is able to match all the profile shapes even at one field setting. Since more angular profiles result from a diffusion coefficient that is independent of the density, it is worth examining the possibility that the diffusion is a combination of classical diffusion ($D \sim n^{1}$) which is due to ion-electron collisions and neutral dominated diffusion ($D \sim n^{0}$) which is due to ion-neutral diffusions. (For the cross-sections used in the following discussion, see Ref. 14 and 15.)

There are problems with this interpretation of the diffusion. First, this does not predict the motion of the peak of the profile. Thus, still another mechanism would need to be postulated to account for that. Although the ion-neutral diffusion coefficient is independent of ion density, it does depend on the neutral density, n_o. Different levels of transport on the inside and outside of the profile are possible if the neutral pressure profile is not the same in both regions and thus, this cannot be ruled out. Triangular profiles will only result if n_o is uniform throughout the machine. This is unlikely since in these high density plasmas the mean free

FIG. 10. Comparison of experimental density decay with the prediction of the model for $D \sim n^{1/2}$ (upper plot). The predicted profile shape (lower plot) has a similar shape to the experimental profile (Fig. 2b).

MODEL → $D_\perp \sim N^{1/2}$

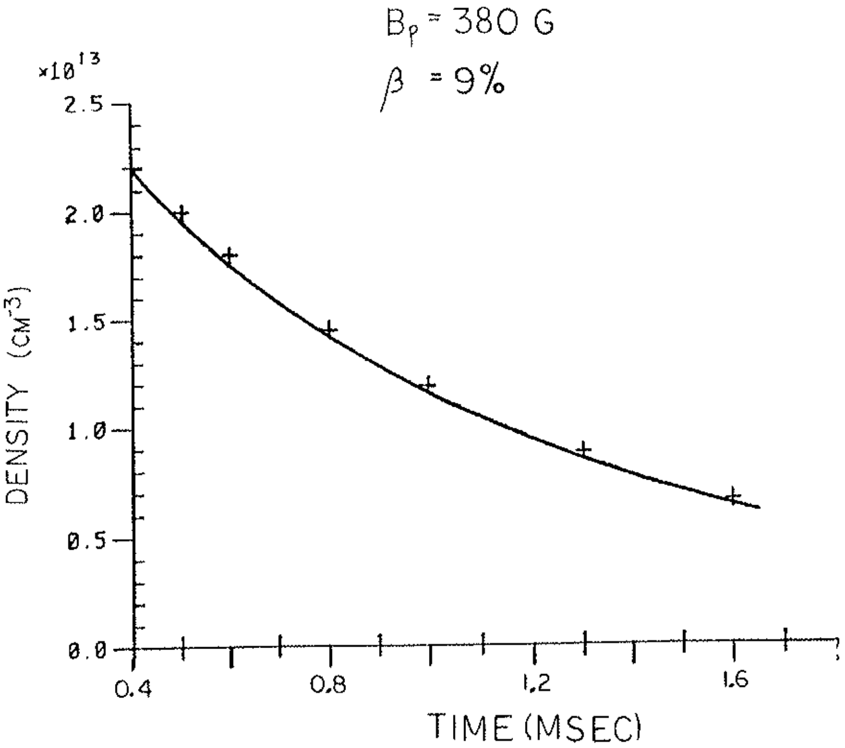

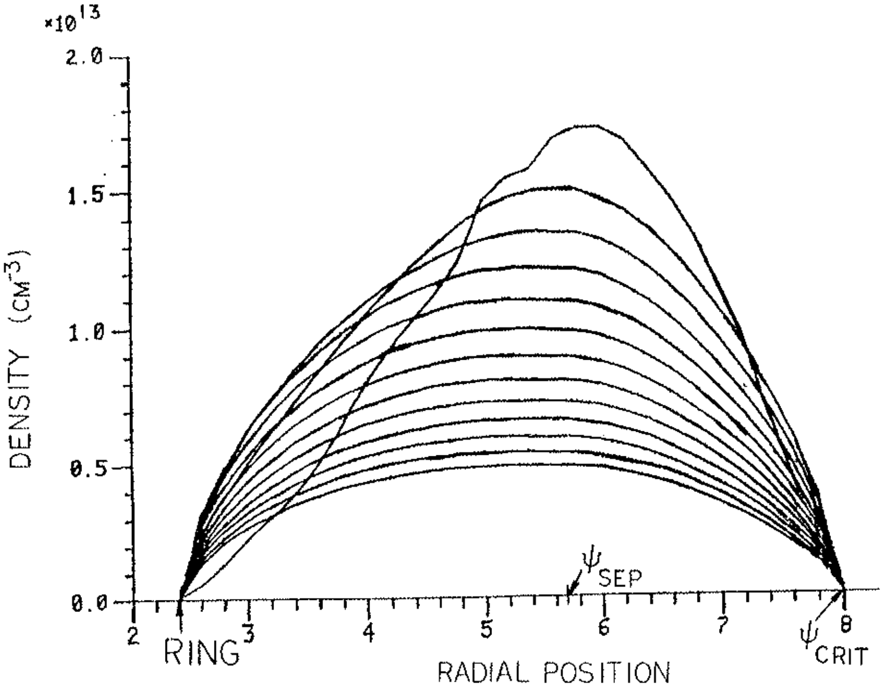

path for ionization is smaller than profile scale lengths. This is particularly true for molecular hydrogen, however, the high energy Frank-Condon neutrals might penetrate to the interior for the lower temperature plasmas. A detailed treatment of the problem is required for each plasma in order to determine the neutral profile, however, there is no apriori reason to expect a flat neutral profile and thus a triangular plasma density profile.

There is a more fundamental problem with ion-neutral dominated diffusion. For the range of plasma parameters in this experiment, the neutral pressure required for ion-neutral diffusion to be comparable with classical diffusion is $n_o \sim 1-4\times10^{-4}$ Torr. Measured edge neutral pressures from a fast ionization gauge are typically in the mid 10^{-5} Torr range during the early part of the shot and are most likely lower in the central plasma region. Moreover, for plasma temperatures above 10 eV, this neutral density would lead to an electron temperature decay time of ~5 μsec due to excitation and ionization[16]. This is inconsistent with the observed decay times of 300-1000 μsec. Even at low $T_e \sim 2.5-5$ eV, where excitation and ionization are drastically reduced, the ion-neutral diffusion coefficient is five to ten times smaller than classical for a neutral density that could lead to the observed electron temperature decays. Thus, it is concluded that the diffusion is not due to ion-neutral collisions.

6.D.3. Vortex (Okuda-Dawson) Diffusion

The theory of vortex diffusion has been treated extensively in the literature[17,18], so details of the theory will not be presented here. An excellent summary of the theory and its relevance to the Octupole is given by Navratil[5]. Basically, this diffusion is due to thermally excited plasma vortices caused by electrostatic convective cells. These cells are created by excess charges on magnetic field lines and they behave like d.c. electric fields. The cell structure damps out on a time scale $\tau \sim (\mu_\perp^i k_\perp^2)^{-1}$, where $\mu_\perp^i = \frac{3}{10}\left(\frac{kT}{m_i}\right)\left(1/\omega_{ci}^2 \tau_{ii}\right)$ is the higher order ion gyroviscosity and $k_\perp = 2\pi/L_\perp$, where $L_\perp$ is the perpendicular scale length of the cell. It can be seen that when the cell size is larger than the ion gyroradius, $k_\perp \rho_i < 1$, then the damping time is larger than ion-ion collision time, and this mechanism can lead to enhanced plasma transport. For high dielectric constant plasmas, such as those in this experiment ($\varepsilon > 10^5$), the form of the resultant diffusion coefficient is $D_{vort} \sim T^{1/2}/n^{1/2}$. Note that this diffusion is field independent, and that it yields concave profile shapes which have been observed in the common flux in the experiment.

Convective cells and the resultant vortex diffusion have been observed on the Octupole in the past[2,3,19]. Particle transport was enhanced above the classical level in a low temperature and density plasma ($n \sim 10^9$ cm^{-3}, $T_e \sim 1.5$ eV) and in a slightly higher density, very collisional plasma ($n \sim 10^{11}$ cm^{-3}, $T_e \sim 0.2$ eV) for fields above

100 G. The current experimental plasmas are collisional and have large gyroradii, and thus the damping times for the convective cells are short. Table 1 is a summary of the damping times in some representative plasmas.

Table 1

n	T	B	τ
2×10^{13} cm^{-3}	10 eV	200 G	85 μsec
2×10^{13}	10 eV	380 G	310 μsec
2×10^{13}	15 eV	540 G	760 μsec
1×10^{13}	20 eV	860 G	4400 μsec

It is clear that the damping time in the lowest field, high β plasma is too short to observe vortex diffusion, however, for the other plasmas, in particular, the high field cases, vortex diffusion should remain long enough to be easily observed. In addition, since the classical contribution scales as B^{-2}, as the field increases the relative contribution of classical to vortex decreases, and the higher fields should more closely resemble vortex, as is observed.

It should be noted that if T is the thermal equilibrium plasma temperature then $D_{vort} \ll D_{class}$. It was shown in previous investigations that non-thermal fluctuations relating to the initial conditions of plasma injection give rise to an effective temperature $T^* \gg T_{thermal}$. $T^* \sim 10^6$ eV was measured in a 10^{11} cm^{-3} plasma[2]. Determining the magnitude of the diffusion coefficient from the decay rate can thus indicate the enhancement above thermal levels.

If the diffusion is modeled by classical enhanced by vortex, the decay rate can be matched; however, comparison of the predicted profile (Fig. 11) with the measured profile (Fig. 2b) indicates that the shape is not correct. In addition, if the enhanced level of diffusion is the same strength in the common and private flux, the inward motion of the profile cannot be matched. This requires an asymmetry in the particle flux between the two regions.

The experimental particle flux can be determined from the observed density profiles by using the continuity equation. If $\langle\Gamma\rangle \equiv \oint R\Gamma_\psi d\ell$, then it is easily shown that

$$\langle\Gamma(\psi)\rangle = \langle\Gamma(\psi_o)\rangle + \frac{1}{2\pi} \oint \frac{\partial n}{\partial t} V' d\psi \quad .$$

Choosing ψ_o at the peak of the profile so that $\Gamma(\psi_o\rangle=0$ (assuming all the flux is diffusion), the flux can be determined at each ψ. The results for a high field profile that moves inward indicate that, as expected, the particle flux on the outside (common flux) is much higher than on the inside (Fig. 12). For comparison, the expected classical flux for this profile is also shown. In the common flux region, the classical and experimental flux disagree in both magnitude and shape, whereas on the inside the agreement is much better. At 1000 μsec, it should be noted that the actual flux is less than classical. This may be due to a misplacement of the baseline for zero flux if there is an error in the location of the

FIG. 11. Comparison of experimental density decay with the prediction of the model for classical diffusion enhanced by vortex diffusion (upper plot). While the decay rates can be made to agree, the predicted profile shape (lower plot) does not match the experiment (Fig. 2b).

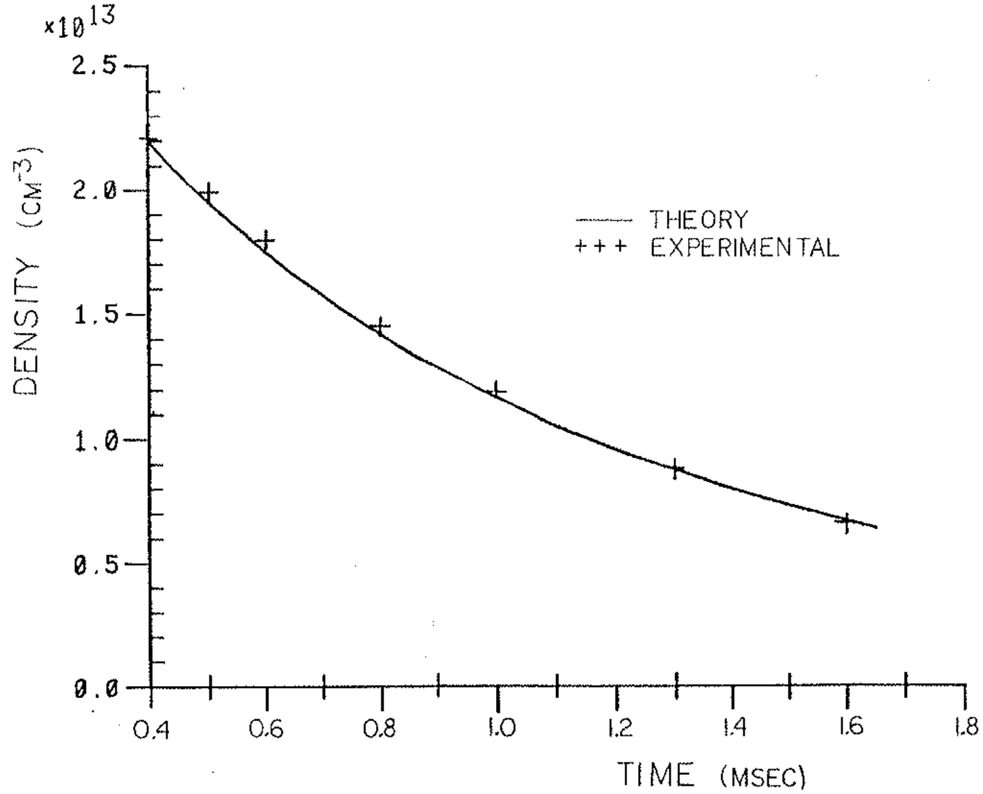

x10^13
2.5
2.0
1.5
1.0
0.5
0.0
DENSITY (CM^-3)
THEORY
+++ EXPERIMENTAL
0.4
0.6
0.8
1.0
1.2
1.4
1.6
1.8
TIME (MSEC)

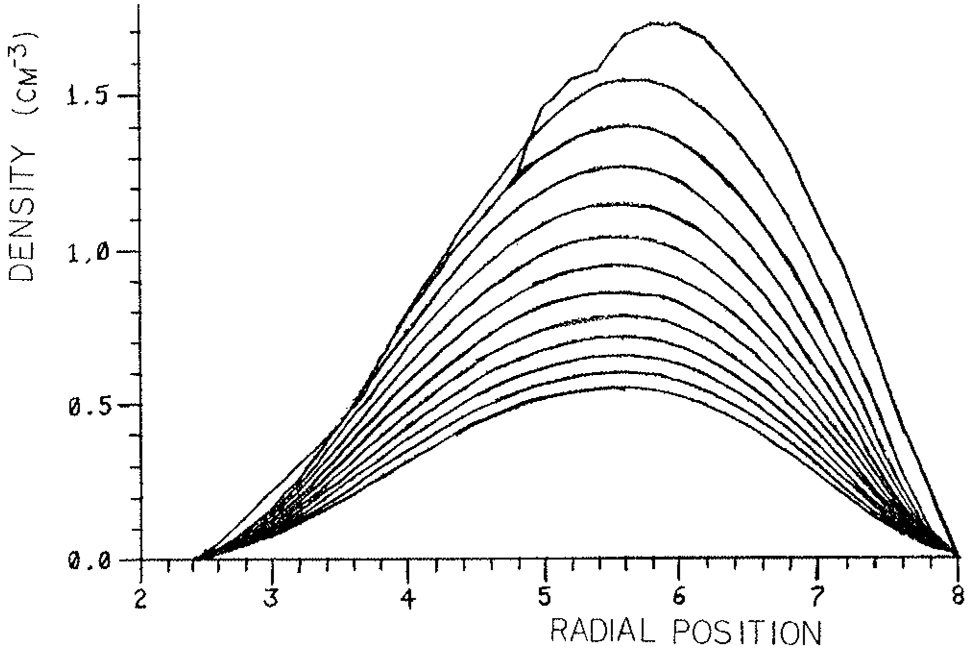

DENSITY (CM^-3)
1.5
1.0
0.5
0.0
2
3
4
5
6
7
8
RADIAL POSITION

FIG. 12. Comparison of experimental particle flux (determined from the measured profile evolution) with classical and vortex flux calculated for the actual profile shapes. (a) t=400 μsec and (b) t=1000 μsec.

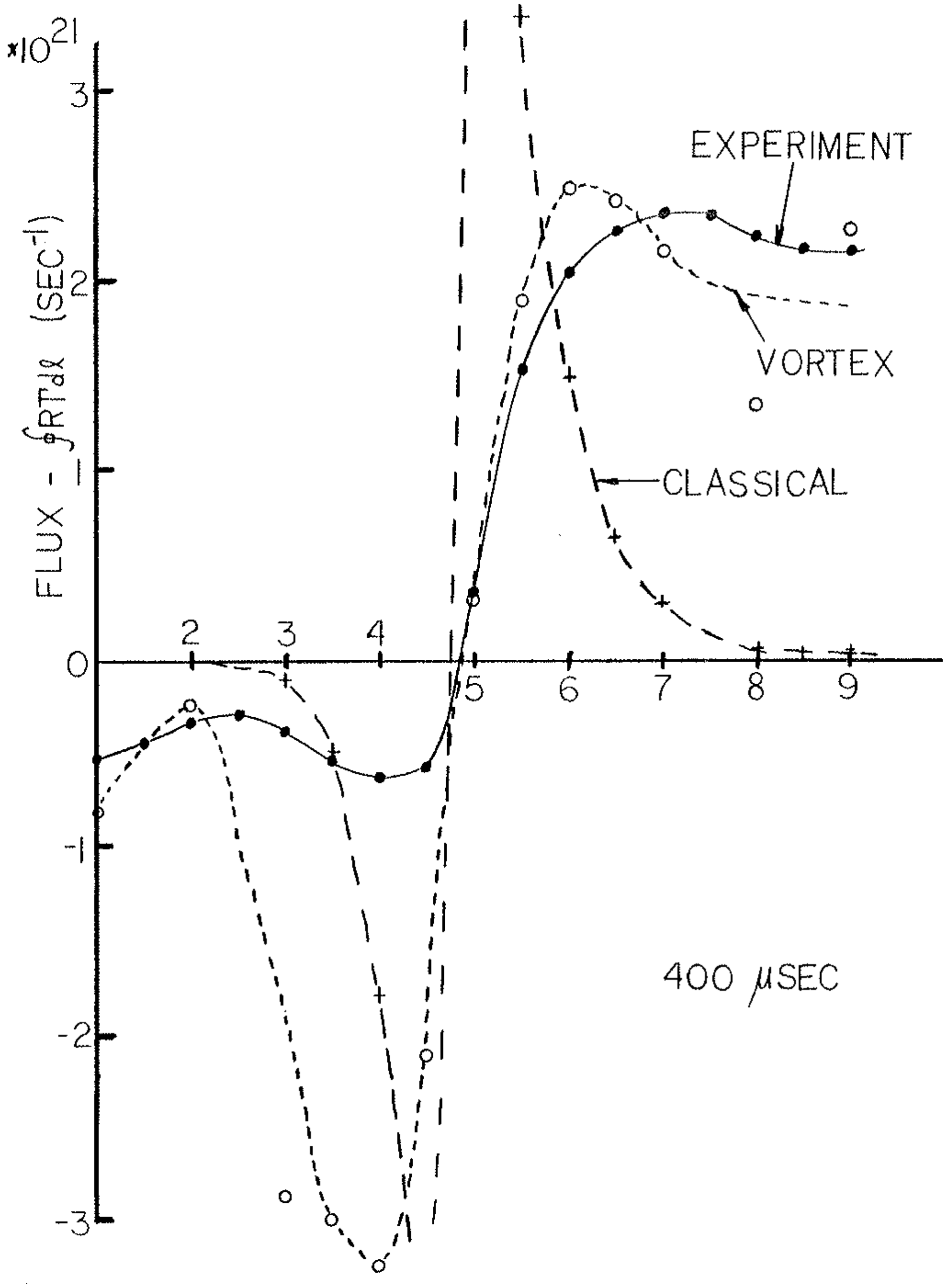
×10^21
FLUX - ∮RTdℓ (SEC^-1)
3
2
1
0
-1
-2
-3
2
3
4
5
6
7
8
9
EXPERIMENT
VORTEX
CLASSICAL
400 μSEC

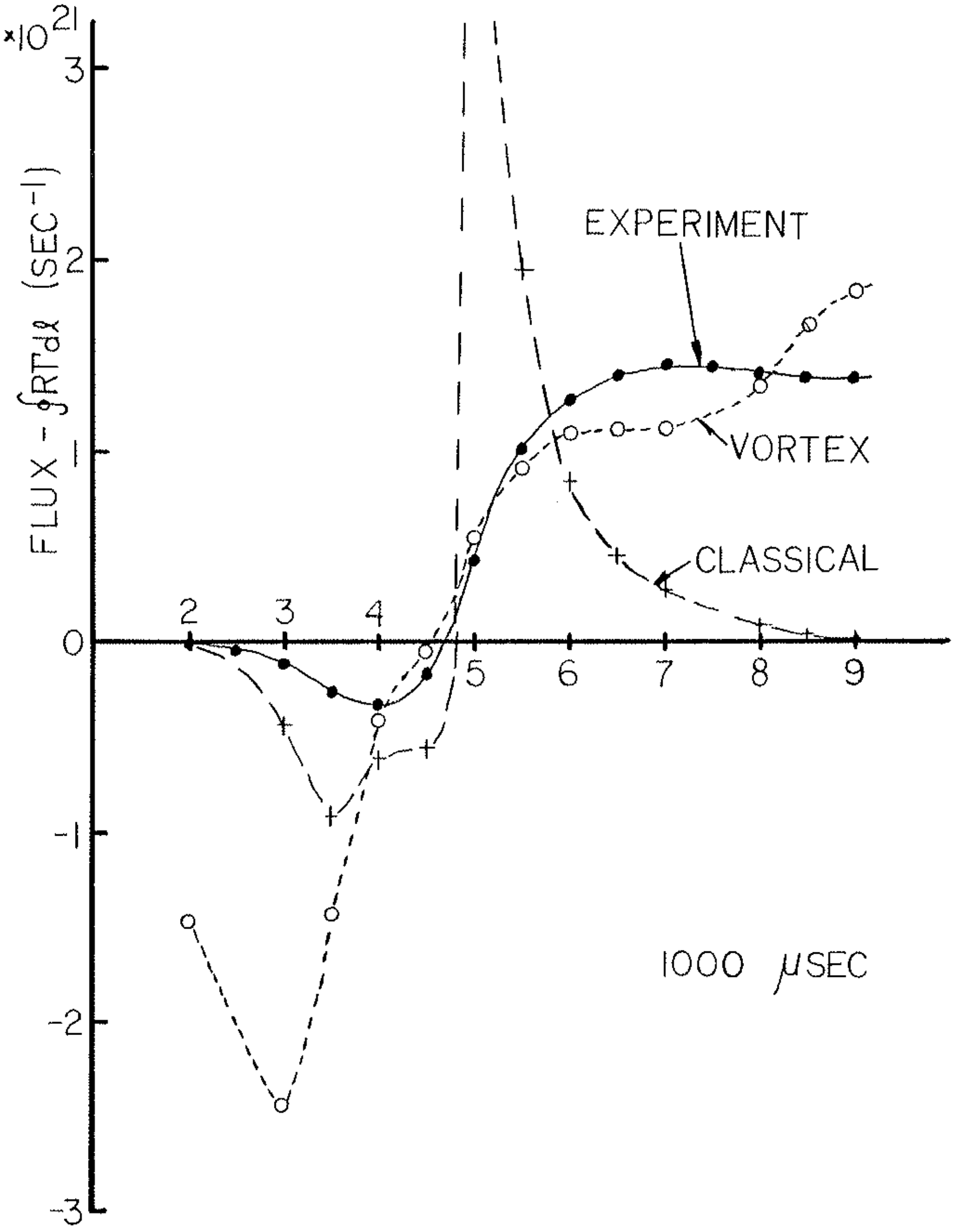
×10^21
3
2
1
0
-1
-2
-3
FLUX - ∮RT dℓ (SEC^-1)
2
3
4
5
6
7
8
9
EXPERIMENT
VORTEX
CLASSICAL
1000 μSEC

profile peak ($\Gamma(\psi_o)=0$), or if there is a small amount of non-diffusive flux near the peak of the profile so that $\Gamma(\psi_{peak})\neq 0$. Alternatively, reflux from the surface of the ring could reduce the net particle flow out of the plasma region.

With this understanding, a good match can be obtained for a $\beta=11\%$ plasma at $B_p=540$ G with classical diffusion on the inside and classical enhanced by vortex on the outside (Fig. 13). The decay time for the vortex diffusion for the best match is 600 μsec which is approximately what is expected due to classical ion viscous damping (line 3, Table 1). In a similar manner, other profile shapes and decay rates for high field plasmas can be matched. In addition, some intermediate field profiles can be matched, in particular, those that exhibit some inward motion.

As mentioned earlier, there are three high field plasmas where the enhancement above classical was considerably larger than the rest. These plasmas were "big gun" plasmas, whereas the other high field cases were intermediate gun plasmas. The magnitude of D indicates that the effective temperature, T*, for the big gun plasmas is the same for most cases studied and is 100 times higher than the intermediate gun plasmas. This is consistent with the interpretation that T* is related to the plasma formation and injection process and thus should be different for the two guns. A higher plasma injection velocity from the big gun would require a larger electric field and polarization charge to allow the plasma to cross field lines. This could account for the higher T* for big gun

FIG. 13. Comparison of experimental and theoretical density decay rate and (b) profile shape (following page) for a $\beta=11\%$ plasma with the inward motion observed ($B_p=540$ G).

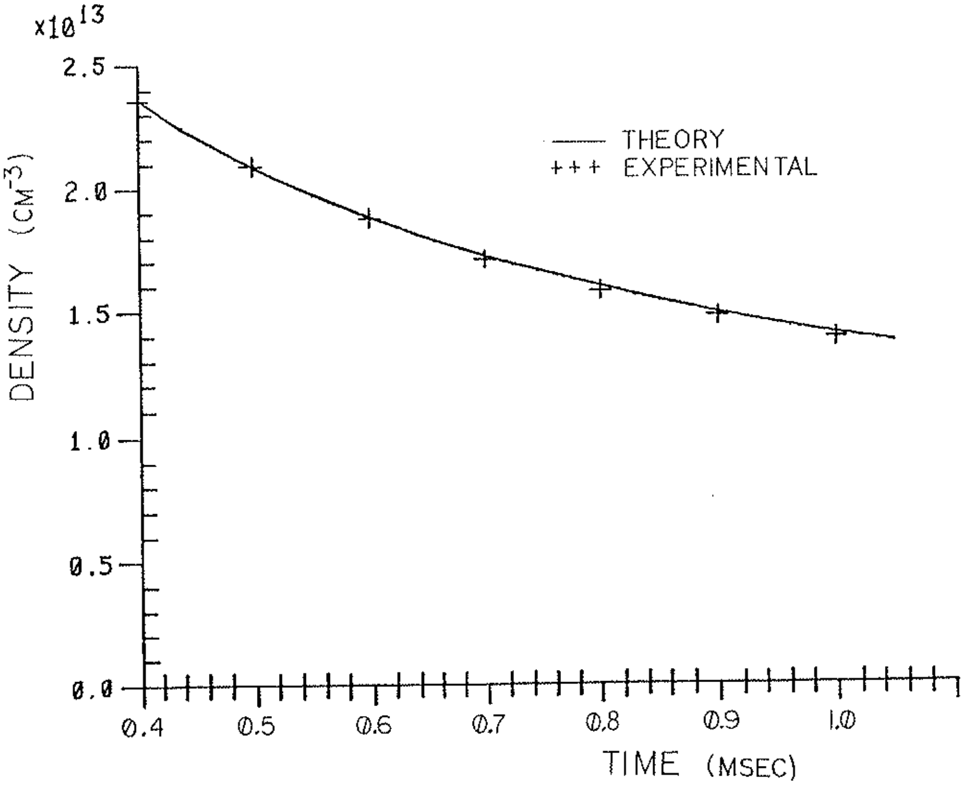

VORTEX IN COMMON FLUX

$B_P = 540$ G

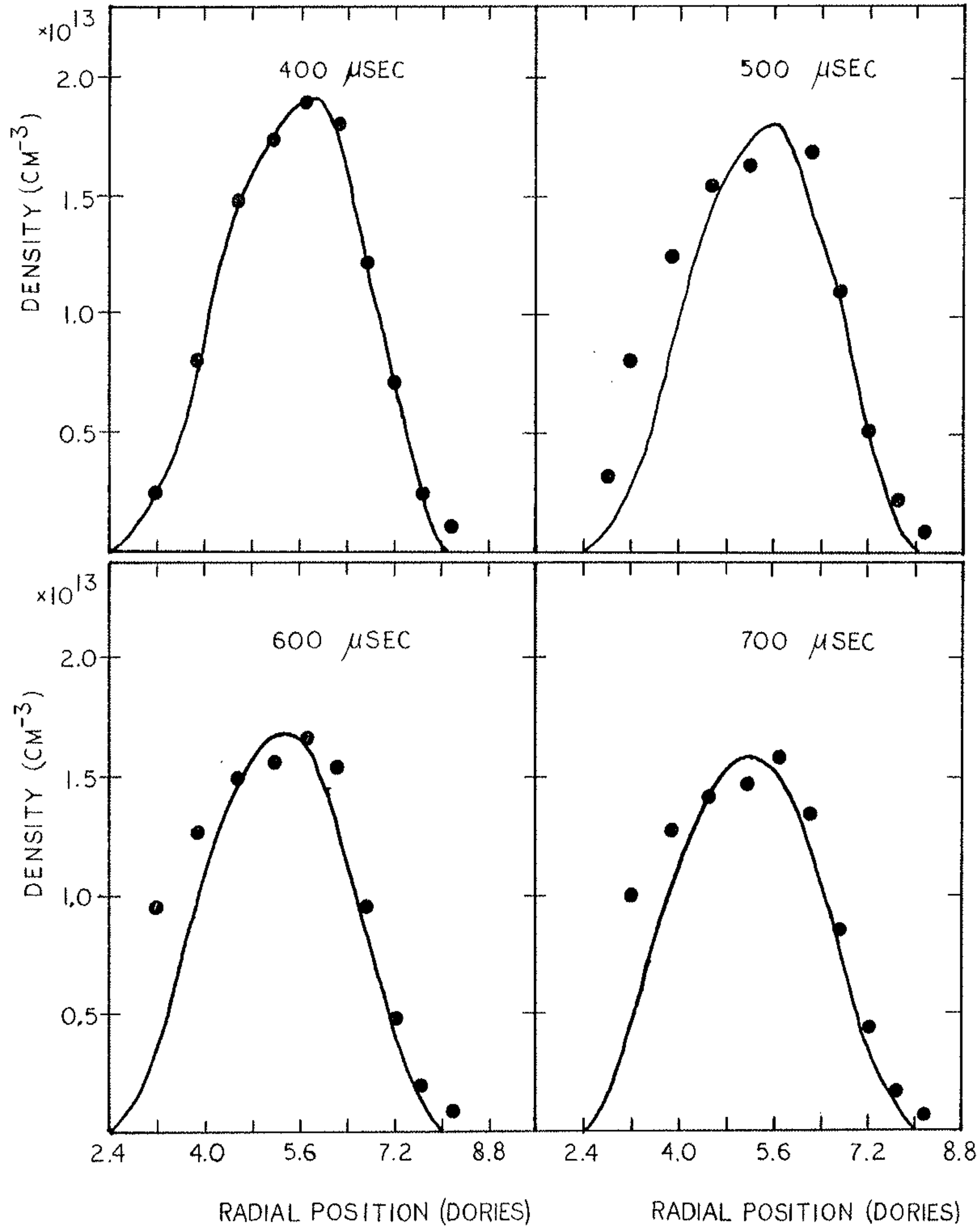
×10^13
2.0
1.5
1.0
0.5
DENSITY (CM^-3)
400 μSEC
500 μSEC
×10^13
2.0
1.5
1.0
0,5
DENSITY (CM^-3)
600 μSEC
700 μSEC
2.4
4.0
5.6
7.2
8.8
2.4
4.0
5.6
7.2
8.8
RADIAL POSITION (DORIES)
RADIAL POSITION (DORIES)

plasmas. For convective cells of the same size as were previously measured, $T^{*}\sim 10^{11}$ eV for the big gun and 10^{9} eV for the intermediate gun. These large enhancement levels above thermal are required in order for vortex diffusion to dominate at these high densities since $D\sim n^{-1/2}$.

There are difficulties, however, with this interpretation. The profile shape for many of the intermediate and low field plasmas cannot be matched, particularly when there is no inward profile motion which is generally true at these fields. In order to match the profile shape at these fields, some vortex diffusion must exist in the private flux. In addition, to match these cases, the decay times for vortex diffusion needs to be much longer than is predicted from classical ion viscous damping. This implies that some mechanism is required to continually regenerate the energy in the vortex spectrum. Although this has been observed before[6], the mechanism has not been identified. Moreover, no mechanism has been identified that would lead to rapid damping of the convective cells in the private flux but not in the common flux.

Finally, the addition of magnetic shear, via toroidal field, should affect vortex diffusion[20]. The addition of toroidal field opens the magnetic field lines and allows charges to flow and short out vortex electric fields. For a mean free path, λ, shorter than the shear length, L_s, the damping time for the vortices is independent of L_s and is simply the time for parallel diffusive flow, $\tau_D=(k_\parallel^2 D_\parallel)^{-1}$, where $D_\parallel\simeq\lambda^2/\tau_e$ and τ_e is the electron collision time. For the parameters in this experiment, the expected damping time is a fraction of a millisecond, so the cells should damp out. Addition of small shear ($B_T/B_p>0.1$) was observed to damp out the convective cells in previous investigations by Navratil, Post, and Ehrhardt[21]. In the current experiment, the addition of toroidal field (B_T=220 G, B_p=860 G on outer bridge separatrix) increases the density decay time slightly from 5000 to 7000 μsec; however, the profile shape is not observed to change to classical. Both the shape and inward motion are similar to the B_T=0 case. Just as a short mean free path can restrict charge flow along field lines, magnetic mirrors along field lines can trap excess charge and enhance the convective cell diffusion[22]. The mean free paths in this experiment are approximately ten times longer than in the experiments by Navratil, and this might account for continued convective transport.

In summary, vortex diffusion in the common flux and classical in the private flux can explain the profile motion and match profile shapes at high field (B>500 G). The observation of classical diffusion in a low field, high density plasma is consistent with a damping time of 85 μsec for vortex diffusion. In addition, where some profile motion is observed, this model also matches the intermediate field cases. The inability to match all the intermediate and low field cases, however, suggests that there may be another transport mechanism that leads to these lower enhancement levels. In addition, since no mechanism has yet been identified that can lead to different levels of vortex diffusion in the private and common flux regions, positive confirmation of vortex diffusion requires the detailed measurement of the convective cell structure.

6.E. Fluctuations

This section presents a survey of the general properties of fluctuations that are observed in plasmas with β up to 40%. This is followed by more detailed description of fluctuation properties for $\tilde{n}$, $\tilde{\phi}$, and $\tilde{B}$, density, electrostatic potential and magnetic field, in a $\beta \sim 3\%$ plasma which is typical of the plasmas studied. In addition, until the enhanced transport reported above is conclusively linked to convective cells by direct measurement of the potential structure, the possibility of other non-diffusive transport mechanisms must be considered, and in particular, the plasma fluctuations could be the cause for the enhanced transport. Thus, the final section presents the results of a calculation of density fluctuation induced transport.

6.E.1. General Properties

For all the plasmas studied in the range of $0.1\% < \beta < 40\%$, the fluctuation levels are strongly peaked in the bad curvature region outside of the separatrix. In the good curvature region inside the separatrix, fluctuation levels of $\tilde{n}/n$ are typically less than 1-2%. Fluctuation levels greater than 1% have been observed on the separatrix in some plasmas. Density fluctuations with $\tilde{n}/n \sim 10$-20% have been measured for various plasmas including those with β up to

40%, however, the fluctuations do not onset when the beta is at its peak value and the fluctuation level increases with time even though beta is decreasing (Fig. 14). These large fluctuations often persist as late as 2-3 msec which is 5-10 e-folding times for the plasma beta. Fluctuations have not been observed which onset early in time when beta is high (above the MHD β limit) and turn off when the beta decreases. A typical fluctuation is observed in the previously mentioned β=11% plasma at a poloidal field of 860 G. Fluctuation levels of less than 2% are measured in the good curvature of the private flux up to the separatrix. Outside of the separatrix, $\tilde{n}/n$ increases to 50%. The onset time for the oscillation on the separatrix is 700 μsec at which time β has decreased to 5%. The onset time is earlier as one moves further into the bad curvature region. The fluctuation continues until ~2 msec even though the β decay time is ~400 μsec. The fluctuations are a mixture of frequencies with the dominant oscillation at f~30 kHz.

In general, the oscillations are not a single frequency although at the lower magnetic fields the fluctuations are more often a purer frequency than at high fields where the fluctuations are almost always less coherent and there is a mixture of many frequencies. In all cases, if there is a dominant frequency it is superimposed on lower level background fluctuations that have a much broader frequency spectrum which is peaked in the low frequency and decreases monotonically as the frequency increases.

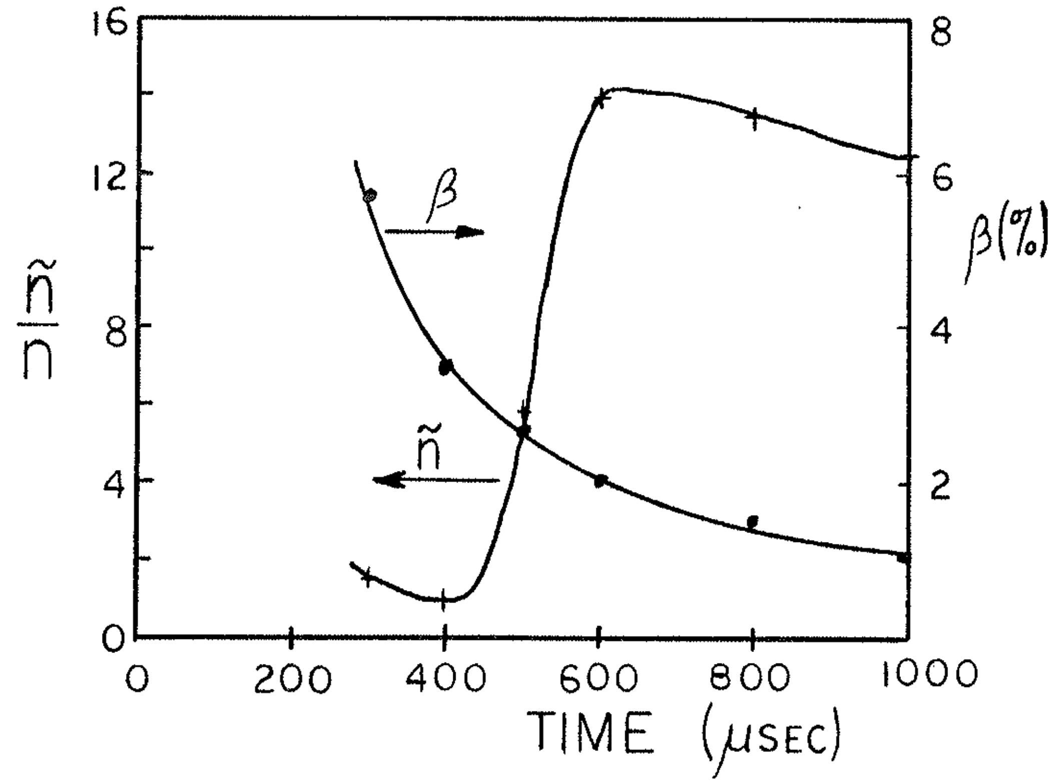

FIG. 14. Density fluctuation in bad curvature region in outer bridge. Note that the fluctuation onsets after β has decreased significantly and $\tilde{n}/n$ remains large even for $\beta \lesssim 1\%$.

Because these are decaying plasmas, the frequency spectrum is not constant in time. In all cases, the frequency of the oscillations observed decreases during the plasma decay. In addition, the frequency of the dominant modes is typically lower in the higher density plasmas. These modes are most likely drift waves because their frequencies are in the correct range (f~30-100 kHz) and the parameter dependence of the frequency is correct. The diamagnetic drift frequency, $\omega_i^* \sim \frac{T}{B} \frac{\nabla n}{n} \sim \frac{T}{B} L_n^{-1}$ decreases as the temperature decreases and the density gradient scale length increases, both of which occur as the plasma is decaying.

There is no indication that any of the fluctuations observed are ideal ballooning modes. Although all fluctuation levels increase strongly in the bad curvature region, this is true of low beta plasmas ($\beta < 1\%$) as well. The properties of the fluctuations are similar over a wide range of beta, and there is no critical beta above which a new oscillation is observed. Drift wave oscillations with properties similar to those observed here have been studied extensively by Rose[23]. No changes occurred in the wave structure as the plasma beta was varied from 8% to as low as 0.004%.

6.E.2. Detailed Fluctuation Properties

The fluctuation properties of a high density ($n{\sim}3{\times}10^{13}$ cm^{-3}), $\beta=3\%$ plasma with $B_p=860$ G were studied in more detail. Density, electrostatic potential, and the poloidal and toroidal magnetic field fluctuations, $\tilde{B}_P$ and $\tilde{B}_T$, were measured, and their power spectrum and correlations are presented. All the fluctuation quantities have properties similar to those mentioned above. Any differences will be specifically noted.

Figure 15 shows a power spectrum for toroidal field fluctuations. The power, P(f), falls off rapidly as the frequency increases with $P(f){\sim}e^{-cf}$ and $c{\sim}4\text{-}5{\times}10^{-5}$ sec, where f is the frequency in sec^{-1}. Figure 16 shows a typical fluctuation observed 7 cm from the ring in the bad curvature region. In the 500 μsec interval shown, the frequency changes from 45 kHz to 20 kHz. Thus, the total sampling period must be chosen to be shorter than 500 μsec for this case. Depending on the rate of change of the frequency, the sampling interval is chosen anywhere from 128 μsec to 512 μsec resulting in frequency resolution of 8 kHz to 2 kHz respectively.

Although the power spectra are similar on the same field line in the upper and lower outer bridge regions, the dominant modes are not exactly correlated because there are slight differences in their frequency. A radial scan between the ring and outer wall shows that the shape of the frequency spectra are similar across the bridge region (Fig. 17). Probes separated toroidally by 6, 12 and 30 cm

FIG. 15. Log of power spectrum of $\tilde{B}_t/B_{vac}$, where $\tilde{B}_t$ is the fluctuating toroidal magnetic field and B_{vac} is the vacuum magnetic field (poloidal field only). The upper frequency cutoff for this particular shot was 300 kHz and the data sampling rate was 1 MHz. The peak value of $\tilde{B}_t/B_{vac}$ is 0.012% at ~30 kHz.

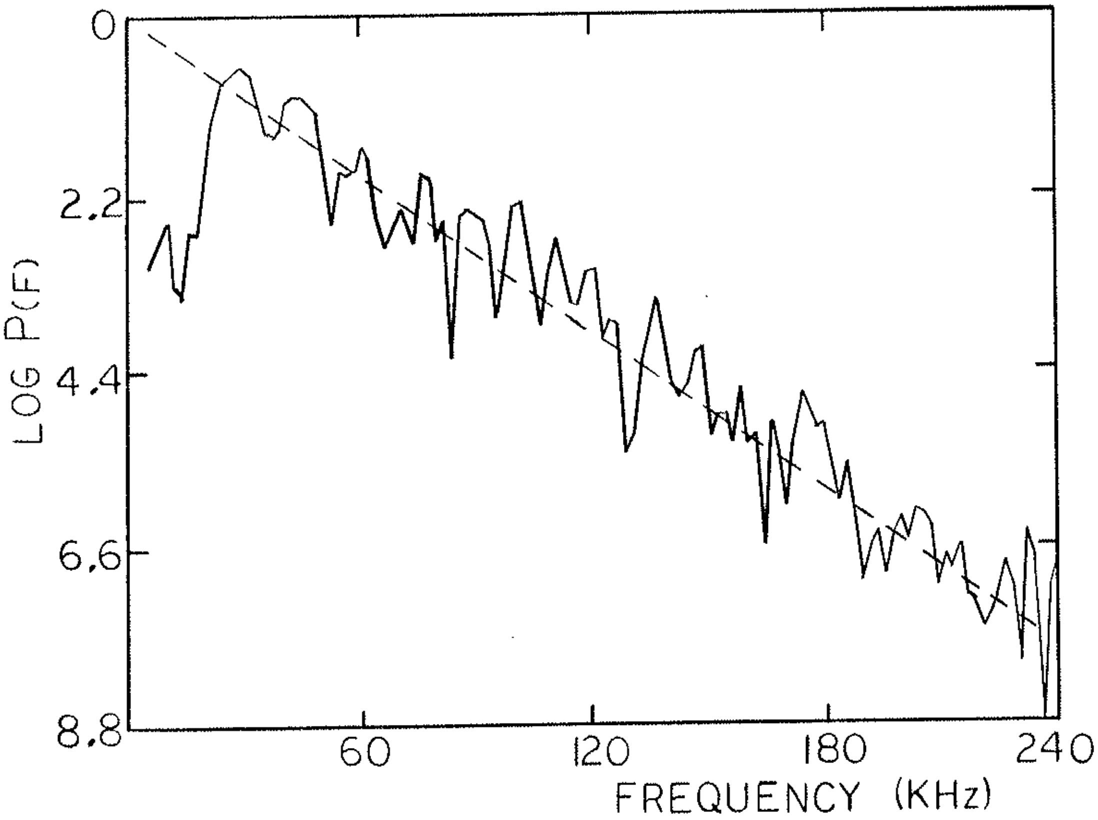
0
2.2
4.4
6.6
8.8
LOG P(F)
60
120
180
240
FREQUENCY (KHz)

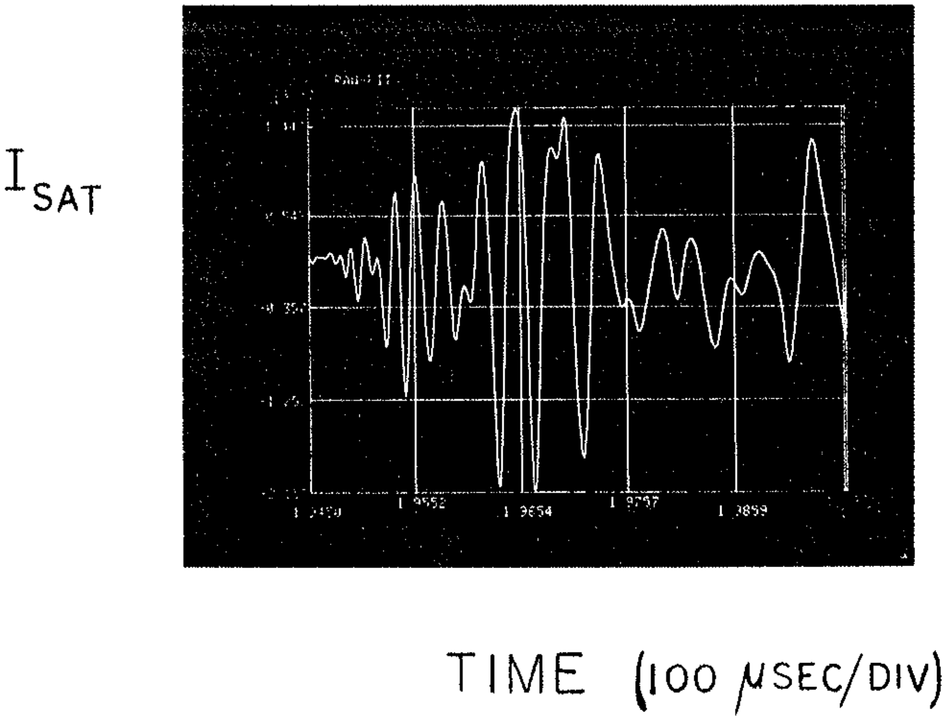

FIG. 16. Typical density fluctuation observed 7 cm from the outer ring in the bad curvature region. ($\beta \sim 3\%$, $B_p = 860$ G).

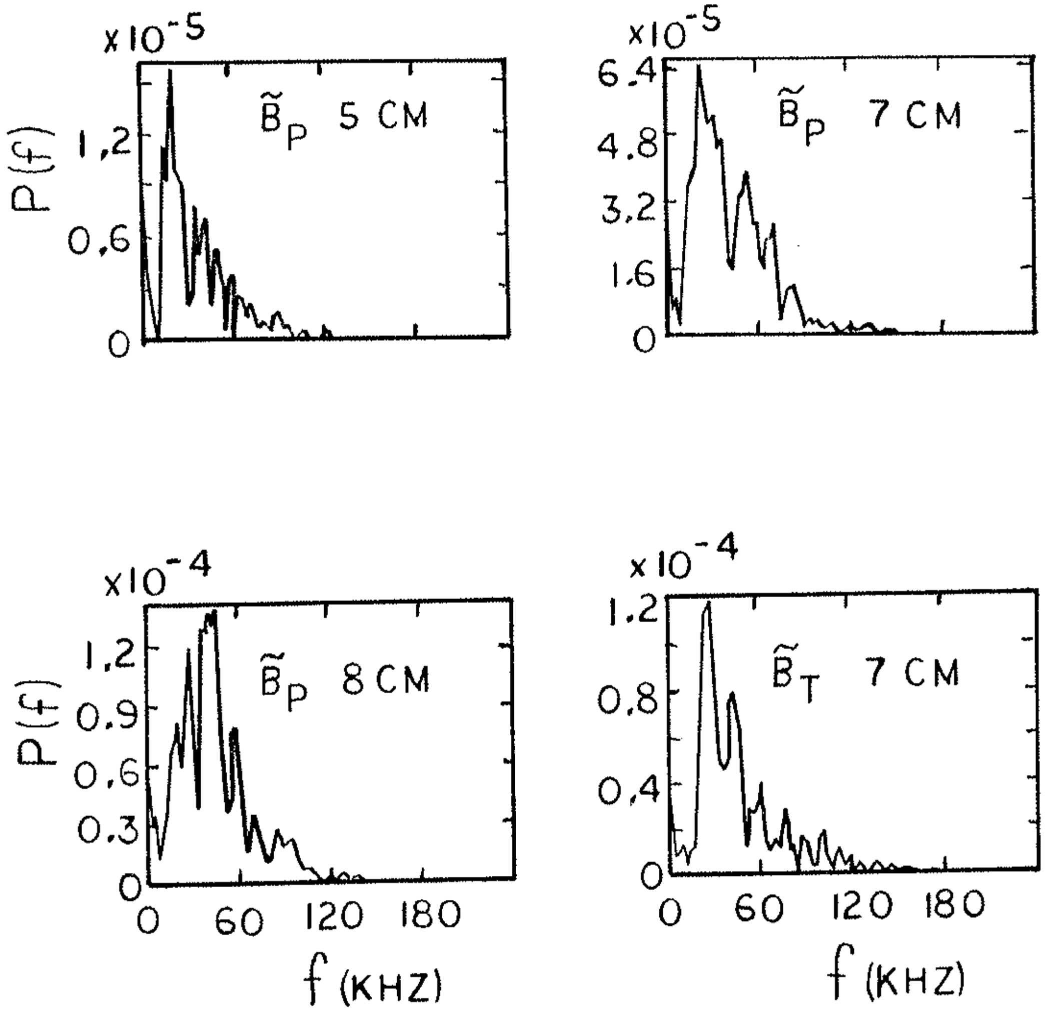

FIG. 17. Power spectra for magnetic field fluctuations at different radial positions. (a)-(c) show the poloidal fluctuation spectra at 5 cm, 7 cm, and 8 cm from the ring. (d) is the toroidal fluctuation power spectrum at 7 cm.

indicate that the dominant modes are coherent over ~10 cm. For the full spectrum, a toroidal probe separation of 6 cm yields an integrated frequency correlation coefficient, η, of 0.8-0.9. For a toroidal separation of 30 cm, η~0.6-0.9 with poor reproducibility. The frequency resolved $\eta(\omega)$ averaged over 20 kHz frequency bins was relatively independent of frequency up to 160 kHz, the highest frequency measured. Variations in $\eta(\omega)$ versus frequency exist but are not reproducible shot to shot.

As mentioned in the previous section, the level of all fluctuations increases strongly in the bad curvature region. This is true for density, potential, and both poloidal and toroidal components of the magnetic field (Fig. 18). Power levels of density fluctuations measured on the same field line in the bridge and nose (ψ=7), i.e. the bad and good curvature regions of the field line, differ by a factor of ~100 with the reduced level in the good curvature. Although this is a sizable decrease, the power level in the nose is still higher than in most of the private flux region.

The cross-correlation coefficient between the density and potential fluctuations for a probe separation of ~0.2 cm is η~0.7-0.9. This value of η is relatively unchanged from 4.0 to 10.0 cm from the ring which includes both good and bad curvature. For comparison, η~0.95-1.0 for the cross-correlation of density fluctuations measured by two Langmuir probes with a similar probe separation. The poorer correlation between $\tilde{n}$ and $\tilde{\phi}$ than between similarly separated $\tilde{n}$ measurements seems to be due to a higher

FIG. 18. Total fluctuation levels for (a) density, (b) electrostatic potential, and (c) poloidal and toroidal magnetic field. The total power is the integral of the power spectrum over the frequency range 20-160 kHz. The magnitudes are in arbitrary units.

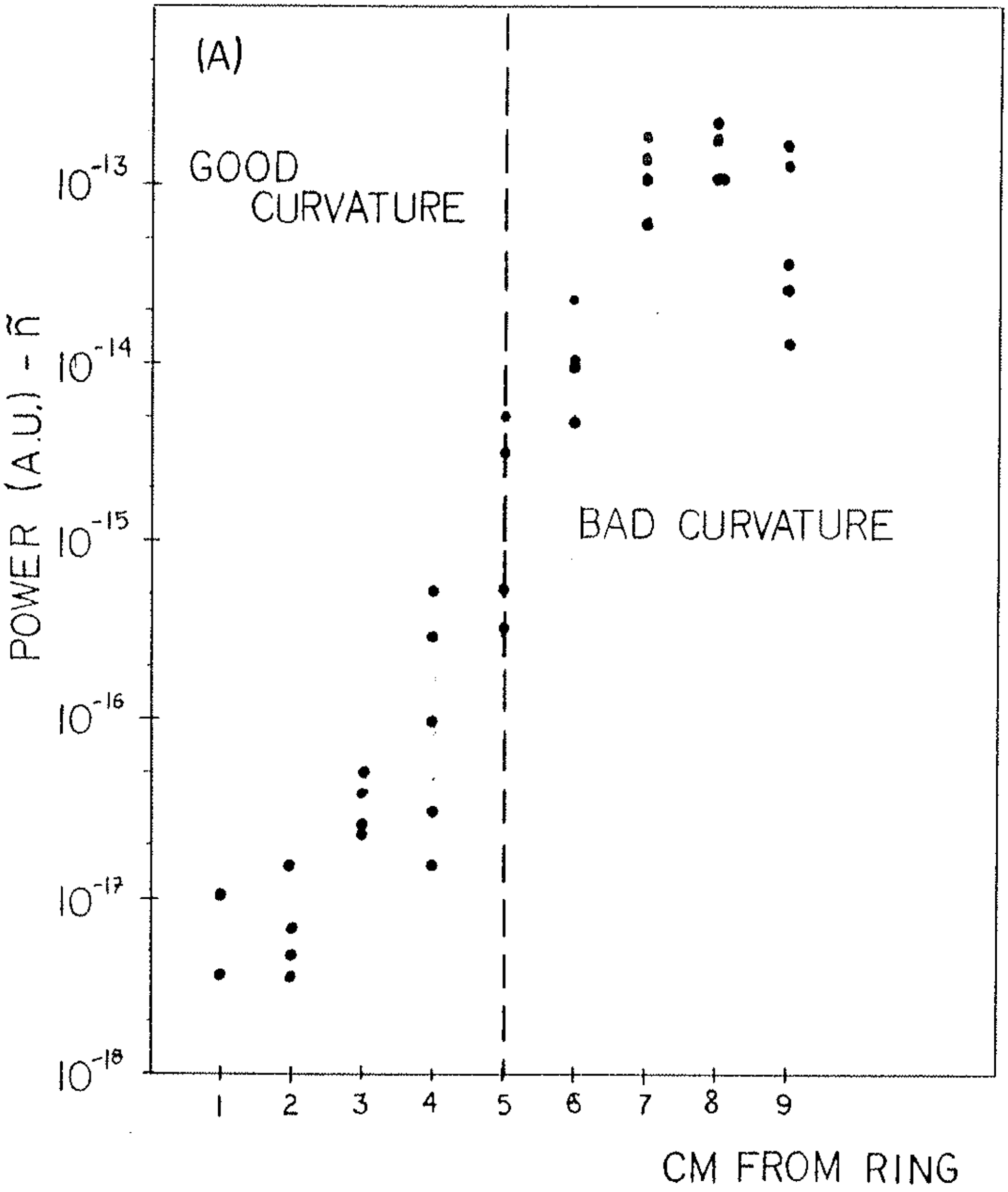
(A)
GOOD CURVATURE
BAD CURVATURE
POWER (A.U.) - ñ
10^{-13}
10^{-14}
10^{-15}
10^{-16}
10^{-17}
10^{-18}
1
2
3
4
5
6
7
8
9
CM FROM RING

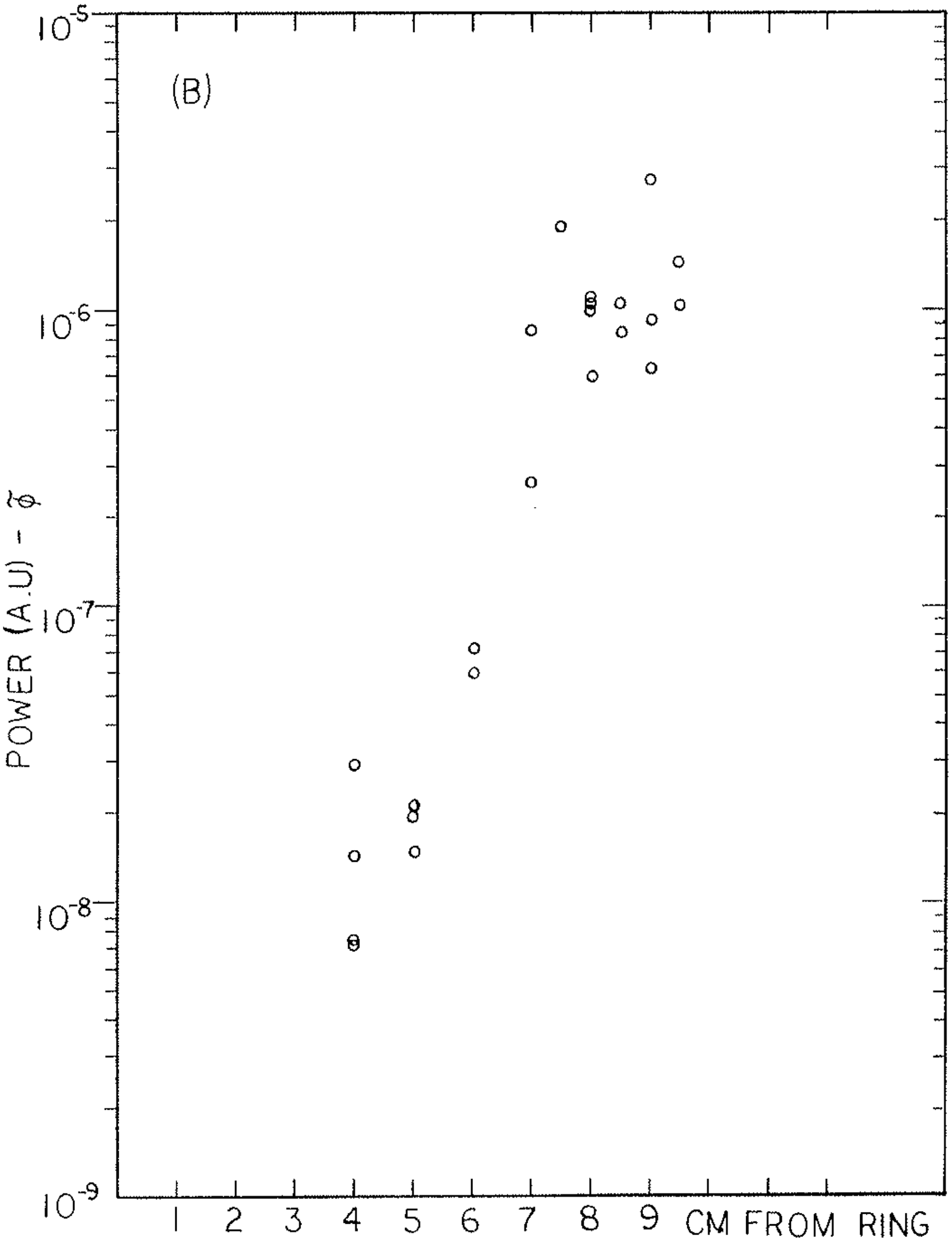
(B)
POWER (A.U) - $\tilde{\phi}$
10^{-5}
10^{-6}
10^{-7}
10^{-8}
10^{-9}
1
2
3
4
5
6
7
8
9
CM FROM RING

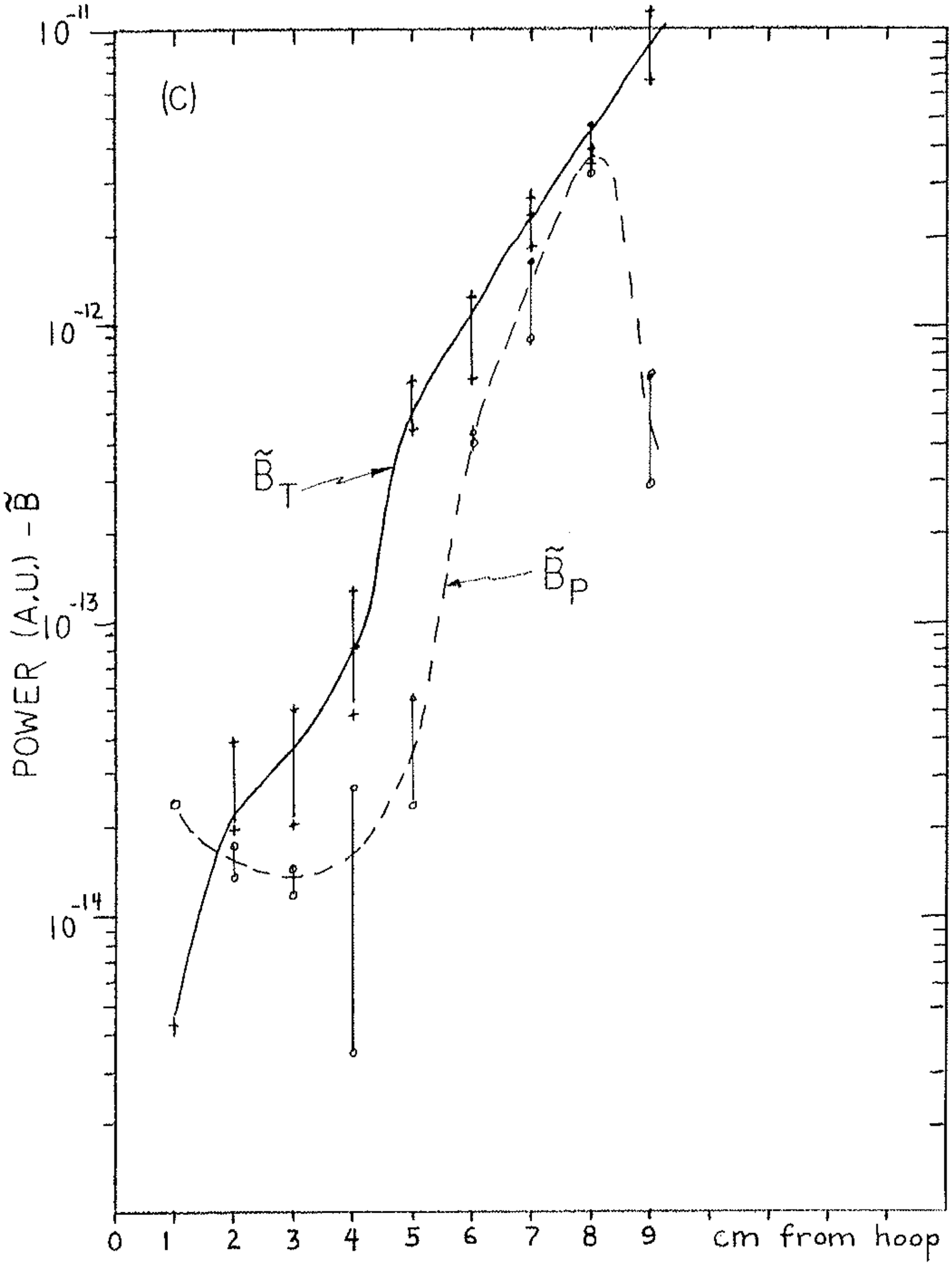
(C)
10^{-11}
10^{-12}
10^{-13}
10^{-14}
POWER (A.U.) - $\tilde{B}$
$\tilde{B}_T$
$\tilde{B}_P$
0
1
2
3
4
5
6
7
8
9
cm from hoop

percentage of low frequency components present in the potential measurements.

It can be seen from Fig. 18c that the toroidal field fluctuations, $\tilde{B}_T$, are typically two to three times larger than the poloidal field fluctuations, $\tilde{B}_P$. This is true not only for this plasma, but for other lower density plasmas $(2\times10^{12}<n<1\times10^{13}\ \mathrm{cm}^{-3})$ at the same magnetic field. The correlation between $\tilde{n}$ and $\tilde{B}_T$ is good with $\eta\sim0.8-0.9$ across the entire bridge region, good and bad curvature (Fig. 19a). The correlation between $\tilde{n}$ and $\tilde{B}_P$ is also good in the bad curvature region ($\eta\sim0.8-0.9$), however, it is slightly worse in the good curvature region (Fig. 19b). The magnitude of the magnetic fluctuations is small with a peak value at 7 cm of $\tilde{B}_T/B_{vac}=0.014\%$ where B_{vac} is the vacuum poloidal field. (The vacuum toroidal field is zero.) Although this value is small compared to $\tilde{n}/n$, it is not negligible when considering the coupling of a drift wave to an Alfvén wave. Although detailed analysis is a topic for future research, preliminary results indicate that $(\tilde{B}/B)/(\tilde{n}/n)$ is roughly proportional to β so that as β decreases, $\tilde{B}/B$ decreases relative to $\tilde{n}/n$. The results indicate that for $\beta_e\sim0.4\%$, $R\equiv(\tilde{B}_T/B)/(\tilde{n}/n)\sim1.1\%$. The value of this ratio (R/β_e) is not a constant as β decays, however, the trend of decreasing R as β decreases is clear from the data.

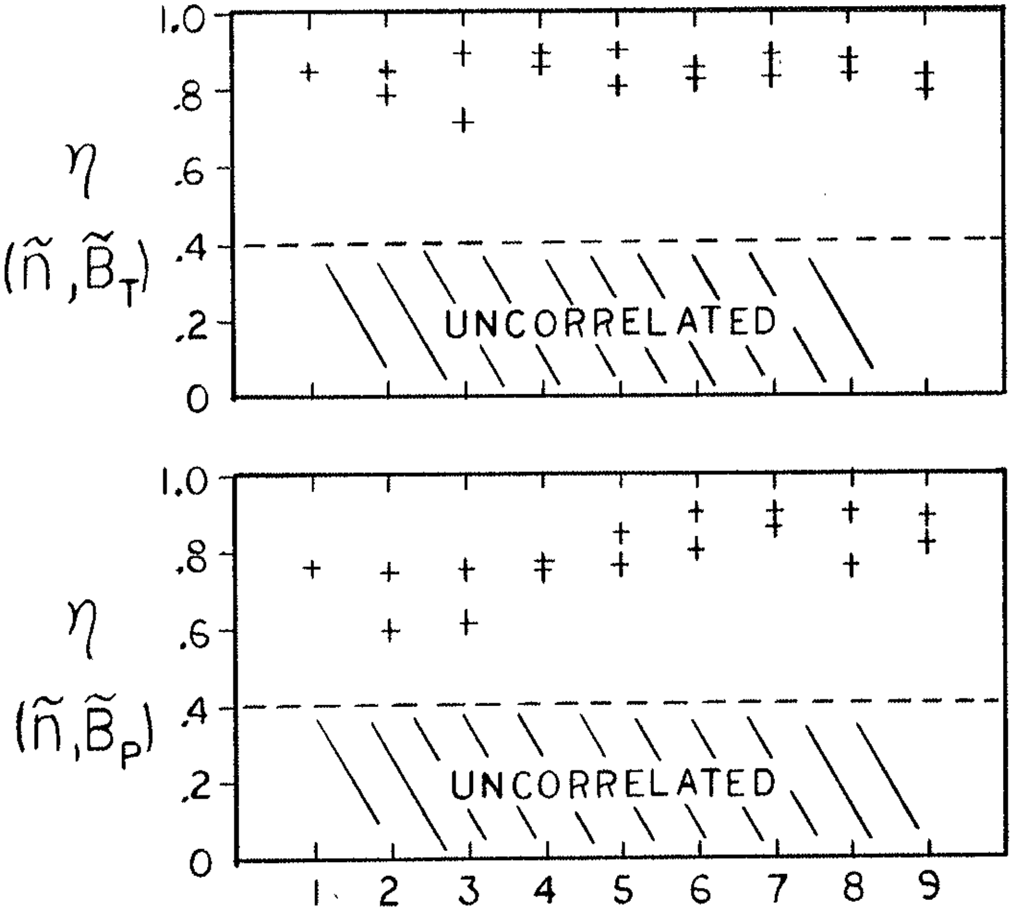

FIG. 19. Radial profile of the total correlation coefficient, η, for density and magnetic field fluctuations. (a) $\tilde{n}$ and $\tilde{B}_t$. (b) $\tilde{n}$ and $\tilde{B}_p$.

6.E.3. Non-Diffusive Transport

As shown above, the fluctuation level of all plasma quantities, $\tilde{n}$, $\tilde{\phi}$, and $\tilde{B}$ increases dramatically as one moves from the internal ring to the outer wall. Thus, fluctuation induced transport could provide the required enhanced transport in the common flux region. Measurements of $\tilde{n}$ and $\tilde{E}$ in the frequency range 10 kHz–160 kHz were obtained in the lower outer bridge region. A time averaged flux was computed over 200 μsec, intervals and this was compared to the experimentally determined flux from measured density profiles (Fig. 20). Since the experimental flux is actually $\oint R\Gamma d\ell$, the fluctuation induced flux measured at one location was multiplied by $\oint R d\ell$ for the field line on which the measurement was taken. This provides an upper limit on the induced transport since power level of the fluctuations in the bad curvature region in the bridge is typically 100 times higher than fluctuations in the good curvature regions on the same field line.

Comparison of the actual flux and the induced flux indicate that the effect of fluctuations is too small to account for the observed transport. At 400 μsec, fluctuation induced transport is less than 1% of the observed transport. Fluctuation levels varied by more than a factor of ten from shot to shot with no noticeable effect on observed transport. Similarly, the direction of the induced flux at a fixed position changed direction from shot to shot and sometimes during a shot with no effect on observed transport.

FIG. 20. Comparison of fluctuation induced transport with the experimental flux determined from the density evolution. The ´+´ indicates that the flux is toward the outer wall and the ´o´ indicates that the flux is toward the ring. Many shots are shown for each position.

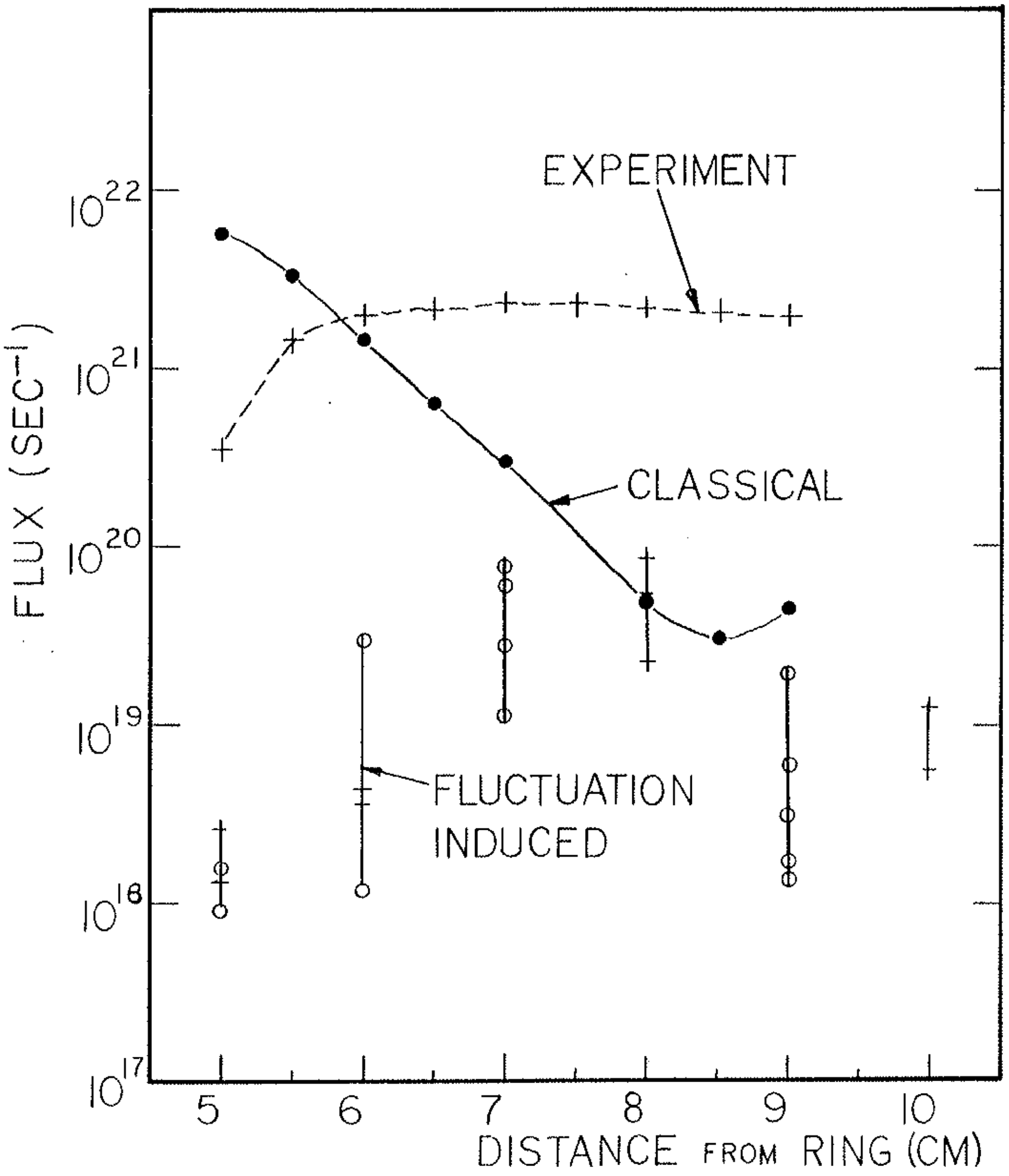
EXPERIMENT
CLASSICAL
FLUCTUATION INDUCED
FLUX (SEC^{-1})
10^{22}
10^{21}
10^{20}
10^{19}
10^{18}
10^{17}
5
6
7
8
9
10
DISTANCE FROM RING (CM)

The magnetic fluctuation levels also increase in the common flux region, and thus they are currently under investigation as a possible mechanism for the enhanced transport. Theoretical work[24] suggests this as a possible mechanism; an experimental study on a tokamak has been performed with no apparent correlation between fluctuations and transport observed.[25]

References for Chapter 6

1. J.R. Greenwood, University of Wisconsin Ph.D. Thesis, (1975).
2. J.R. Drake, J.R. Greenwood, G.A. Navratil, and R.S. Post, Phys. Fluids 20, 148 (1977).
3. G.A. Navratil, R.S. Post, and A.B. Ehrhardt, Phys. Fluids 20, 156 (1977).
4. G.A. Navratil and R.S. Post, Phys. Fluids 20, 1205 (1977).
5. G.A. Navratil, University of Wisconsin Ph.D. Thesis, (1976).
6. H.R. Garner, University of Wisconsin Ph.D. Thesis, (1982).
7. J.R. Drake and J.G. Berryman, Phys. Fluids 20, 851 (1977).
8. J.R. Drake, et.al., Plasma Physics and Controlled Nuclear Fusion Research, Vol. II, (IAEA, Vienna, 1977) 333.
9. J.G. Berryman and C.J.Holland, UCRL-86871 (1981) and J.G. Berryman, UCRL-86873 (1983).
10. R.D. Richtmeyer and K.W. Morton, Difference Methods for Initial Value Problems, (J. Wiley and Sons, Inc., N.Y. 1981) 2nd Ed.
11. D. Greenspan, Discrete Numerical Methods in Physics and Engineering, (Academic Press, N.Y. 1974).
12. G.D. Smith, Numerical Solution of Partial Differential Equations, (Oxford University Press, London, 1965), Ch. 2.
13. W.A. Houlberg and R.W. Conn, Nuclear Science and Engineering 64, 141 (1977).
14. P.K. Smith, "Summary of Ion-Neutral Collision Frequency Data", University of Wisconsin PLP 767 (1978).
15. R.L. Freeman and E.M. Jones, "Atomic Collision Processes in Plasma Physics Experiments", Culham Lab. Report CLM-R137 (1974).
16. J.C. Sprott, "Comparison of Electron Cooling Mechanism in the Toroidal Octupole", University of Wisconsin PLP 235 (1968).
17. H. Okuda and J.M. Dawson, Phys. Fluids 16, 408 (1973).

18. J.B. Taylor and B. McNamara, Phys. Fluids 14, 1492 (1972).

19. A. Butcher Ehrhardt and R.S. Post, Phys. Fluids 24, 1625 (1981).

20. H. Okuda and J.M. Dawson, Phys. Fluids 16, 1456 (1973).

21. G.A. Navratil, R.S. Post, and A. Butcher Ehrhardt, Phys. Fluids 22, 241 (1979).

22. T. Kamimura and J.M. Dawson, Phys. Rev. Lett. 36, 313 (1976).

23. E.A. Rose and S.C. Prager, submitted to Phys. Fluids; E.A. Rose, University of Wisconsin-Madison, Ph.D. Thesis (1982).

24. J.D. Callen, Phys. Rev. Lett. 39, 1540 (1977).

25. S.J. Zweben and R.J. Taylor, UCLA Report PPG-463 (1980).

CHAPTER 7

CONCLUSIONS AND PROPOSAL FOR FUTURE WORK

A wide range of stable high β plasmas has been obtained with β values significantly above the ideal MHD β limit of 4.3% for the Octupole. Plasmas with β up to 44% have been achieved by simultaneous cross-field injection of up to three coaxial Marshall guns. These plasmas are macroscopically stable with beta decay times in excess of 1000 Alfvén times. Although fluctuation levels of equilibrium quantities (density, electrostatic potential, and magnetic field) increase strongly in the bad curvature region, they are not correlated with high values of β; moreover, their properties are similar down to values of β below the MHD β limit.

This paper has considered two particular plasmas, β=8% and 35% in more detail. At β=8% (B_p=860 G), it is found that the equilibrium is well described by single fluid theory. The enhanced stability is explained with a kinetic treatment developed by Phillips that includes the effect of finite Larmor radius which couples the ballooning mode to a stable ion drift wave. Heat flow along field lines was an additional, although small, stabilizing effect. At a lower magnetic field (B_p=200 G), a more collisional, larger gyroradius plasma is obtained with β=35%. For this plasma, the FLR effect is not sufficient to explain the enhanced stability.

In addition, measured equilibrium does not agree with ideal MHD, and in particular, the perturbation to the vacuum magnetic field due to the plasma diamagnetic current is a factor of five too small. This is probably due to ion gyroviscosity, and since the balloning instability is driven by the diamagnetic current, this may account for the stability. Thus, non-ideal effects play a dominant role in the stability as well as the equilibrium of the plasmas, and can significantly alter the predictions of ideal MHD.

Particle transport is enhanced above classical for all but the highest beta, low field plasma. The level of enhancement increases with magnetic field strength up to thirteen times the classical rate in a β=11%, high field (B_p=860 G), high density plasma ($n=5.9\times10^{13}$ cm^{-3}). The enhanced transport is predominantly in the common flux region, particularly at high magnetic field, and this results in an inward motion of the density profile. Profile shapes and the density decay rates are compared with a computer model of the diffusion in the Octupole. No single diffusion coefficient can match all the profile shapes and decay rates; however, it is found that a good match to many of the profiles can be obtained if the enhanced transport in the common flux is due to vortex diffusion. No mechanism has been identified that would account for the existence of vortex diffusion in the common flux region only. Other possible mechanisms to enhance the transport, such as neutral-ion collisions and density fluctuation induced transport are shown to be too small.

Suggestions

There are many possible directions that future research could follow. In the search for the ballooning instability, the most promising prospect is plasma heating with ICRH. By producing a sustained, high β plasma, many of the problems associated with a decaying plasma can be eliminated, in particular, those asociated with the measurement of fluctuation properties. In addition, increasing plasma β by heating would permit the observation of the growth of the mode.

Aside from the goal of searching for the β limit, investigation of high β plasma properties should be pursued. Convectives cells have been measured in low density and low β plasmas where they are purely electrostatic, however, they have never been identified in a high beta plasma. In addition, direct measurement of the convective cells would conclusively verify the interpretation of the particle transport.

Study of the magnetic fluctuations should also be pursued. A full examination of the coupling of drift waves to Alfvén waves requires the measurement of the radial magnetic field perturbations as well as the components that were measured here. If as in this experiment, modes with long coherence lengths cannot be found, the measurement of the magnetic field and corresponding density oscillation should be done with the same probe in order to get better correlation. Finally, a measurement of fluctuation induced transport due to the small scale magnetic fluctuations should be pursued. The high values of β routinely available and the ability to use probes in the plasma provide a unique opportunity for investigation.

APPENDIX

In Eq. (10) for the radial structure of the ballooning mode, the constants a_o–a_7 are as follows:

$$a_o = \oint \frac{r^2}{J}\left(\frac{\partial U_o}{\partial \chi}\right)^2 d\chi \quad ,$$

$$a_1 = \oint J r^2 U_o^2 d\chi \quad ,$$

$$a_2 = \oint \frac{\partial U_o}{\partial \chi} \frac{r^2}{J} \frac{\partial}{\partial \chi} \left(\frac{\partial U_o}{\partial \phi} + \frac{\mu_o p'}{B^2} U_o\right) dx \quad ,$$

$$a_3 = \oint U_o J r^2 \left(\frac{\partial U_o}{\partial \phi} + \frac{\mu_o p'}{B^2} U_o\right) d\chi \quad ,$$

$$a_4 = \oint \frac{r^2}{J} \left[\frac{\partial}{\partial \chi}\left(\frac{\partial U_o}{\partial \phi} + \frac{\mu_o p'}{B^2} U_o\right)\right]^2 d\chi \quad ,$$

$$a_5 = \oint Jr^2\left(\frac{\partial U_o}{\partial \phi} + \frac{\mu_o p'}{B^2}\,U_o\right)^2 d\chi \quad ,$$

$$a_6 = \oint JDU_o^2 dx \quad ,$$

$$a_7 = \oint J\,\frac{U_o^2}{r^2 B^2}\,d\chi \quad .$$

The constants C_o-C_5 appearing in Eqs. (12)-(14) are:

$$C_o = -\int_{\phi_a}^{\phi_b} \mu_o m_i p a_7 R_o^2 d\phi \quad ,$$

$$C_1 = -\int_{\phi_a}^{\phi_b} \mu_o m_i p\left[a_1\left(\frac{\partial R_o}{\partial \phi}\right)^2 + 2a_3 R_o\,\frac{\partial R_o}{\partial \phi} + a_5 R_o^2\right]d\phi \quad ,$$

$$C_2 = \int_{\phi_a}^{\phi_b} \mu_o(p'-p_o')a_6 R_o^2 d\phi + \int_{\phi_a}^{\phi_b} \omega_o^2 a_7 R_o^2 d\phi \quad ,$$

$$C_3 = \int_{\phi_a}^{\phi_b} \left[a_o\left(\frac{\partial R_o}{\partial \phi}\right)^2 + 2a_2 R_o\,\frac{\partial R_o}{\partial \phi} + a_4 R_o^2\right]d\phi \quad ,$$

$$C_4 = -\int_{\phi_a}^{\phi_b} \mu_o m_i p' a_7 R_o^2 d\phi \quad ,$$

$$C_5 = -\int_{\phi_a}^{\phi_b} \mu_o m_i p' \left[a_1 \left(\frac{\partial R_o}{\partial \phi}\right)^2 + 2a_3 R_o \frac{\partial R_o}{\partial \phi} + a_5 R_o^2 \right] d\phi \quad .$$

where the $\{a_i\}$ are defined above and the limits ϕ_a and ϕ_b are the boundaries of $R_o(\phi)$.